Università degli Studi di Cagliari

PhD Degree in Physics

Cycle XXXIV

Structural and optical characterisation of all-inorganic perovskites

Scientific Disciplinary Sector(s)

FIS01

Ph.D. Student: ***Jessica Satta***

Supervisor ***Prof. Pier Carlo Ricci***

Final exam. Academic Year 2020 – 2021
Thesis defence: March 2022 Session

Abstract

History gives us evidence that the occurrence of problems drives human being evolution, bringing to the development of new efficient technologies. Now, in the twenty-first century, a lot of global problems are threatening our future: global warming, toxic wastes, water, and air pollution, decreasing energy supplies. In this perspective, great importance has acquired the development of materials, methods, and devices with a low impact on the Earth reservoirs. The use of the never-ending solar radiation, photocatalysis, and Earth-abundant raw materials are some examples. Effectively converting and harvesting power from the sun is a promising strategy to meet the increasing energy demands of human society. As well as solar-driven pollutants conversion into valuable chemical products has been regarded as a promising route to alleviate the increasing environmental problem of greenhouse gas emission. On these bases, in the last decades, an increasing interest has been addressed to lead halide perovskites. Since the 1990s, halide perovskites have received increasing attention in an optoelectronic context for their intrinsic properties, finding potential applications in many different sectors and devices from efficient light harvesters to photovoltaics, photodetectors, solar fuels, lighting and displays. On the other hand, their application in commercial devices is strongly hampered by their instability.

The aim of the Ph.D. project was primarily structurally and optically characterize caesium lead halide perovskites, shedding light on the role of external factors which undermine their stability.

The first part of the work was focused on completing the characterization of $CsPbI_3$. Because of the rapid phase transition, it appeared urgent a fast experimental tool to rapidly identify different polymorphs.

Among inorganic lead halide perovskites, $CsPbI_3$ is the most attractive for the scientific community due to its narrow bang gap, the absorption in a large portion of the solar spectrum and the emission of a deep red light. However, it is the most vulnerable member of lead halide perovskites under ambient conditions, because of the presence of iodine. Most of the first studies were focused on finding the most efficient and stable device, with more attention to the stabilization and less to understanding the reasons of the instability, leading sometimes to misleading assignation of the different phase structures.

We proposed Raman spectroscopy to fulfil this task, providing a definitive assignation of the Raman peaks with a careful analysis of the vibrational modes for the cubic and the orthorhombic phase of ABX_3 perovskites, carried out by experimental measurements on $CsPbI_3$ samples corroborated by DFT calculations. $CsPbI_3$ perovskite was synthesized by a solid-state reaction, and its structural and

optical properties were deeply investigated using a multi-technique approach. Furthermore, the optically induced degradation process and the phase evolution as a function of the synthesis time length were studied, providing new insights on the formation mechanism of secondary phases.

Looking at the applications of caesium lead halide perovskites, it is essential to solve the problem of their instability. In this perspective, many studies suggest that nanocrystals are more stable than the bulk counterpart, thanks to the contribution of surface energy. But in practice, in the architecture of the devices, it becomes particularly important also the interaction among the different components in operative conditions. With a view at the potential applications in photovoltaics and photocatalysis, we realized a heterostructure of $CsPbBr_3$ NCs and nanoporous gold. With the aim of studying the optical properties variations due to the interaction between the structures, the heterostructure was realized directly synthesising $CsPbBr_3$ nanocrystals on gold surface, revealing a high-efficiency charge transfer.

Even if more structurally stable, nanocrystals still suffer from the instability in ambient conditions. In this perspective, different kind of encapsulation have been proposed, to deal with environmental stresses. For this purpose, a preliminary work has been done to study the stability of inorganic perovskites in a mesoporous silica matrix. The mesoporous structure provides the template to synthesize nanosized perovskites, and collapsing at high temperature, encapsulates the perovskites providing good stability and preserving their excellent optical properties. $CsPbCl_3$, $CsPbBr_3$ and $CsPbI_3$ NCs have been obtained with different optical and emitting properties that permitted us to obtain a first prototype of RGB matrix for lighting applications.

Table of contents

Table of figures

Table of tables

Thesis structure

The thesis is structured in 9 chapters. Chapter 1 presents an introduction on lead halide perovskites, illustrating their structure and properties, placing more attention on their criticism, the stability.

In chapter 2, after a theoretical discussion on the vibrational properties of cubic and orthorhombic $CsPbI_3$, the assignation of δ-$CsPbI_3$ experimental Raman modes is reported, corroborated by DFT calculations. Moreover, Raman spectroscopy is used to describe the laser-induced phase degradation.

Chapter 3 illustrates the study on the stability of $CsPbI_3$ as function of the synthesis time length. $CsPbI_3$ is synthesized by a solid state-reaction and the formation of secondary phases during the process is described by a multi-technique approach.

Chapter 4 discusses the different efforts made in the last years to stabilize lead halide perovskites, introducing the work reported in the following chapters.

In chapter 5, a heterostructure of $CsPbBr_3$ NCs and nanoporous gold is presented, focalizing on its optical properties.

Chapter 6 illustrates the work on NCs encapsulated in silica matrix. The preliminary results are reported together with the first prototype of an RGB matrix.

Finally, conclusions, references and appendix are reported, respectively, in chapter 7, 8 and 9.

1 Caesium lead halide perovskites: State of the art

Perovskites belong to a class of crystalline compounds described by the generic chemical formula AMX_3, with A being a large cation, M a smaller metal cation and X an anion of the halide series. Essentially, they can be divided into two types, hybrid organic-inorganic perovskites and inorganic perovskites, depending on the nature of the A-site ion. In hybrid halide perovskites, the organic cations are small and are typically restricted to methylammonium, ethyl ammonium and formamidinium, while in all-inorganic halide perovskites, the A cation is caesium or rubidium. The metal cations are typically divalent metal ions such as Pb^{2+}, Ge^{2+} and Sn^{2+}, while the halide anions are I^-, Cl^- and Br^-.[1]

The first synthetic lead halide perovskite was prepared in 1892, although its structure and properties were studied only in the second half of the 1900s.[2,3] The interest for these materials was born in the area of scintillators, to convert high energy X-ray photons into low energy visible photons. X-ray absorption increases with the atomic number and lead halide perovskites, thanks to the presence of heavy atoms, exhibit a large X-ray stopping power. X-ray photons are efficiently converted in charge carriers, which thermalizing in low-energy exciton, produce visible photons via bandgap emission. Unlike conventional scintillators, such as CsI:Tl, $PbWO_4$, $YAlO_3$:Ce and $Bi_4Ge_3O_{12}$, with fixed transition energies, the narrow emission of lead halide perovskites is tuneable from the near UV to near-IR moving from Cl-rich to I-rich composition, and varying size or dimensions.[4] Moreover, lead halide perovskites are soluble processable and show a very bright photoluminescence. These properties, together with the high absorption coefficient, high charge carrier mobility and long electron-hole diffusion length, offer new opportunities in many applications, like photovoltaics, LEDs, lasers, photodetectors, photocatalysis. In the last years, power conversion efficiency (PCE) of perovskite solar cells increased to over 20%, making them competitive photovoltaic technology with Si-based solar cells.[5] Combining a direct bandgap with the presence of p-p transition and Pb lone-pair s orbitals, lead halide perovskites show an highly efficient optical absorption.[6] Furthermore, they exhibit a high defects tolerance compared to traditional semiconductors (such as Si and GaAs), where the presence of impurities can be detrimental forming mid gap trap states. In lead halide perovskites, despite the low formation energy, vacancies and other defects form states residing within the VB and CB, or at worst are shallow defects.[7] Additionally, lead halide perovskites present high PL quantum yields (QYs) and highly saturated colours because of their narrow emission bandwidths. They offer blue, green and red primary colours with an impressive gamut, achieving up to ~140% of the North American National Television Standard Committee (NTSC) specification. In the context of LCDs, they can be used as colour downconverters in backlighting, converting the blue light

generated by standard InGaN LEDs (~460 to 470 nm) into lower-energy emission in green (530 nm) and in red (630 to 640 nm).[7] Despite the countless properties and the numerous studies on lead halide perovskites, they are far to be commercialized because of their instability over long-term operation.

1.1 Phase stability

Perovskites are based on a three-dimensional structure of corner-sharing [MX_6] octahedra, with the A-site cation located within the cuboctahedron cavities. So, the size of the cation A is an important aspect for the formation of a closed packed perovskite structure, since this cation must fit into the space composed of the eight adjacent octahedra.

Generally, the structural stability of perovskites AMX_3 is determined by the Goldschmidt tolerance factor:

$$t = \frac{r_A + r_X}{\sqrt{2(r_M + r_X)}}$$

with r_A, r_M, r_X being the different ionic radii. It assesses whether the A cation can fit the space within the octahedra cages. The ideal cubic structure is not very common and usually arises in the range $0.8 < t < 1$. If $t > 1$, the A cation is too large to form the cubic perovskite structure, and if $t < 0.8$, the A cation is too small, inducing lattice distortions and leading to non – perovskites structures. Goldschmidt tolerance factor is not sufficient to predict the stability of the perovskites structure. An additional indicator is the octahedral factor $\mu = {r_M}/{r_X}$, which determines if the M cation fits the octahedron X_6.[1,8] To stabilize the octahedron [MX_6], it requires $0.414 \leq \mu < 0.592$. If μ is smaller than 0.414, M cation is not in contact with the X anions and leads to a smaller coordination number. If it is bigger than 0.592, a coordination number of 7 is more favourable.[9]

Whereas the Goldschmidt and octahedral factors allow estimating the stability of perovskites from a geometrical empirical point of view, the formation energy provides a theoretical description based on thermodynamics, since under equilibrium conditions, the compound or the polymorph with the lowest formation energy is the most stable one. All the members of the group of trihalides undergo phase transitions when varying the temperature, with the high – temperature cubic phase (α) with space group $Pm\bar{3}m$ which transitions either to a tetragonal (β) $P4/mbm$ (in the case of inorganic perovskites) or $I4/mcm$ (in the hybrid counterpart). Furthermore, both hybrid and inorganic perovskites show an orthorhombic (γ) Pnma ground – state. All these structural phase transitions are the result of the flexibility of the structure of corner-connected $[MX_6]^{4-}$ octahedra, which induces octahedral tilting and breaks the symmetry of the cubic structure, for the purpose of lowering the lattice entropy at low temperatures. Finally, several compounds, particularly $FAPbI_3$ and $CsPbI_3$, also

exhibit a photoinactive non-perovskites yellow polymorph, known as δ phase, which consists of one-dimensional chains of face-sharing octahedra.[10–13] While the δ phase is the most stable at room temperature, only the perovskite structures have optical properties suitable for optoelectronic applications, having optical bandgaps ranging between ~1.73 eV and ~2.3 eV. The application in commercial devices is strongly hampered by low phase stability. The resistance to various environmental stresses such as humidity, illumination and high temperatures under prolonged operative conditions must be fully satisfied. In this respect, caesium-based all-inorganic lead halide perovskites show superior thermal stability compared to the hybrid counterpart. Because of the presence of organic components, these latter are highly instable at temperatures above 80 °C, resulting unsuitable in real operating conditions.[14–16] The same organic components are highly hygroscopic, and their coupling with water molecules to form hydrated form of perovskites leads to moisture-induced decomposition.[17–19] As well as directly reacting, absorbed water can acts also as catalyst, promoting the phase transition of perovskites to their non-perovskite structure.[20] Because of the large solvation enthalpy of halide ions and the corresponding low vacancy formation energy, also Cs-based inorganic perovskites suffer from poor moisture stability. The absorption of water on the surface can generate vacancies in the crystal lattice, catalysing the phase transition.[21] Whereas moisture can be avoided by encapsulation, perovskites employed in solar cells have to be stable under illumination. Both in inorganic and hybrid perovskites, illumination with visible light accelerates the degradation, inducing different phenomena such as phase segregation and ion migration.[22–24] As consequence, a major issue in the development of Lead halide perovskites is the assessment of the crystal structure of the samples, due to their typically limited time-stability, and the understanding of the role of external factors that can induce a crystal phase transformation.

1.2 Identification of polymorphs

The most widely studied inorganic perovskites are $CsPbI_3$ and $CsPbBr_3$, with a photoluminescence quantum yield (PLQY) over 90% and 95%, respectively.[25–27] $CsPbI_3$ shows the narrowest band gap, 1.73 eV, being able to absorb large part of the solar spectrum. However, at room temperature the cubic α-$CsPbI_3$, is not thermodynamically stable and a temperature above 320 °C is required to set and keep this phase under controlled conditions, being the α-phase very quickly transformed into the δ-phase under ambient conditions. Thermal treatments, high flux illumination, humidity, further affect the stability of the α–phase and represent the bottleneck that prevents its exploitation in technological devices.[28] The Goldschmidt tolerance factor is of about 0.81 for $CsPbI_3$, thus generating an intrinsic instability in the structure.[28] However, different strategies have been tested

and applied to extend the time stability of the α-$CsPbI_3$ phase at room temperature. One of them regards the doping of the structure with Rb in the A site,[29] Sn, Ti, Mn in the B site [30,31] and Cl and/or Br in the anion X site.[32,33] Other strategies consist in engineering the surface to reduce the effects of water and humidity in ambient conditions, so that additives were added to the synthesis procedure to reduce the surface energy or to coat the surface and passivate it.[34–37] Finally, great efforts have been devoted to decrease the crystal dimensions to obtain active films, since a higher phase stability was observed when decreasing the grain dimensions down to nanoscale. In particular, samples of α-$CsPbI_3$ were kept stable for months when the dimensions were reduced to Quantum Dots.[38,39] However, the synthesis procedure requires tricky steps, due to the care of the samples and the high degree of control of the atmospheric conditions. Indeed, the synthesis should be carried out in absence of humidity (dry air), or under Nitrogen or Argon pressure, and the sample must be enveloped in a thoroughly resistant, transparent, hydrophobic material to prevent phase deterioration. Therefore, the control and the structural characterization take on great importance for a deeper development of perovskites-based devices and new synthesis methods, calling for a fast and reliable in-situ crystal characterization.

On these bases, during the Ph.D. course, two different works were developed. In the first, Raman spectroscopy has been proposed as a fast and reliable technique to identify lead halide perovskite polymorphs. Despite the large use of the technique in different sectors of solid-state sciences, there is a lack in the application of Raman spectroscopy to Lead halide perovskites. As it is detailed in the next report, the reason is strictly connected to the above-mentioned cubic structure, the presence of different polymorphs, and the low structural stability under illumination.

Successively, the phase transition mechanism and the phase stability of $CsPbI_3$ samples, obtained through a one-step solid-state reaction, have been studied. The phase evolution depending on synthesis time length has been observed and the key role of the local stoichiometry at the nanometre scale in defining phase formation was deeply analysed.

2 Raman spectra and vibrational analysis of $CsPbI_3$: A fast and reliable technique to identify lead halide perovskite polymorphs

Jessica Satta, Claudio Melis, Carlo Maria Carbonaro, Andrea Pinna, Manuel Salado, Daniel Salazar, Pier Carlo Ricci

Journal of Materiomics 7 (2021) 127 – 135

DOI: 10.1016/j.jmat.2020.08.004

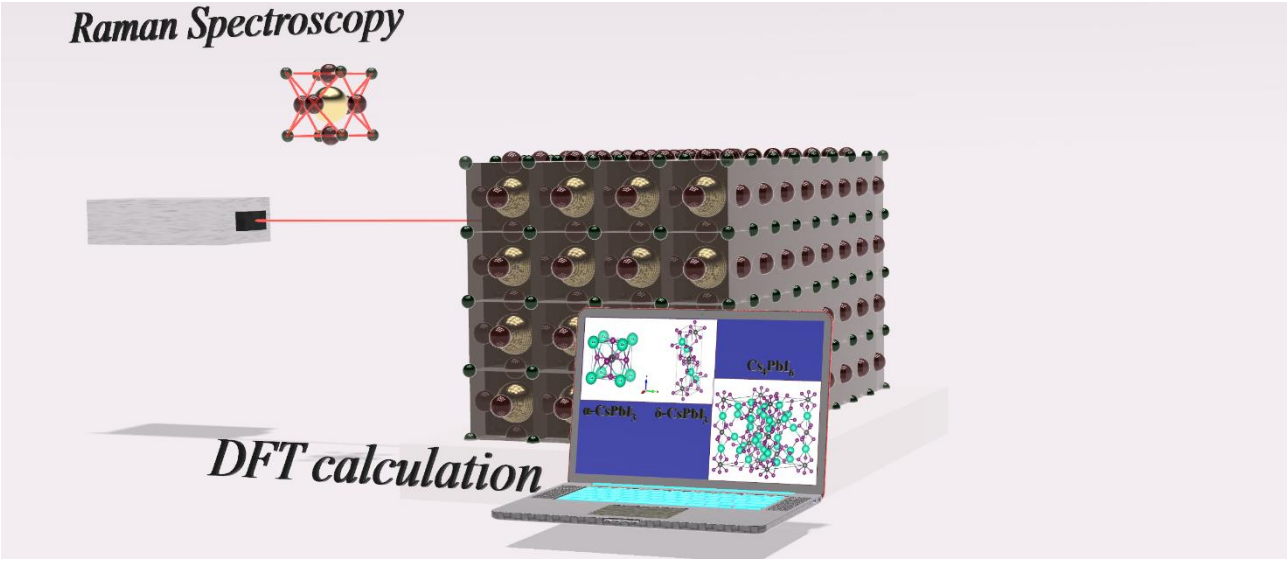

As already indicated, it is of utmost importance to have at disposal a fast and reliable experimental tool able to give an immediate indication of the polymorph of the sample with the possibility to integrate in-situ measurements for constant monitoring.

The analysis of XRD pattern is certainly the most common technique applied to assess the crystal phase of the synthesized samples, but it cannot be performed in-situ for a direct control of the synthesis procedure. In addition, since in general it requires a quite long procedure and the careful preparation of the samples, it can give low information of the effective time stability, in particular during the synthesis steps, when an effective control is mostly required. Moreover, amorphous or not extended enough crystalline phases remain unobserved using the XRD technique.

Other strategies for in-situ monitoring involve optical characterizations like luminescence and/or optical absorption measurements. Indeed, the α- phase has a lower band gap as compared to the δ phase (1.7 eV vs 2.8 eV in $CsPbI_3$, respectively) and displays a different luminescence emission peak (700 nm vs 550 nm in $CsPbI_3$) and emission efficiency.[40,41] However, these measurements give indirect information on the structure and cannot be useful, for example, in case of mixed phases.

Raman spectroscopy could be a reliable tool that conjugates the fast-experimental set-up of the optical characterization with precise structural information, useful for in-situ monitoring of phase transformations.[42–44] Nevertheless, up to now it is not a very common technique for the characterization of Lead Halide perovskites because of the difficulty in the assignment of the Raman bands. Indeed, there are a few papers that exploit Raman spectra to assess the structure achieved during the synthesis.[45–49] However, there is still disagreement on the assignment of the Raman peaks to a specific phase and no dedicated works were performed for a fully understanding of the vibrational analysis. Xiang et al. claimed that a peak at 238 cm^{-1} can be used as fingerprint for the presence of the α-phase in $CsPbI_3$,[45] and Strauss et al. identified an additional band at about 90 cm^{-1}.[47] However, both the peaks were assigned to pure PbI_2 in a different work.[46] Similarly, Raman measurements were exploited to follow the temperature-induced phase transition, identifying several bands in the low frequency part of the Raman spectrum as related to the α-phase in $CsPbI_3$,[48] but Uliel et al. demonstrated, by microcavity enhancement Raman measurements on the δ-phase, that the same bands could be related to weak Van der Walls interactions between corner I–Pb–I atoms with Cs ones.[49]

In this chapter, Raman spectroscopy is proposed as the ideal technique to rapidly identify different polymorphs and constantly monitoring phase transitions by in-situ measurements. The vibrational analysis of $CsPbI_3$ in the α-phase and δ-phase and of the Cs_4PbI_6 secondary phase is reported and all the vibrational modes are assigned by comparing experimental spectra of the phases to Raman modes calculated within the DFT framework. Finally, the mechanism of laser induced phase degradation was studied using in-situ Raman measurements providing new insights on the secondary phase generated during the process.

2.1 Experimental

2.1.1 Materials

Caesium iodide (CsI, 50 ppm alkali metals, 99,9%) was purchased from Alfa-Aesar, Lead iodide (PbI_2, 99%) was purchased from Sigma Aldrich. All chemicals were used without any further purification.

2.1.2 Synthesis

The $CsPbI_3$ and Cs_4PbI_6 samples were synthesized by a solid-state reaction of CsI and PbI_2. Stoichiometric raw materials were weighed, ground in an agate mortar, and then sintered in a furnace.

$$CsI + PbI_2 \rightarrow CsPbI_3$$

$$4CsI + PbI_2 \rightarrow Cs_4PbI_6$$

The stability is affected by oxygen and moisture, so the syntheses were performed under continuous vacuum conditions (experimental chamber pressure ~$8 \cdot 10^{-5}$ mbar). The samples were thermally treated at 400 ºC, using a warming ramp of 10 °C/min, for 10 minutes and 5 hours for the $CsPbI_3$ and the Cs_4PbI_6, respectively. Then, the samples were slowly cooled to room temperature.

2.1.3 Characterization

X-ray diffraction patterns at room temperature were collected by using a Rigaku Miniflex II diffractometer with θ-2θ Bragg-Brentano geometry with Cu Kα (λ = 1.5418 Å) radiation at room temperature. The powder patterns were recorded in the $5º \leq 2\theta \leq 45º$ range. High temperature measurements were performed with a Bruker D8 Advance diffractometer operating at 30 kV and 20 mA, equipped with a Cu tube (λ = 1.5418 Å), a Vantec-1 PSD detector, and an Anton Parr HTK2000 high-temperature furnace. The powder patterns were recorded in the $21° \leq 2\theta \leq 45°$ range. To avoid the evaporation of the powder at high temperature, the sample was sealed in Kapton.

Raman measurements were carried out in backscattering geometry by exciting the samples at 532 nm with a wavelength stabilized diode module (LASOS – GLK series-532) coupled with a Reflecting Bragg Grating (Optigrate-Braggrade 532) to narrow the laser line. Measurements were performed at room temperature with a triple spectrometer Jobin-Yvon Dilor integrated system with a spectral resolution of about 1 cm^{-1}. Spectra were recorded in the Stokes region by a 1200 groove/mm grating monochromator and a liquid N-cooled charge coupled device (CCD) detector system.

Steady-state photoluminescence measurements were performed with 405 nm laser excitation (Ondax LM-405-PLR-40-1) coupled with an optical fiber to an Avantes Sensiline Avaspec-ULS-TEC Spectrometer. The measurements were acquired with 1 s time window in a 300–800 nm spectral range.

The absorption measurements were obtained by diffuse reflectance spectroscopy utilizing a UV-Vis-NIR Agilent Technologies Cary 5000. Measurements were performed by using a PbS solid state photodetector using KBr as reference. The reflection configuration measures the diffuse reflection of sample with respect to a reference sample which is considered to have a 100% reflectivity. The Kubelka-Munk equation was applied to calculate the absorption properties.

Density-functional theory (DFT) calculations were carried out using Quantum Espresso,[50] an integrated suite of open-source computer codes for electronic-structure calculations and material modelling based on density-functional theory, plane waves, and pseudopotentials. We used the generalized gradient approximation (GGA) in the Perdew–Burke–Ernzerhof version,[51] for the exchange correlation potential and norm-conserving Troullier-Martins pseudopotentials.[52] The electronic Kohn– Sham wave functions were expanded using a plane wave basis set, up to a kinetic

energy cut-off of 70 Ry. As for the k-points, we considered an 8x8x8 mesh of points distributed according to the Monkhorst–Pack algorithm within the first Brillouin zone of the reciprocal lattice. We calculated the Raman and IR spectra using Density Functional Perturbation Theory (DFPT),[53,54] as implemented in the Quantum-Espresso package.

2.1.4 Crystal structure and vibrational analysis

Four crystal phases are expected in the case of $CsPbI_3$: a black cubic phase (called α), a tetragonal one (β) and two orthorhombic polymorphs (γ phase and a non-perovskite yellow δ-phase). After heating the samples above 320 °C, the room temperature yellow phase (δ-phase) converts to the black α-phase, but when cooling down to room temperature the α polymorph doesn't return immediately to its original yellow phase.[13]

The α-phase is a perovskite structure, belonging to the space group number 221, *P m-3m* in the Hermann-Mauguin notation and O_h^1 in the Schönflies notation, with Z=1. The cubic $CsPbI_3$ perovskite can be described as consisting of I^- ions corner-shared by two $[PbI_6]^{4-}$ octahedra, with the Cs cation occupying the 12-fold coordination site in the middle of the cuboctahedron void. Cs atoms are in Wyckoff position *1a*, Pb atoms in *1b*, and I atoms in *3c*. Cesium and lead atoms occupy O_h sites, and the three iodine atoms lie in D_{4h} sites. Each ion in O_h gives rise to T_{1u} symmetry modes, and the three iodine atoms contribute with $2T_{1u} + T_{2u}$ modes.[55] The total reducible representation at the center of the Brillouin zone is $\Gamma = 4T_{1u} + T_{2u}$. One T_{1u} mode is acoustic and the others are optical modes. T_{1u} modes are IR active, T_{2u} are silent. Vibrational Raman modes are not expected for symmetry reasons.

The δ-phase is described by the space group number 62 (*Pnma*, or D_{2h}^{16}), with four formula units in the unit cell. The constituent ions, Cs^+, Pb^{2+}, I_1^-, I_2^-, I_3^- are in Wyckoff position 4c. The symmetry of each site is C_s. The contribution of each group of ions gives the reducible representation at the center of Brillouin zone $\Gamma = 10A_g + 5A_u + 5B_{1g} + 10B_{1u} + 10B_{2g} + 5B_{2u} + 5B_{3g} + 10B_{3u}$.[55] One of B_{1u}, B_{2u}, B_{3u} is acoustic, the others are optical modes. The A_u modes are silent, B_{1u}, B_{2u}, B_{3u} are IR active, A_g, B_{1g}, B_{2g}, B_{3g} are Raman active.

To better understand the relationship between the two phases we can consider the $[PbI_6]^{4-}$ ion. To a first approximation, $[PbI_6]^{4-}$ has an octahedral structure and Figure 1 illustrates the six vibrational modes of an octahedral XY_6 molecule: the A_{1g}, E_g, T_{2g} vibrations are Raman-active, the T_{1u} ones are infrared-active, the T_{2u} are silent.[56] The vibrational modes that are active in a molecule can be inactive when the molecule is part of a crystal. For reason of symmetry, A_{1g}, E_g, T_{2g} modes are not active in the α-$CsPbI_3$. In the orthorhombic δ-$CsPbI_3$ the octahedra do not form any longer a 3D-

chain but a 1D-chain and the octahedra are distorted: this symmetry lowering activates Raman modes and induces a splitting of degenerate vibrations, as indicated in the insert in Figure 1.

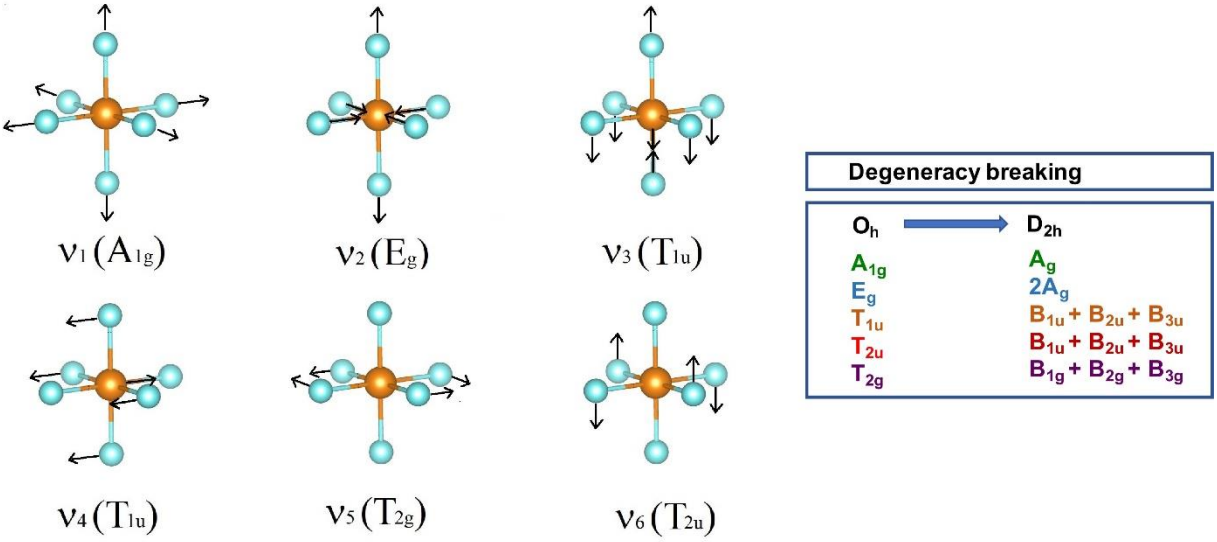

Figure 1: Normal modes of octahedral XY_6 molecules. Conversion from O_h to D_{2h} and relative degeneracy breaking.

Cs_4PbI_6 secondary phase can be obtained from the $CsPbI_3$ primary compound under specific circumstances. The two crystals are quite different from the structural point of view. The Cs_4PbI_6 belongs to the space group number 167 (*R-3c:H*, or D_{3d}^6), with Z=6. The $[PbI_6]^{4-}$ octahedra are surrounded by eight Cs^+ atoms, but I^- atoms are no longer shared between two octahedra, and Cs^+ atoms occupy two different crystallographic sites. Cs atoms are in Wyckoff position *6a* and *18e*, Pb atoms in *6b* and I atoms in *36f*. Cesium atoms occupy D_3 and C_2 sites, Pb atoms occupy S_6 sites, and I atoms lie in C_1 sites. The total reducible representation at the center of the Brillouin zone is $\Gamma = 4A_{1g} + 5A_{1u} + 6A_{2g} + 7A_{2u} + 10E_g + 12E_u$.[55] One of the A_{2u} and one of E_u modes are acoustic, the others are optical modes. A_{2u} and E_u are IR active, whilst A_{1g} and E_g are Raman active. Figure 2a shows the sketch of $CsPbI_3$ structure, in the two phases α and δ. Figure 2b reports the sketch of Cs_4PbI_6 structure. From the above reported analysis, it is clear that the vibrational spectra allow distinguishing the two crystals (*vide infra*).

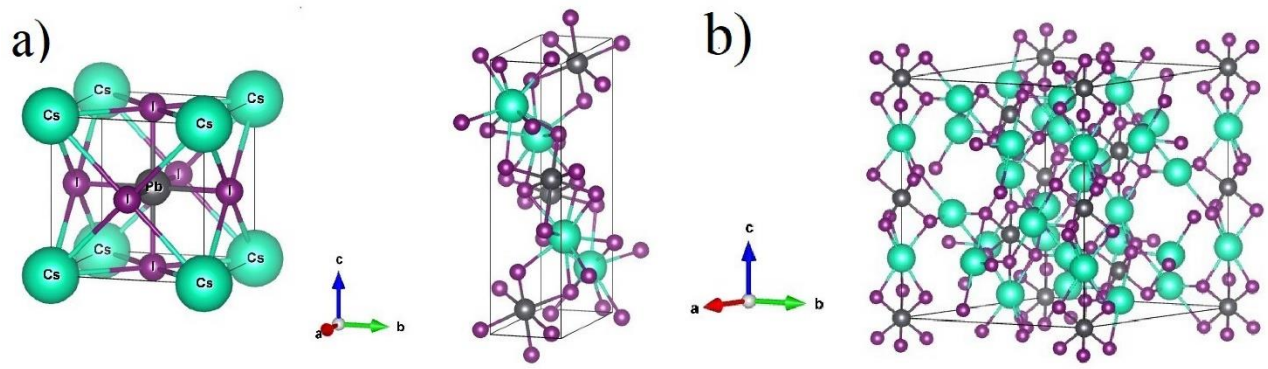

Figure 2: a) Sketch of $CsPbI_3$ structure. On the left α-phase, on the right δ-phase. b) Sketch of Cs_4PbI_6 structure.[57]

2.2 Results and discussion

2.2.1 X-ray and optical measurements

The crystal structures were confirmed by X-ray diffraction measurements. The patterns of δ-$CsPbI_3$ and Cs_4PbI_6 were gathered at room temperature, the one of the α-$CsPbI_3$ at 400 °C. Figure 3a reports the experimental XRD pattern and the Rietveld analysis of the yellow δ-$CsPbI_3$ sample (ICSD 27979) obtained from the synthesis of *$CsI+PbI_2$*. The lattice parameters obtained for this sample are *a=9.921(2)* Å, *b=4.554(3)* Å, *c=16.86(3)* Å, with R factors: *R_{wp}=11.83%*, *R_{exp}=7.51%*, *R_B=9.62%*.
The measurements at high temperature (Figure 3b) confirm the presence of α-$CsPbI_3$, with lattice parameter *a=6.218(1)* Å (ICSD 161481). It is also present, in the pattern, the platinum peak at 40°, deriving from the sample-holder, and a small percentage of δ-phase. It is to be noted that the sealing Kapton, being amorphous, has a broad peak below 21°, which doesn't affect the diffraction pattern, although the presence of this layer has the effect of reducing the signal-to-noise ratio. For this reason, the reported pattern is a bit noisy.
In Figure 3c it is reported the analysis of the sample deriving from the synthesis of *$4CsI+PbI_2$*. The pattern reveals the presence of Cs_4PbI_6 sample up to 74% by weight, with a residual contribution of CsI precursor (20%) and 6% by weight of δ-$CsPbI_3$. The lattice parameters of Cs_4PbI_6 are *a=14.609(1)* Å, *c=18.36(5)* Å, with R factors: *R_{wp}=12.19%*, *R_{exp}=7.85%*, *R_B=9.32%*.

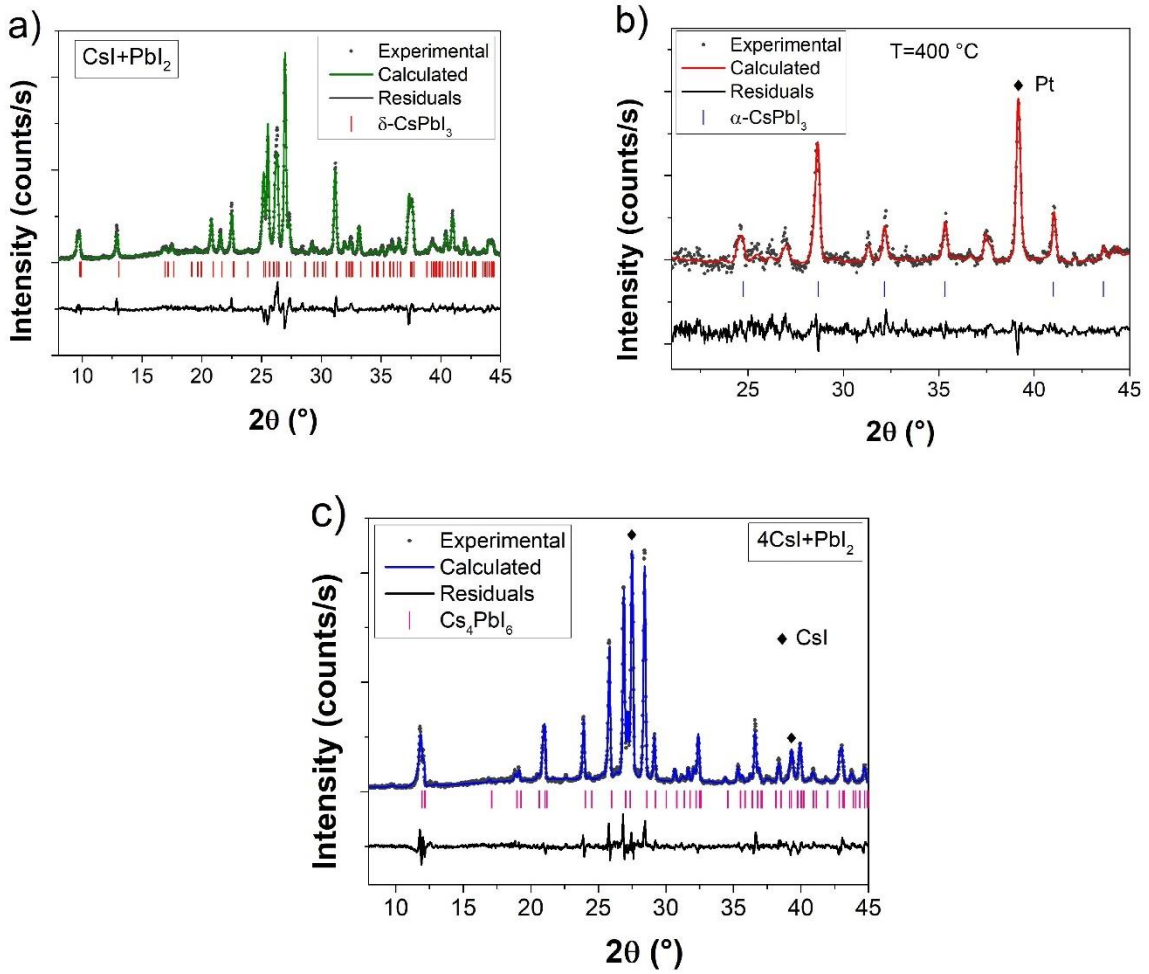

Figure 3: a) Rietveld refinement and theoretical pattern of δ-$CsPbI_3$. b) Rietveld refinement on the measurement at high temperature and theoretical pattern of α-$CsPbI_3$. c) Rietveld refinement and theoretical pattern of Cs_4PbI_6.

Figure 4 reports the absorption and steady-state photo-luminescence spectra collected on the samples of $CsPbI_3$. The spectra confirm the success of the synthesis, showing the optical features of α and δ phases.[58,59] In particular, the former shows a highly efficient and narrow emission at 715 nm, the latter a broad and weak emission around 550 nm.

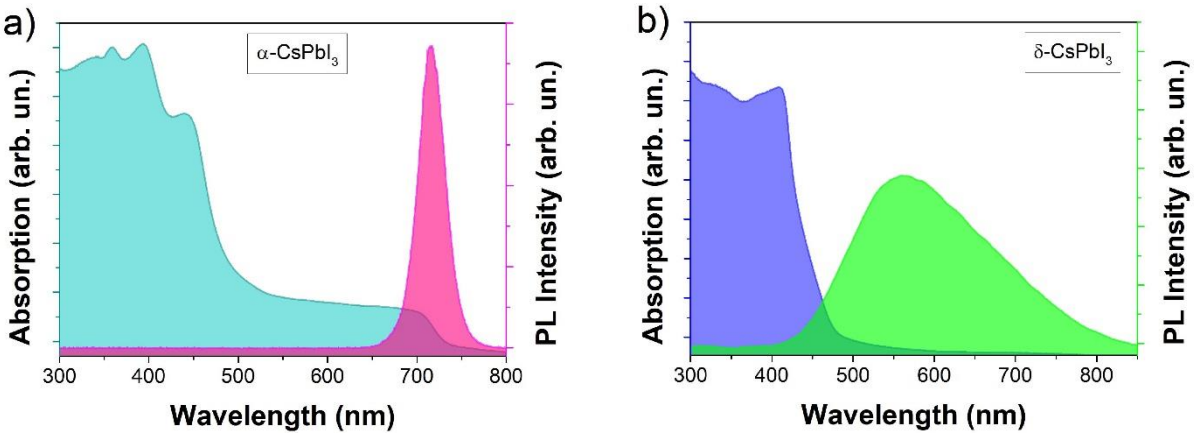

Figure 4: a) Absorption and steady-state PL spectra of α-$CsPbI_3$ excited at 405 nm. b) Absorption and steady-state PL spectra of δ–$CsPbI_3$ excited at 405 nm.

2.2.2 Raman measurements and simulation

For the α-$CsPbI_3$ and δ-$CsPbI_3$ structures, we considered simulation cells containing 5 and 20 atoms respectively. The initial structures obtained from single crystal data were fully optimized to the equilibrium positions with forces smaller than 0.001 eV/atom to a target pressure smaller than 0.5 kbar. The corresponding optimized lattice parameter for the cubic α-$CsPbI_3$ structure was equal to a=6.39 Å which is identical to the value previously obtained with DFT-GGA calculations [60] and in good agreement with the experimental value obtained by X-ray measurements. For the orthorhombic δ-$CsPbI_3$ structure, the DFT lattice parameters were a= 10.73 Å, b=4.90 Å and c=18.24 Å, in perfect agreement with previous DFT calculations [61] and in agreement with the experimental values obtained by X-ray measurements.

As already stated in the previous paragraphs, the selection rules point out that no vibrational Raman modes are allowed in the cubic α-$CsPbI_3$ for symmetry reasons and the experimental Raman spectrum, collected on the black α-phase sample, does not show any Raman features.

In Figure 5 the experimental Raman spectrum of the sample δ-$CsPbI_3$ is reported together with the curve fitting and the vibrational modes computed by DFT simulation.

A single molecule vibrates at a well-defined frequency, but each molecule is surrounded by interacting neighbours. The observed line shape is the result of these interactions. The relaxation time from the excited state to the ground state is due to two contributions: the amplitude correlation time (τ_a), related to the single molecule, and the coherence lifetime (τ_c), related to the motion of the environment. In the case of solids, the coherence lifetime is the main contribution and the line shape has mainly a Gaussian profile. In the case of gases, coherence is easily lost and the main contribution is due to the amplitude correlation time, so that the line shape has mainly a Lorentzian profile.[62] We fitted the experimental spectrum by a multiple peak fitting procedure, with a Pseudo-Voigt function, combination of Gaussian and Lorentzian profile:

$$y = y_0 + A\left[m_u \frac{2}{\pi}\frac{w_L}{4(x-x_C)^2 + w_L^2} + (1-m_u)\frac{\sqrt{4ln2}}{\sqrt{\pi}w_G} e^{-\frac{4ln2}{w_G^2}(x-x_C)^2}\right]$$

where m_u represents the Lorentzian character of the Voigt profile, w_L and w_G are the width parameters of the Lorentzian and Gaussian components, respectively.

Eight peaks were individuated at 47, 54, 58, 65, 84, 96, 107 and 115 cm^{-1}. All the fit parameters are reported in Table 1.

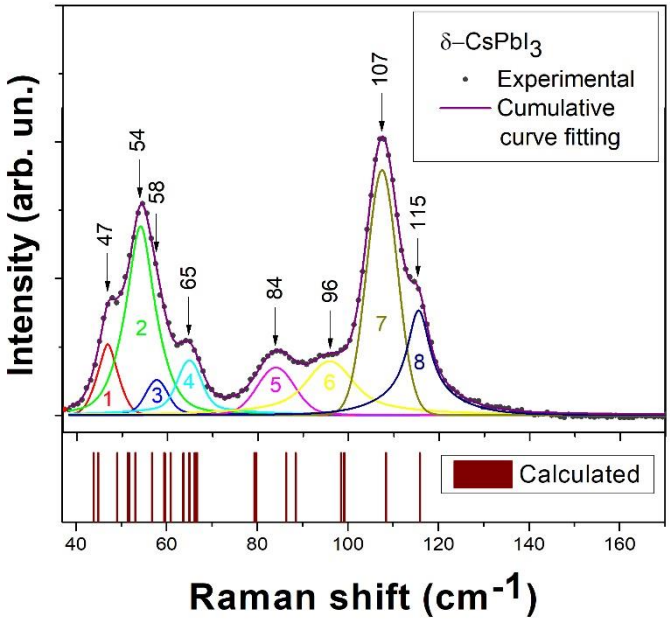

Figure 5: Raman spectrum of δ-CsPbI$_3$, excitation 532 nm. Numbers from 1 to 8 refer to the peaks fit. For comparison the calculated modes are reported.

Table 1: Fit parameters of multiple curve fitting in δ–CsPbI$_3$ Raman spectrum.

	y_0	x_c	A	w_G	w_L	m_u
Peak 1	0	46,82	6276,93	6,15	2,99	0,21
Peak 2	0	54,05	28074,96	10,02	6,26	0,60
Peak 3	0	57,65	4593,73	5,51	24,50	0,40
Peak 4	0	64,84	8993,35	5,82	21,87	0,55
Peak 5	0	83,96	7886,23	9,57	23,27	0,14
Peak 6	0	95,86	16536,93	9,85	20,52	0,74
Peak 7	0	107,39	30744,7	8,12	4,30	0,03
Peak 8	0	115,46	17110,68	20,48	6,17	0,76

As stated above, δ-CsPbI$_3$ has 30 Raman-active modes. Caesium, lead and iodide are heavy atoms, so their vibrations are expected at low Raman shifts. In particular, the Raman peaks are in the range 45-120 cm^{-1} (due to the notch filter, we cannot observe peaks at frequencies smaller than 40 cm^{-1}).

It is possible to divide the spectrum into two principal regions, around the main peaks at 54 and 107 cm^{-1} respectively. The mean distance between caesium and iodine atoms is around *3.95* Å, whilst the one between lead and iodine atoms is around *3.24* Å (ICSD 27979), indicating that the interactions between lead and iodine are stronger than the ones between caesium and iodine atoms. Therefore, it is expected that the Cs-I vibrations are located at lower frequencies with respect to the Pb-I vibrations. DFT calculations confirm these observations and assign the main Raman features. The main vibrations are sketched in Figure 6 and the assignation of experimental Raman peaks is reported in Table 2. The whole vibrational modes are reported in Figure 7. The peaks above 80 cm^{-1} mainly concern vibrations of lead and iodide atoms, whilst below 80 cm^{-1} also caesium vibrations are involved. The strongest peak at 107 cm^{-1} is assigned to a symmetric A_g mode (Figure 6a), the shoulder at 115 cm^{-1} to an asymmetric B_{2g} mode (Figure 6b) and the peak at 96 cm^{-1} to the convolution of two modes, A_g and B_{2g} (n. 3 and 4 in Table 2). In these modes, caesium atoms are at rest and the atoms in the $[PbI_6]^{4-}$ octahedra vibrate. The other peaks are considered as the convolution of different vibrations. The peak at 84 cm^{-1} is assigned to the convolution of four modes, B_{2g}, A_g, B_{1g} and B_{3g} (n. 5- 8 in Table 2), where mainly lead and iodide atoms vibrate, whilst caesium atoms are involved in small vibrations. The peak at 64 cm^{-1} is considered the convolution of B_{1g}, B_{2g} and two A_g modes (n. 9- 12 in Table 2). The peak at 47 cm^{-1} is the convolution of a A_g, B_{2g} and B_{3g} modes (n. 20, 21 and 22 in Table 2). The region around the second strongest peak, 54-58 cm^{-1}, includes wide vibrations of caesium and iodide atoms: B_{1g}, B_{2g}, B_{3g} and A_g modes (n. 13-19 in Table 2). In particular, A_g and B_{2g} modes involve vibrations of Cs-I, whilst lead atoms are at rest (Figure 6c and d), and the A_g mode in Figure 6e regards strong vibrations of caesium.

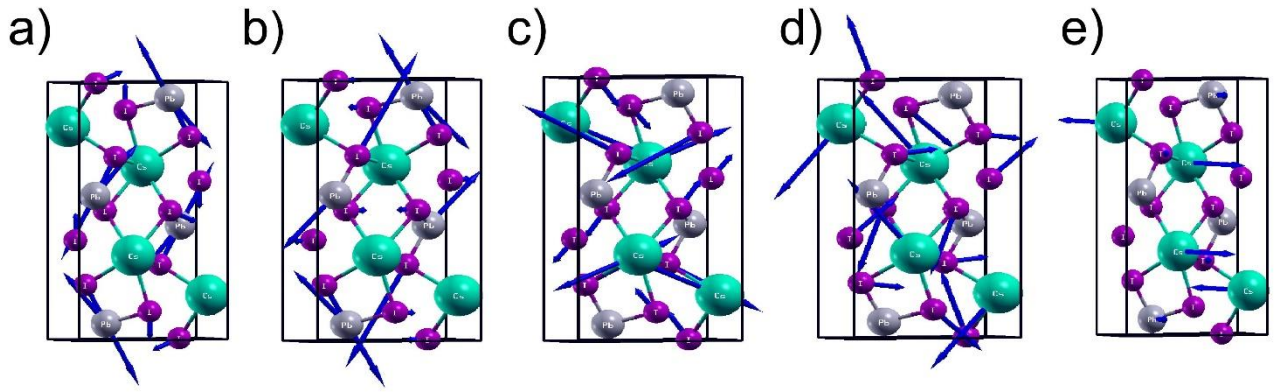

Figure 6: Assignation of Vibrational modes. a) A_g mode, n. 2 table 2 (107 cm^{-1}); b) B_{2g} mode, n. 1 table 2 (115 cm^{-1}) ; c) A_g mode, n. 9 table 2 (64 cm^{-1}) ; d) B_{2g} mode, n. 16 table 2 (54 – 58 cm^{-1}) ; e) A_g mode, n. 17 table 2 (54 – 58 cm^{-1}).

Table 2: Calculated Raman modes and assignation.

Mode number	Vibrational mode	Calculated Raman Shift (cm^{-1})	Experimental Raman shift (cm^{-1})
1	B_{2g}	115.9	115
2	A_g	108.4	107
3	A_g	99.2	96
4	B_{2g}	98.5	
5	B_{2g}	88.5	84
6	A_g	86.4	
7	B_{3g}	79.8	
8	B_{1g}	79.4	
9	A_g	66.7	64
10	B_{2g}	66.2	
11	A_g	65	
12	B_{1g}	63.7	
13	B_{2g}	60.9	54-58
14	B_{3g}	59.6	
15	B_{1g}	59.5	
16	B_{2g}	56.8	
17	A_g	53.1	
18	B_{2g}	51.7	
19	B_{3g}	51.4	
20	A_g	49.1	47
21	B_{3g}	44.9	
22	B_{2g}	43.9	
23	A_g	38,9	
24	B_{1g}	38,2	
25	B_{3g}	36,8	
26	B_{2g}	33	
27	B_{2g}	28,3	
28	A_g	27,3	
29	B_{1g}	16,2	
30	A_g	13,5	

a)

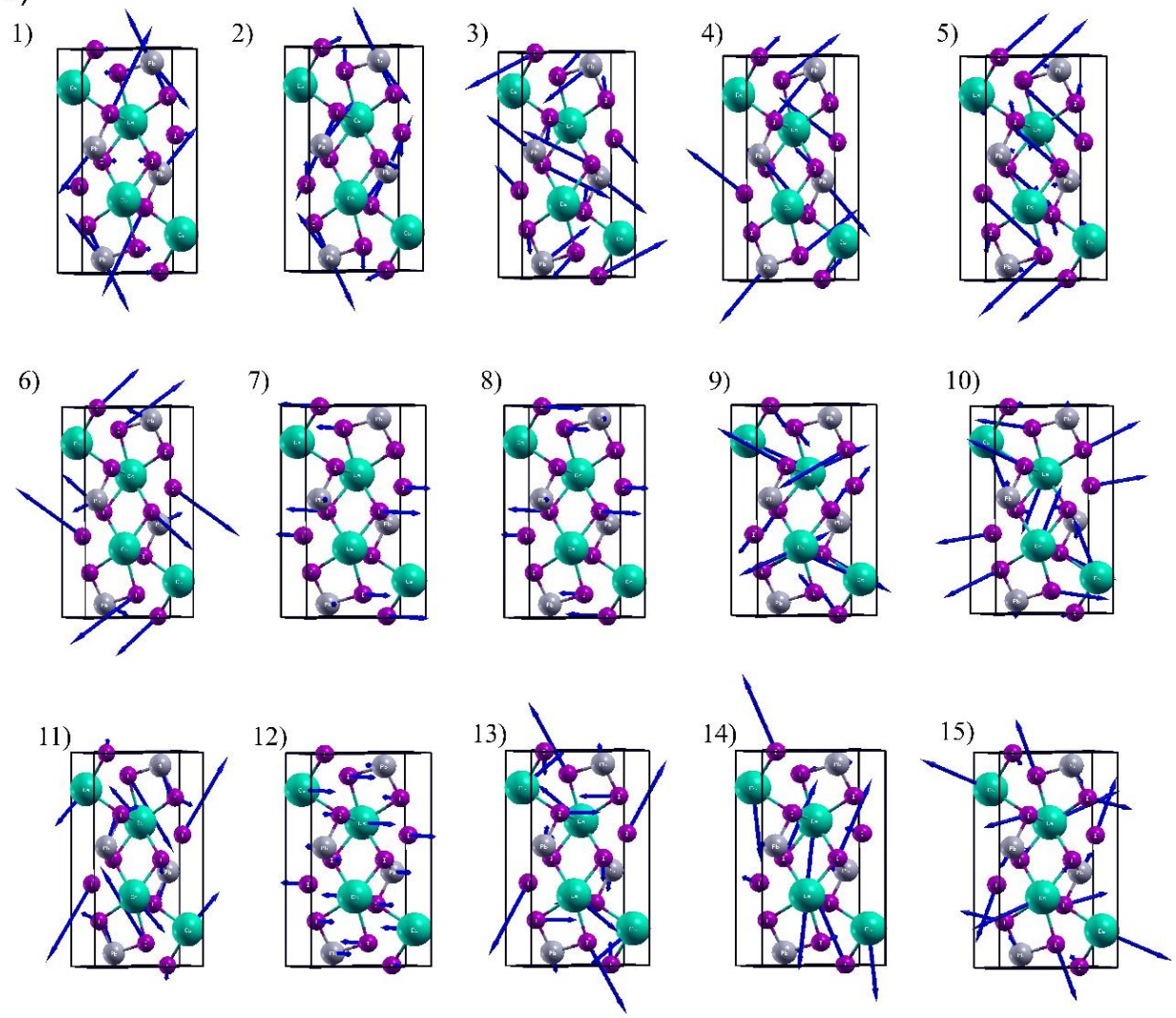

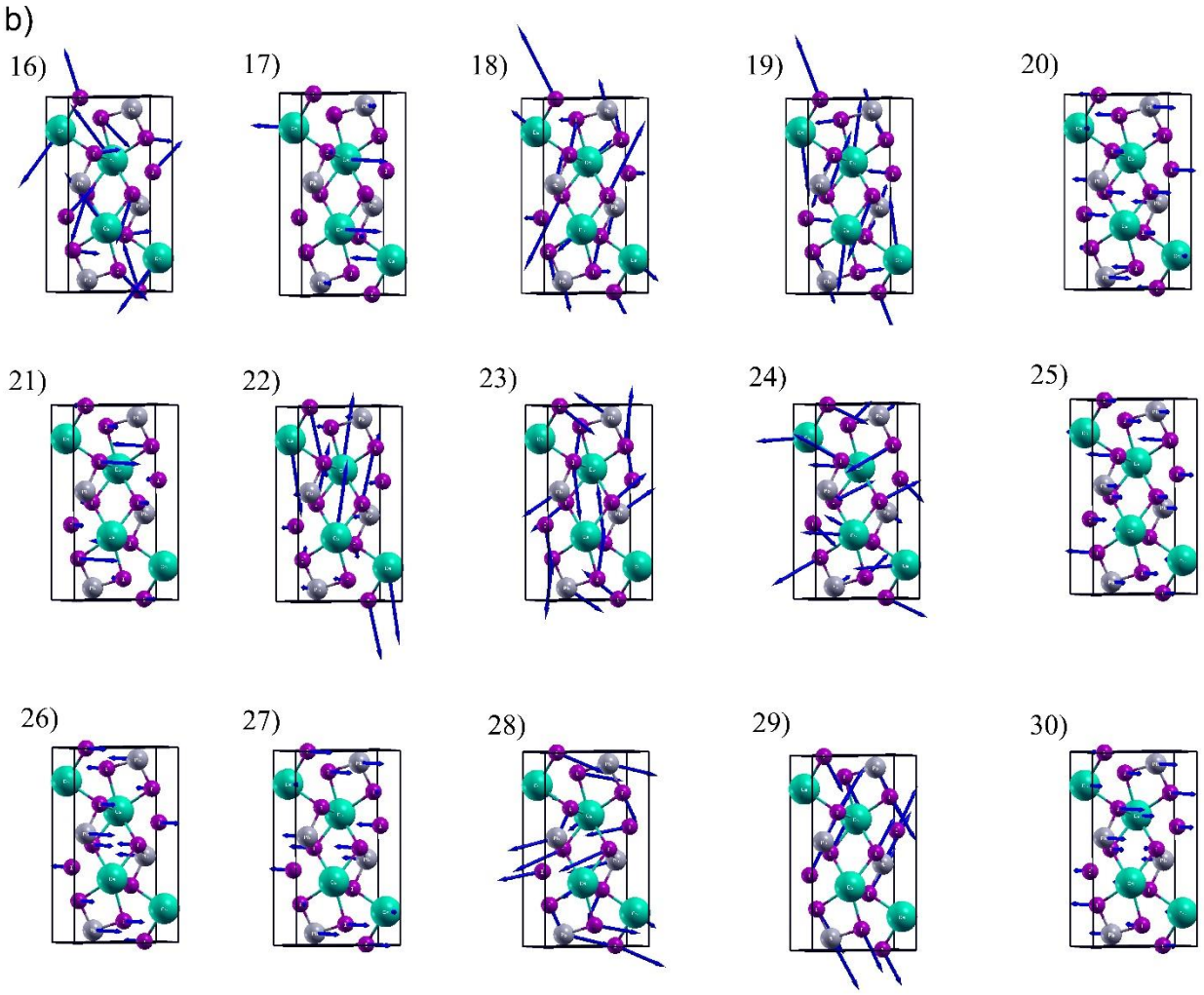

Figure 7: a) and b) Illustration of Raman modes calculated by DFT.

It was already observed that a high-power laser beam can degrade the stability of perovskite samples.[46,63,64] Thus, one should take care of controlling the experimental conditions in order to avoid the reported degradation when performing Raman and luminescence measurements. To perform in-situ measurements, we aligned the Raman and luminescence set-up to exploit the same microscope system to collect both the signals from the sample. Once the sample reached 320°C and the synthesis was accomplished, the sample was placed under the microscope to collect the luminescence and Raman signal. Indeed, carrying out the Raman and photoluminescence measurements, by increasing the power of the laser, we observed an abrupt decrease in the luminescence signal (the laser density power was increased up to 955 mW/mm^2). Thanks to the previous analysis on the vibrational modes, we were able to study the degradation phenomenon by means of Raman spectroscopy.

In Figure 8a three Raman spectra related to this process are reported, the spectra being recorded at zero irradiation time and after 10 and 30 seconds of laser irradiation (taking into account the short time considered we assume that the sample temperature kept almost constant). Figure 8b reports the

static luminescence measurements (excitation wavelength 405 nm) recorded, simultaneously, with the Raman spectra.

As expected, being recorded at room temperature, the sample presents a mixed structure: the zero-irradiation time PL spectrum, taken with very small laser power density (50 mW/mm^2), indicates the presence of α-phase (at naked eye the sample appeared indeed black). On the other hand, the Raman spectrum already reveals the presence of the δ-phase. It is important to recall that the cubic α-phase doesn't generate any Raman feature and the fast phase transition from α to δ-phase at room temperature is well documented. After 10 seconds of irradiation, the Raman signal related to the δ-phase remain constant (as suggested by the peak at 107 cm^{-1}) but two vibrational features at 65 and 90 cm^{-1} increase their relative intensity. The latter could still recall for the Raman bands related to the δ–$CsPbI_3$ phase (see Figure 5 and Table 2), but they have different relative intensity with respect to the other bands, and, mainly, appear at slightly red-shifted positions (at 65 and 90 cm^{-1} instead of 54 and 84 cm^{-1}). We also noticed that the relative contribution of the band at 90 cm^{-1} is larger than the one of 84 cm^{-1} band in Figure 5. As the irradiation proceeds, the 107 cm^{-1} band remains still constant, but the formation of two new peaks at 136 and 270 cm^{-1} is clearly visible. These last two peaks are assigned to lead oxide.[65] The luminescence collected simultaneously drops swiftly to zero, strongly suggesting the full degradation of the α-phase and its absence after 30 second under illumination.

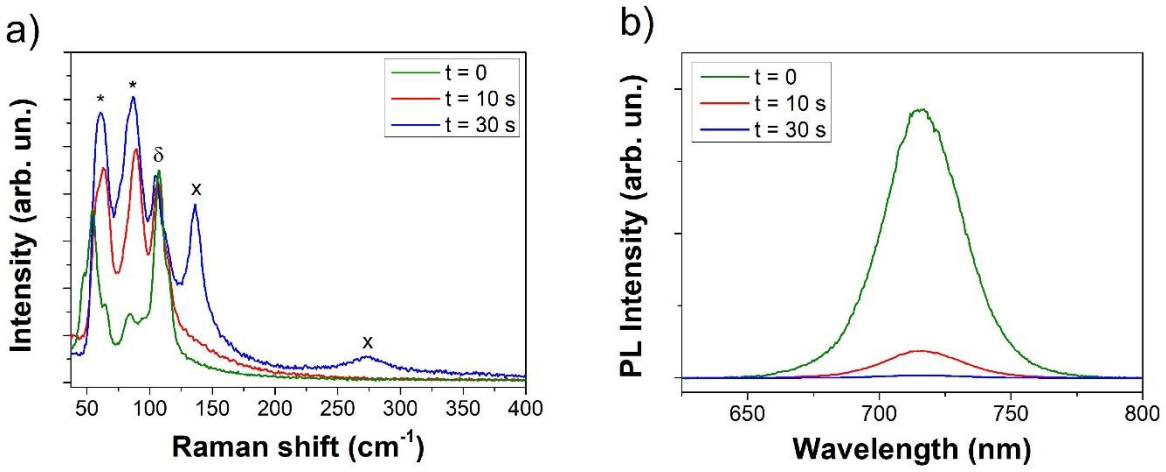

Figure 8: a) Raman spectrum of $CsPbI_3$ after laser degradation. The main peaks of the different phases are indicated in figure: (*) Cs_4PbI_6 phase, (δ) δ-$CsPbI_3$ phase, (x) PbO. b) Luminescence collected simultaneously with the relative Raman spectrum.

In literature the synthesis process of α–$CsPbI_3$ from a secondary compound of caesium, lead and iodine, Cs_4PbI_6, is reported.[34] We hypothesize that an inverse process is activated by laser irradiation, leading from α–$CsPbI_3$ to Cs_4PbI_6:

$$4\,\alpha\,CsPbI_3 \rightarrow Cs_4PbI_6 + 3PbI_2$$

Lead iodide is unstable in ambient air under irradiation, because oxygen oxidizes the iodide with the formation of lead oxide and elemental iodine:[66,67]

$$2PbI_2 + O_2 \rightarrow 2PbO + 2I_2$$

To confirm the above considerations about the degradation process, pure Cs_4PbI_6 samples were synthesized (see Figure 3c and the crystal sketch reported in Figure 2b). Figure 9 reports the Cs_4PbI_6 Raman spectrum, characterized by two main peaks at 65 and 90 cm^{-1} allowing to confirm the aforementioned hypothesis, fully justifying both the spectral position and the relative contribution of the recorded bands in Figure 8a.

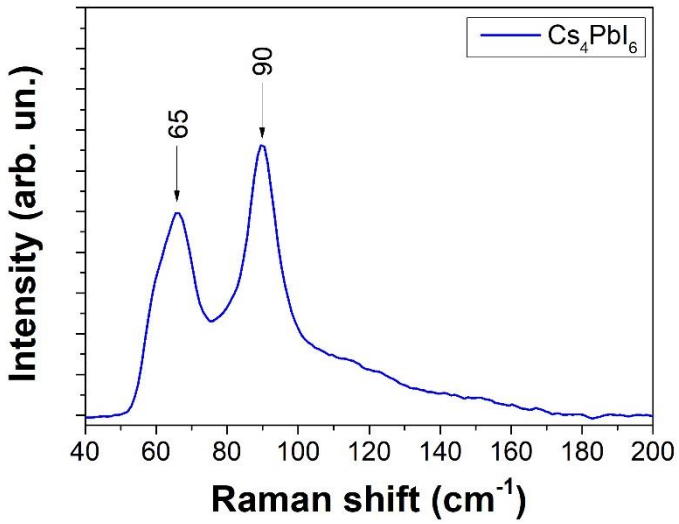

Figure 9: Raman spectrum of Cs_4PbI_6.

In view of these results it is possible to define the experimental Raman peaks of δ–$CsPbI_3$ and Cs_4PbI_6, completing and clarifying previous works.[45,49] Further, we showed that, for symmetry reasons, α-$CsPbI_3$ doesn't have allowed Raman modes.

2.3 Conclusions

The vibrational analysis of lead halide perovskites in the α-phase and δ-phase is reported. The analysis allowed to completely discriminate between the two crystal phases, being the cubic α-phase lacking in allowed Raman modes, because of symmetry reasons, and the orthorhombic δ-phase characterized by several distinctive bands. Corroborated by theoretical argumentations and DFT calculations, we were able to definitely assign the experimental Raman modes in δ–$CsPbI_3$.

Further, the analysis of the Raman modes was extended to the secondary phase, Cs_4PbI_6, allowing to successfully study, by in-situ measurements, the laser-induced phase degradation of α–$CsPbI_3$ with the formation of the secondary phase Cs_4PbI_6 and relative by-products.

Beyond the vibrational characterization, Raman spectroscopy was proven to be a fast and reliable experimental tool to characterize the different polymorphs of lead halide perovskites and to follow in-situ phase transitions or degradation processes caused by laser irradiation.

3 Formation Mechanisms and Phase Stability of Solid-State Grown $CsPbI_3$ Perovskites

Jessica Satta, Alberto Casu, Daniele Chiriu, Carlo Maria Carbonaro, Luigi Stagi and Pier Carlo Ricci

Nanomaterials 2021, 11, 1823.

DOI: 10.3390/nano11071823

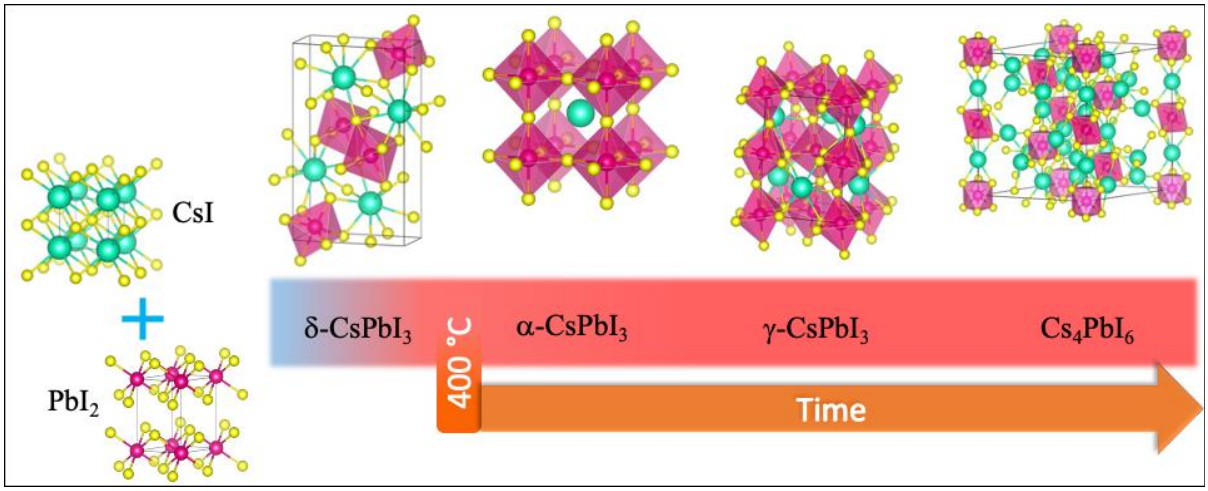

Different synthesis techniques have been applied to obtain high-quality samples, with solution deposition techniques being the most widely utilized because of their low-cost and easy processing. There are mainly two approaches in the synthesis of perovskites, either based on a one-step or a two-step procedure.[68,69] Mainly, dimethylformamide (DMF) and dimethyl sulfoxide (DMSO) are used as solvents, followed by a high-temperature annealing process. Solvent properties affect the quality of the film and, for this reason, antisolvent engineering or solvent evaporation control are used to promote the crystallization process.[70,71] Surface passivation strategies, the use of hydriodic acid or the so-called hydrogen lead iodide precursor are frequently employed to stabilize the cubic phase.[34,36,45] In a different approach, the cubic phase is achieved in solution by co-precipitation of monodisperse colloidal nanocrystals, with the stability being due to the large contribution of surface energy.[32] These methods require the use of long-chain organic capping agents and high boiling point solvents. It has been reported that the use of solvents and specific precursors can affect the synthesis, creating organic inclusions in a fully inorganic perovskite.[28] Alternatively, other methods allow to produce lead halide perovskites without the exploitation of capping ligands or solvents, namely gas phase deposition, mechanochemical synthesis and synthesis of single crystals.[47,72–74]

In this chapter, we focalize our studies on $CsPbI_3$ obtained through a one-step, solid-state reaction. This kind of synthesis is relatively simple and, most importantly, does not need the use of any solvent or ligand. This point is fundamental for clearly assessing the structural parameters that define the

stable phase and to determine how it is possible to achieve room-temperature, stable γ-phase $CsPbI_3$. On this basis, we investigated the formation of secondary phases using a multi-technique approach. X-Ray Diffraction (XRD) and Raman measurements, optical absorption, steady-time and time-resolved luminescence, as well as High-Resolution Transmission Electron Microscopy (HRTEM) imaging, were exploited to understand phase evolution as a function of synthesis time length. We pointed out the key role of stoichiometry in defining phase formation.

Nanoparticles with multiple, well-defined crystalline domains of different crystalline phases were observed, usually surrounded by a thin, amorphous/out-of-axis shell. By increasing the synthesis time length, in addition to the pure α phase, which was rapidly converted into the δ phase at room temperature, a secondary phase, Cs_4PbI_6, was observed, together with the 715 nm-emitting γ phase.

3.1 Material and Methods

3.1.1 Materials

Caesium iodide (CsI, 50 ppm alkali metals, 99.9%) was purchased from Alfa Aesar (Ward Hill, MA, USA) and lead iodide (PbI_2, 99%) was purchased from Sigma Aldrich (Saint Louis, MO, USA). All chemicals were used without any further purification.

3.1.2 Synthesis

$CsPbI_3$ and Cs_4PbI_6 samples were synthesized through a solid-state reaction of CsI and PbI_2. Stoichiometric raw materials were weighed, ground in an agate mortar and then sintered in a furnace.

$$CsI + PbI_2 \rightarrow CsPbI_3$$

$$4CsI + PbI_2 \rightarrow Cs_4PbI_6$$

Different synthesis processes were performed.

First, the samples were slowly heated at 10 °C/min up to 400 °C and treated at a constant temperature for 10 min. Next, the samples were slowly cooled to room temperature.

The same process was carried out multiple times, treating the samples at 400 °C for 1 hour, 5 hours, 10 hours, 17 hours and 24 hours, respectively, to study the effect of the synthesis duration on the final products. Hereinafter, the samples are called CPI3-10 m, CPI3-1 h, CPI3-5 h, CPI3-10 h, CPI3-17 h, CPI3-24 h. In order to discriminate the features of $CsPbI_3$ from those of the secondary phases, we synthesized pure Cs_4PbI_6. We repeated the previous procedure, treating the sample at 400 °C for 5 h. The resulting sample will be called C4PI6 in the following. As stated above, the stability was affected by oxygen and moisture, so the syntheses were performed in a continuous vacuum (~$8 \cdot 10^{-5}$ mbar).

3.1.3 Characterization

X-ray patterns were collected at room temperature, using a Rigaku Miniflex II diffractometer with θ-2θ Bragg–Brentano geometry with Cu Kα (λ = 1.54059 Å) radiation. The powder patterns were recorded in the $5° \leq 2\theta \leq 45°$ range. High temperature measurements were performed with a Bruker D8 Advance diffractometer operating at 30 kV and 20 mA equipped with a Cu tube (λ = 1.5418 Å), a Vantec-1 PSD detector (Freemont, CA, USA) and an HTK2000, Anton Paar (Graz, Austria) high-temperature furnace. The powder patterns were recorded in the $21° \leq 2\theta \leq 45°$ range. To avoid the evaporation of the powder at high temperature, the sample was sealed in Kapton.

Micro-photoluminescence and micro-Raman imaging spectroscopy were collected using an MS750 spectrograph (sol-instruments, Mink Belarus) equipped with different gratings (150 gr/mm and 1200 gr/mm for luminescence and Raman measurements, respectively). The laser beam (405 nm and 785 nm for luminescence and Raman, respectively) was focalized through an Olympus objective (100×) with a laser power of about 0.75 mW. The measurements were acquired within a 100 ms time window in a 300–800 nm spectral range.

The micro-PL–Raman measurements were carried out with backscattering geometry coupled with a reflecting Bragg grating (Optigrate-Braggrade 405 and 785, respectively). Measurements were performed at room temperature with a spectral resolution for the Raman measurements of 1 cm^{-1}.

Time-resolved photoluminescence (TR-PL) measurements were recorded by exciting the samples with 200 fs pulses sourced from an optical parametric amplifier (TOPAS-C, Light Conversion, Vilnius, Lithuania) pumped by a regenerative Ti:Sapphire amplifier (Coherent Libra-HE, Santa Clara, CA, USA). The repetition frequency was 1 kHz, and the TR-PL signal was recorded by a streak camera (Hamamatsu C10910) equipped with a grating spectrometer (Acton Spectra Pro SP-2300, Princeton Instruments , Trenton, NJ, USA). All the measurements were collected in the front-facing configuration to reduce inner filter effects. Proper emission filters were applied to remove the reflected contribution of the excitation light.

Excitation–emission fluorescence maps were recorded by a NanoLog spectrofluorometer (Horiba Jobin Yvon, Kyoto, Japan). Absolute quantum yields (QYs) were obtained by a quanta-ϕ-integrating sphere accessory with a 450 W Xenon lamp as the excitation source.

The absorption measurements were obtained by diffuse reflectance spectroscopy utilizing a UV-Vis-NIR Cary 5000, Agilent Technologies (Santa Clara, CA, USA). Measurements were performed using a PbS solid-state photodetector using KBr as reference. The reflection configuration measured the diffuse reflection of samples with respect to a reference sample, which was considered to have 100% reflectivity. The Kubelka–Munk equation was applied to define the absorption properties.

HR-TEM measurements were performed using a HRTEM JEOL 2010 UHR equipped with a Gatan imaging filter (GIF) with a 15-eV window and a 794 slow scan CCD camera. The structural characterization was conducted by 2-dimensional fast Fourier transform (2D-FFT) analysis, calculating planar and angular relationships between diffraction spots and comparing them with the diffraction cards previously adopted for X-ray diffraction analysis.

3.2 Results and Discussion

3.2.1 X-ray Diffraction Measurements

The phase stability of CPI3 samples at different temperatures is underlined in Figure 10. CPI3-10 m sample was obtained by solid state reaction with the correct stoichiometric amount of the precursors. Figure 10a reports the XRD pattern obtained at 400 °C in continuous vacuum, confirming the presence of α-$CsPbI_3$, with lattice parameter a = 6.218(1) Å (ICSD 161481). The sample was kept at 400 °C degree for 10 min and cooled down to RT, hence the XRD pattern was collected again (Figure 10b). The sample turns in colour from black to yellow and the Rietveld refinement on the X-ray diffraction pattern confirms the formation of the δ-$CsPbI_3$ structure: the peaks are attributed to the orthorhombic δ-$CsPbI_3$ (ICSD 27979), with crystal structure Pmnb (space group N. 62) and lattice parameters a = 4.7993(2) Å, b = 10.4521(6) Å, c = 17.7456(9) Å, with R_{wp} = 10.5% and R_B = 8%.

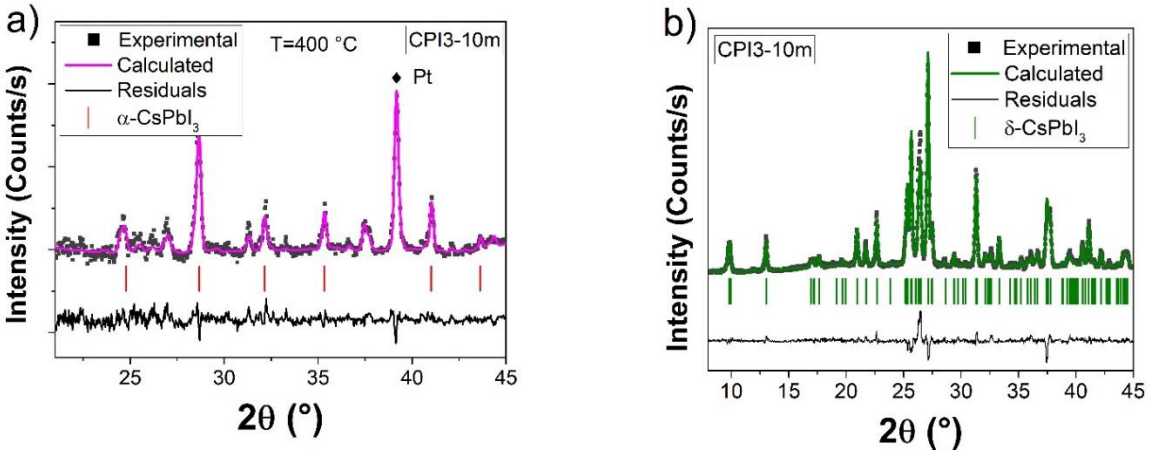

Figure 10: Rietveld refinement of sample CPI3-10 m at 400 °C (a) and at room temperature (b). ■ refers to Experimental pattern, colour line is the pattern calculated by Rietveld refinement, in Black line the residuals between experimental and calculated pattern, the vertical bar indicates the theoretical peaks characteristic of α and δ-$CsPbI_3$.

This result showed the possibility of rapidly synthesizing lead halide perovskites by solid-state reaction in the δ-$CsPbI_3$ phase, which converted to α-phase only at a high temperature, as already reported in a previous study.[75] The presence of unreacted precursors could be excluded by the XRD analysis, which highlighted the higher amount of CsI (not PbI_2) in samples with prolonged thermal treatment.

The XRD patterns of samples obtained by prolonged synthesis at 400 °C (CPI3-1 h, CPI3-5 h, CPI3-10 h, CPI3-17 h, CPI3-24 h) were collected once the samples were brought back to RT (Figure 11). Comparing these patterns with the one related to CPI3-10 m, the secondary phase Cs_4PbI_6 with crystal structure R-3c:H (space group number 167) was clearly observable in addition to the δ-$CsPbI_3$ phase. The percentages of these two phases were calculated by Rietveld refinement using the software MAUD (version 2.94, University of Trento, Italy).[76] The analysis evidenced that the percentage of Cs_4PbI_6 increased proportionally to the synthesis duration (Table 3).

Table 3: Results of Rietveld refinement on CPI3 samples at room temperature.

Time	**Phases**		**R_{wp}**	**R_B**
	δ-$CsPbI_3$	**Cs_4PbI_6**		
10 min	100%		10.5%	8.0%
1 h	90.6%	9.4%	12.1%	9.6%
5 h	54.9%	45.1%	12.6%	9.8%
10 h	42.1%	57.9%	13.6%	10.6%
17 h	33.2%	66.8%	12.8%	8.9%
24 h	21.5%	78.5%	17.6%	12.6%

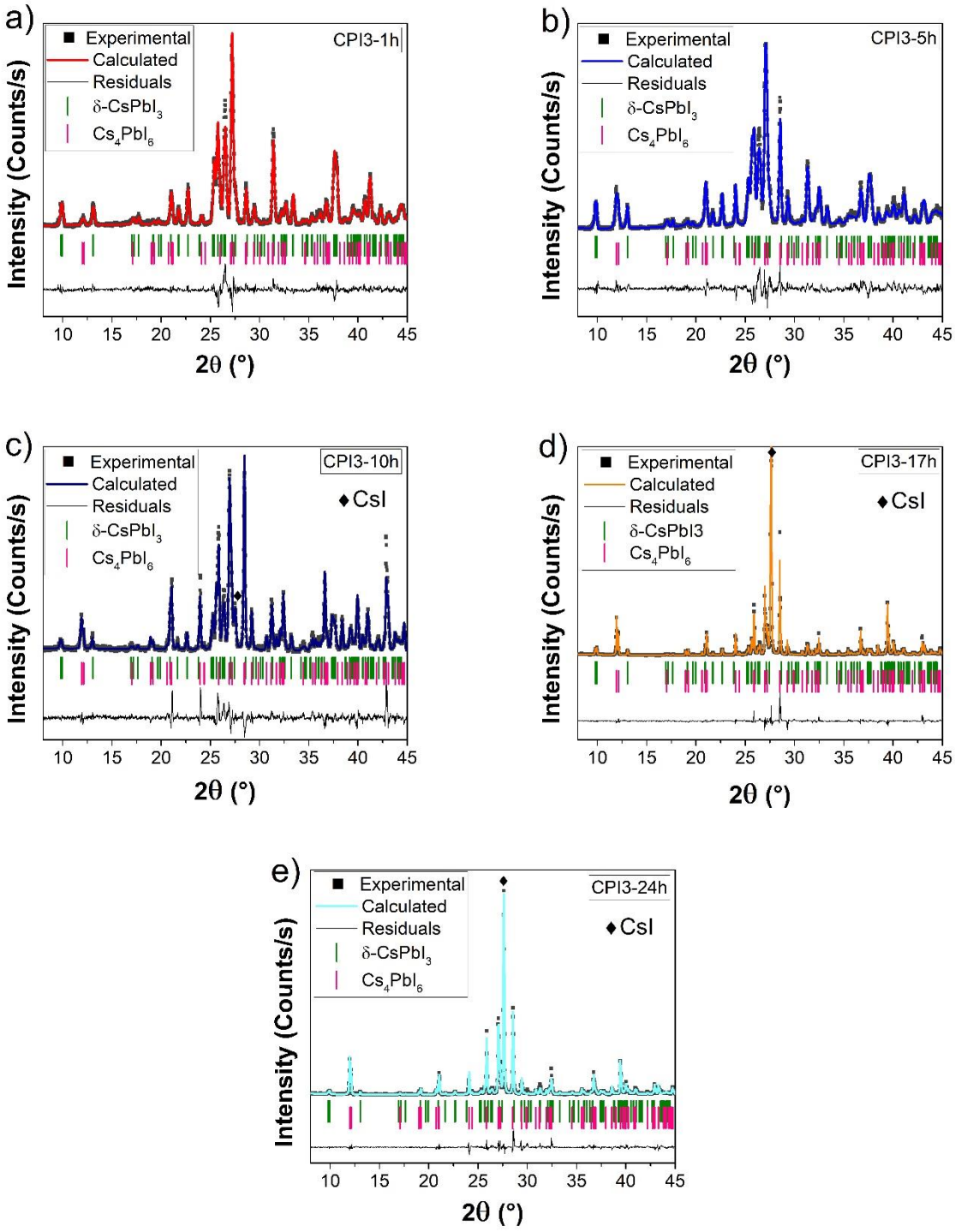

*Figure 11: Rietveld refinement of CPI3 samples at different times: (**a**) 1 h, (**b**) 5 h, (**c**) 10 h, (**d**) 17 h, (**e**) 24 h. ■ refers to Experimental pattern, colour line is the pattern calculated by Rietveld refinement, in Black line the residuals between experimental and calculated pattern, the vertical bar indicates the theoretical peaks characteristic of δ-$CsPbI_3$ and Cs_4PbI_6.*

Additionally, Figure 12 reports the Rietveld refinement of the C4PI6 sample obtained from the synthesis of 4CsI + PbI_2. The pattern revealed the presence of Cs_4PbI_6 up to 74% by weight, with a residual contribution of CsI precursor (20%) and 6% by weight δ-$CsPbI_3$. The lattice parameters of Cs_4PbI_6 were a = 14.609(1) Å and c = 18.36(5) Å with R factors R_{wp} = 12.19% and R_B = 9.32%.

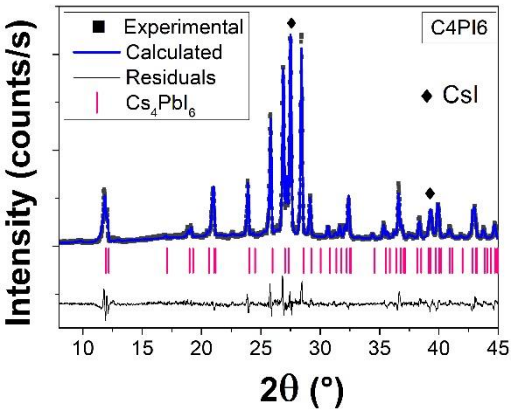

Figure 12: Rietveld refinement of C4PI6 sample. ■ refers to Experimental pattern, color line is the pattern calculated by Rietveld refinement, in Black line the residuals between experimental and calculated pattern, the vertical bar indicates the theoretical peaks characteristic of Cs_4PbI_6.

3.2.2 Luminescence and Raman Maps

To better understand the relation between the length of the synthesis and the presence of the secondary phase (Cs_4PbI_6), luminescence properties and Raman features were analysed.

The sample obtained after 10 min showed the typical PL of the δ phase, a broad and weak emission around 550 nm (Figure 13a). The absence of CsI in the XRD measurement of sample CPI3-10 m strongly suggests that the emission from unreacted CsI doped with Pb can be excluded (Figure 10). Increasing the synthesis duration, the luminescence started to become not uniform, and a strong emission appeared at around 715 nm, typical of black phases α and γ (Figure 13b).[32,59,77]

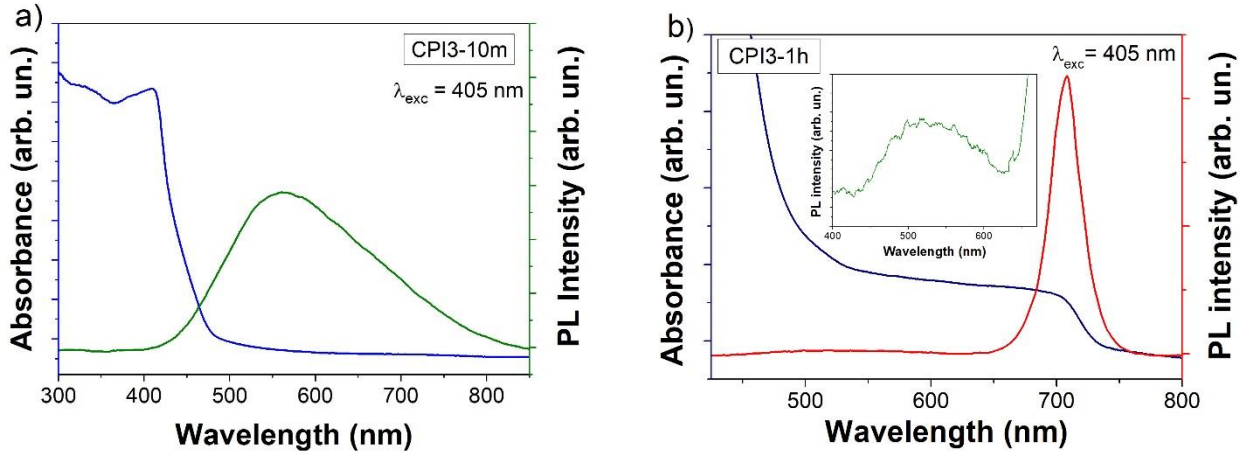

*Figure 13: Absorption and steady-state luminescence spectra of the sample CPI3-10m, respectively in blue and green (**a**) and of the sample CPI3-1h, respectively in blue and red (**b**). The inset in figure **b** shows a zoom of the range 400–670 nm.*

The broad emission from the δ-phase could be well reproduced with two gaussian contributions:

$$I = I_0 + A_1 e^{-\frac{(x-x_{c1})^2}{2w_1^2}} + A_2 e^{-\frac{(x-x_{c2})^2}{2w_2^2}}$$

With *A* amplitude, x_c the centre and *w* the width of the peak (Figure 14a). Retrieved parameters are reported in Table 4.

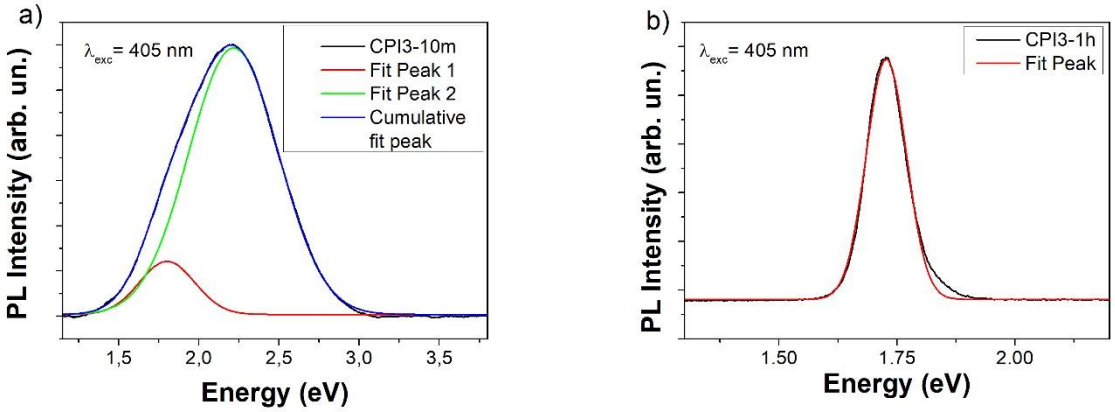

Figure 14: Gaussian Fit of the luminescence spectra collected on the samples a) CPI3-10m and b) CPI3-1h.

Table 4: Fit parameters of PL spectrum in figure 14a.

	A_i	**x_c (eV)**	**w (eV)**	**FWHM (eV)**
Peak 1	59 ± 3	1.802 ± 0.004	0.172 ± 0.003	0.406 ±0.008
Peak 2	294.5 ± 0.9	2.216 ± 0.003	0.280 ± 0.002	0.659 ±0.004

The red emission was the effect of a single band from the excitonic recombination in the α and γ phases (Figure 14b):

$$I = I_0 + Ae^{-\frac{(x-x_c)^2}{2w^2}}$$

Retrieved parameters are reported in Table 5.

Table 5: Fit parameters of PL spectrum in figure 14b.

	A_i	**x_c (eV)**	**w (eV)**	**FWHM (eV)**
Peak 1	4939 ± 9	1.72734 ± 0.00009	0.04240 ± 0.00009	0.0998 ±0.0002

Similar features were observed in the samples obtained by prolonged synthesis (Figure 15).

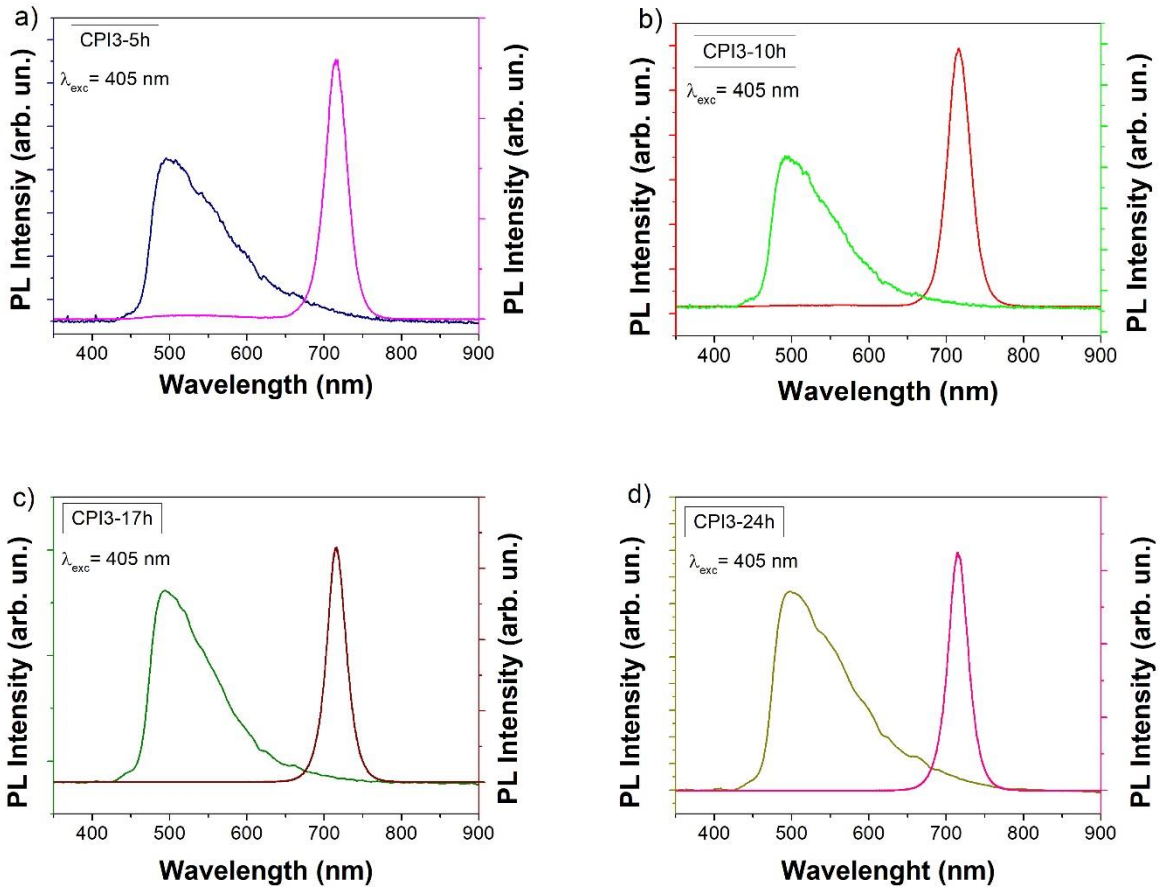

Figure 15: Steady-state luminescence spectra of two different points on the samples a) CPI3-5h, b) CPI3-10h, c) CPI3-17h and d) CPI3-24h.

Figure 15 shows steady-state luminescence spectra collected on different points of the samples CPI3-5h, CPI3-10h, CPI3-17h and CPI3-24h. The graphs confirm the inhomogeneity of the samples, showing that the luminescence is point-dependent. It's possible to observe a broad peak around 550 nm and a narrow one around 715 nm.

The local properties were, therefore, analyzed by optical microscope imaging coupled with a Raman and luminescence system. The samples appeared to be constituted of black spots surrounded by a white phase, mixed to a yellow phase.

The Raman spectrum collected on the black spots showed the presence of Cs_4PbI_6 (65 and 90 cm^{-1}) and δ-$CsPbI_3$ (55, 107 cm^{-1}). The yellow parts of the samples appeared to be δ-$CsPbI_3$ (Figure 16).[75]

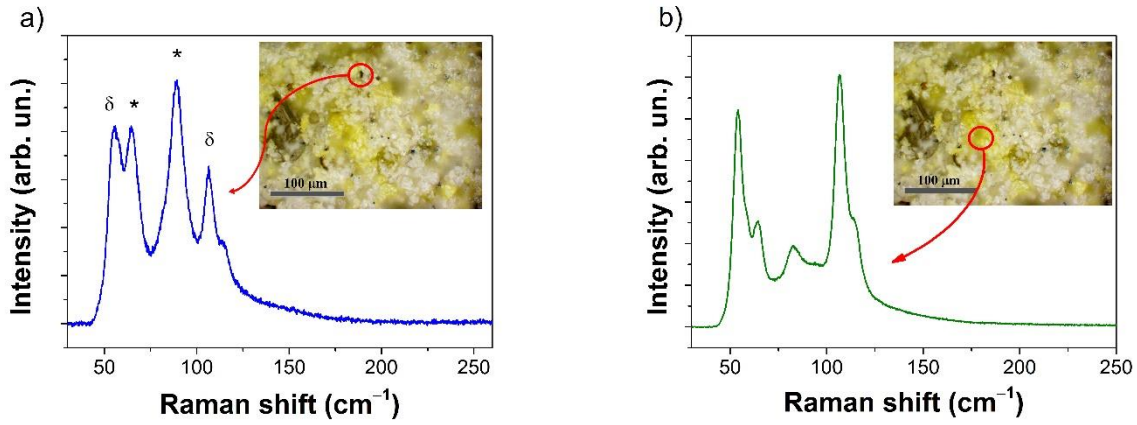

Figure 16 Raman spectra of CPI3-10 h sample, λ_{exc} = 785 nm. (a) Spectrum collected on a black spot, pointed out in the inset, with peaks in the Cs_4PbI_6 (*) and $CsPbI_3$ δ phases. (b) Spectrum gathered on the yellow part of the sample, pointed out in the inset. The images were obtained with optical microscope imaging.

Focusing our attention on the Photo Luminescence at 715 nm, we performed a luminescence map. Figure 17 correlates the PL map and the optical imaging. It is possible to notice how the emission is more intense in correspondence with the black spots.

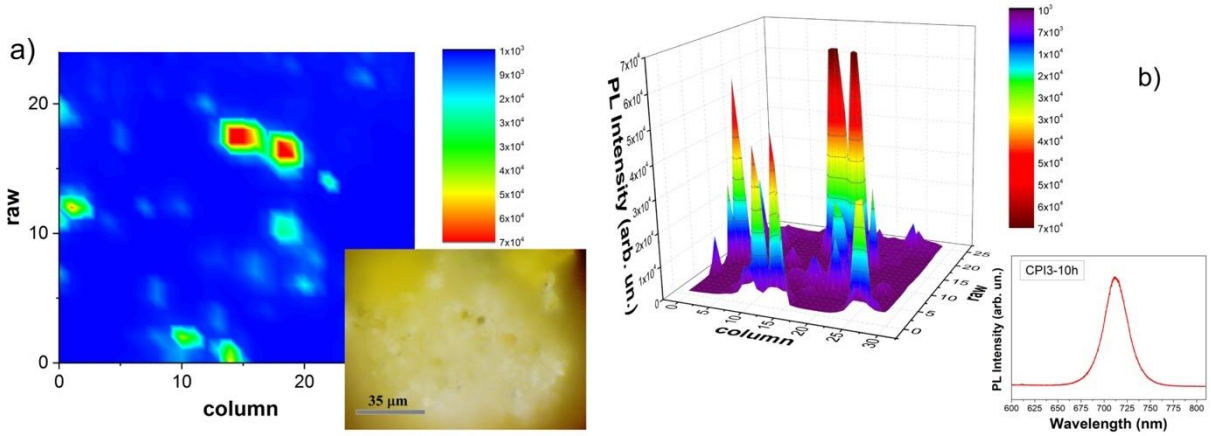

*Figure 17: Luminescence map of the emissions at 715 nm of the sample CPI3-10 h: in (**a**), a 2D map and, in the inset, the image through optical microscope and in (**b**), a 3D map and, in the inset, the PL emission spectrum.*

To better and deeper correlate the luminescence to a specific phase, we performed a series of measurements on 7 points (inset in Figure 18) close to an optically black point by simultaneously collecting Raman and luminescence spectra at each point. The black spot at point 1 showed an intense luminescence at 715 nm with a Raman spectrum typical of the γ-$CsPbI_3$ and peaks at 60 and 240 cm^{-1}.[47,78] Moving from the black spot to the yellow region, the luminescence at 715 nm decreased in intensity (Figure 18b,c). Simultaneously, in the Raman spectra (Figure 18a), it was possible to observe the appearance of the secondary phase, Cs_4PbI_6 (65 and 90 cm^{-1}), and finally, δ-$CsPbI_3$ (58, 107 and 115 cm^{-1}) with its related broad luminescence band at 550 nm.

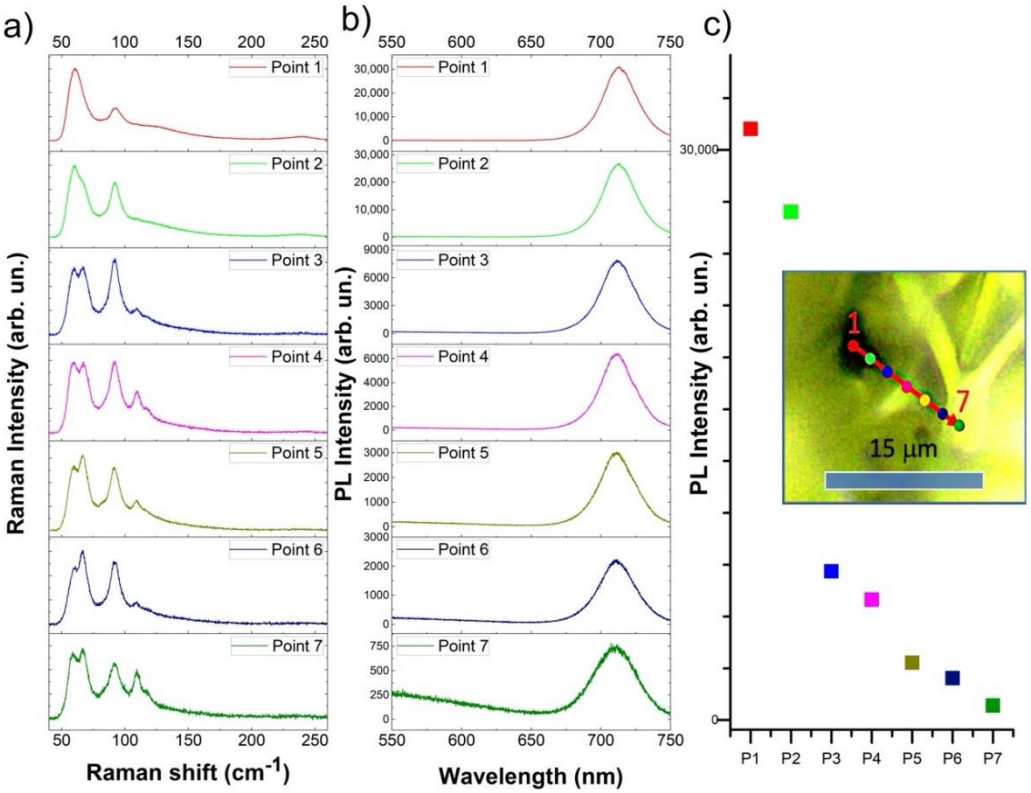

*Figure 18: Raman and luminescence measurements on seven points in the CPI3-10 h sample. (**a**) Raman spectra, (**b**) luminescence spectra and (**c**) 715 nm PL intensity. The spectra were collected at a spatial point indicated in the inset of panel (**c**). The colour relates the Raman and luminescence spectrum, the intensity of the peak at 715 nm and the point in the map.*

The quantum efficiency of the samples calculated at 715 nm, obtained by an integration sphere with a de-focalized beam, gave a general overview of the emission properties of the different samples (Table 6). In addition, considering that this red emission was related to a γ-phase, and it was well known that the quantum efficiency of this phase was close to unity,[79] it was possible to obtain an indirect rough estimation of the amount of γ-phase in the synthetized samples.

Table 6: Quantum yield vs. synthesis time.

Sample	**CPI3-1 h**	**CPI3-5 h**	**CPI3-10 h**	**CPI3-17 h**	**CPI3-24 h**
Synthesis time	1 h	5 h	10 h	17 h	24 h
Quantum yield	0.6 %	0.7 %	1.86 %	0.5 %	0 %

The values in Table 6 confirm the low amount of γ-$CsPbI_3$ deduced by X-ray diffraction measurements below the 1% detection limit.[79,80]

In Figure 19, the photoluminescence excitation/emission maps of the samples treated at different synthesis time are reported. In Figure 19a,b,c, three CPI3 samples are shown, while Figure 19d

displays, for comparison, the fluorescence map of the C4PI6 sample. Two different regions in the CPI3 samples could be clearly identified in the ultraviolet (UV) range (300–400 nm excitation, broad band 400–450 nm emission) and in the visible range (450–650 nm excitation, 715 emission). While the visible region was easily assignable to the γ-phase, the UV region could be assigned to the presence of the Cs_4PbI_6 phase by comparison with the map of the C4PI6 sample. However, due to the presence of CsI revealed by XRD measurements (see Figure 11 and Figure 12), whose emission properties lay in the same spectral range, a small amount of CsI:Pb could not be totally excluded [81]. Furthermore, the optical features of the δ-phase were not easily detectable, being overlapped by the broad emission of the Cs_4PbI_6 phase.

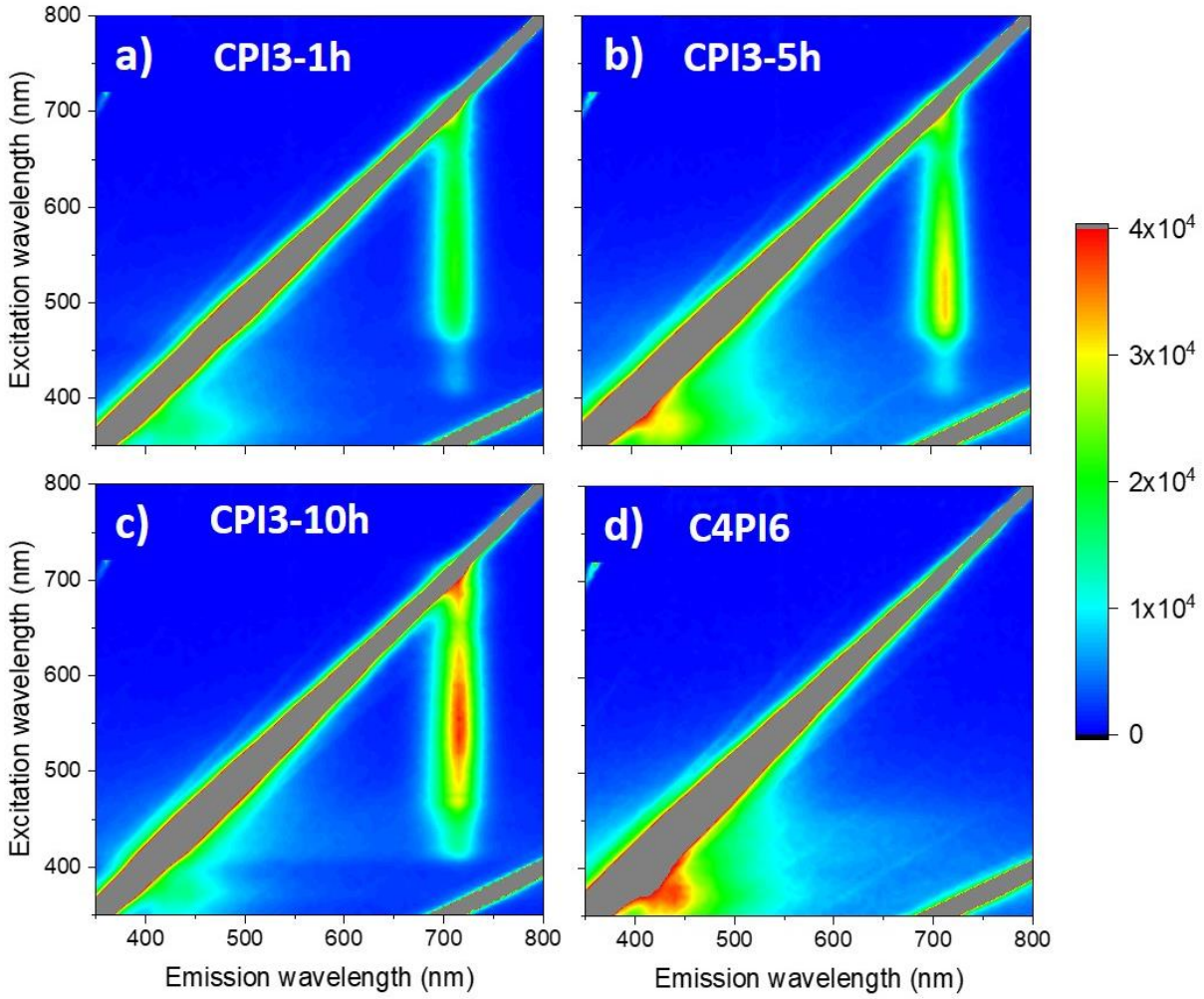

Figure 19: 3D-Photoluminescence excitation spectra of different samples: (a) CPI3-1 h, (b) CPI3-5 h, (c) CPI3-10 h and (d) C4PI6.

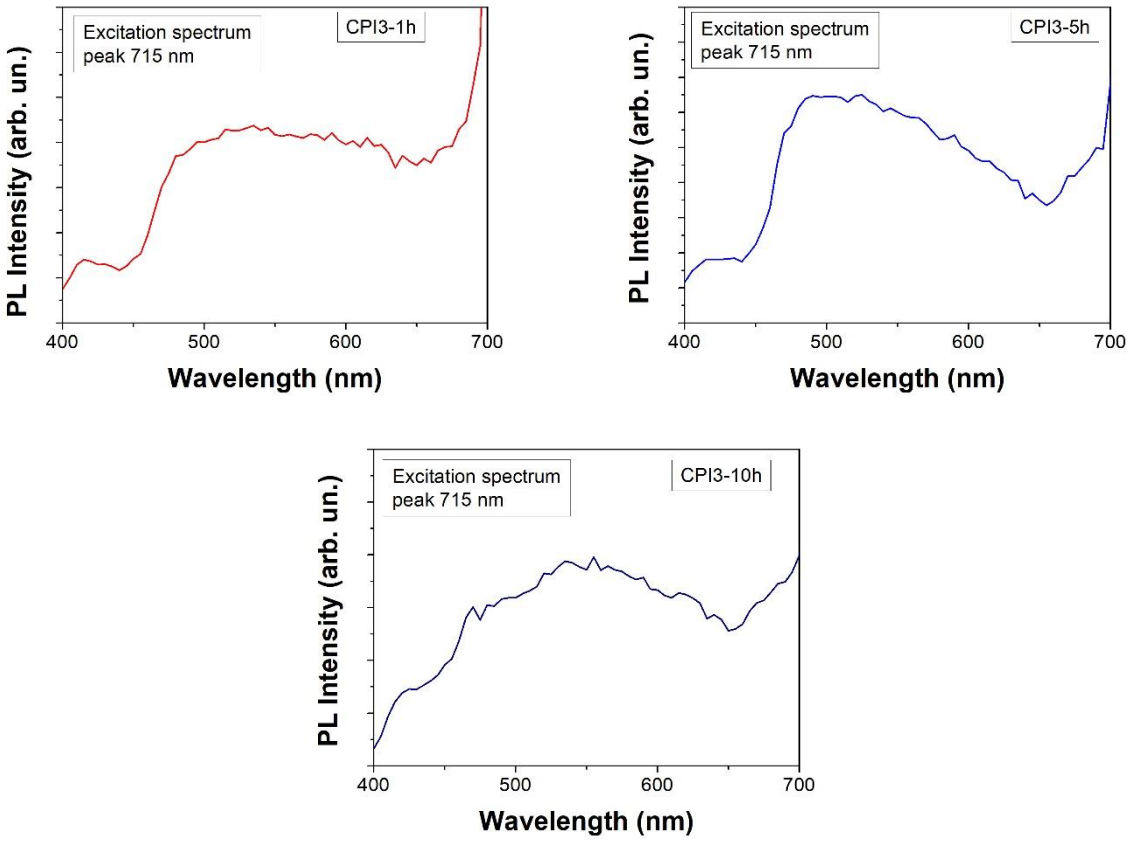

Figure 20: PL Excitation spectra of the emission at 715 nm on the samples a) CPI3-1h, b) CPI3-5h and c) CPI3-10h.

Figure 20 shows the PL Excitation spectra of the emission at 715 nm of the samples CPI3-1h, CPI3-5h and CPI3-10h. The spectra have been extrapolated from the 3D maps in Figure 19.

Time-resolved photo-luminescence measurements performed on the emission at 715 nm gave more insight into the properties of the recombination channel and consequently, on the intrinsic properties of the luminescent phase.

Figure 21 shows the results of the measurement at two different points on the sample synthesized in 10 h. The sample was not uniform, and different lifetimes for the same emission at 715 nm were observed. The curves were fitted with a multi-exponential decay function:

$$I(t) = I_0 + \sum_{i=1}^{n} A_i e^{-(t-t_0)/\tau_i}$$

with $I(t)$ time-dependent PL intensity, I_0 initial PL intensity, A_i amplitude, t time, t_0 initial time, τ_i the characteristic lifetime and $n = 2$ and $n = 3$ for points 1 and 2, respectively. Table 7 retrieves the fitting

parameters that are in accord with previous results on $CsPbI_3$ perovskite.[36,82] The average lifetime has been calculated using the following relation:[83]

$$\bar{\tau} = \frac{\sum_i A_i \cdot \tau_i^2}{\sum_i A_i \cdot \tau_i}$$

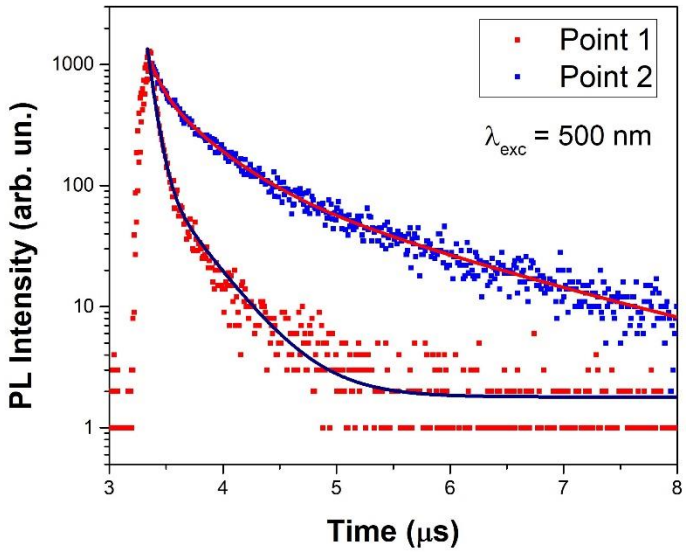

Figure 21: Time-resolved luminescence measurement at two different points of the CPI3-10 h sample; λ_{exc} = 500 nm.

Table 7: Fit parameters of TR-photoluminescence measurements.

	$\bar{\tau}$(μs)	A_1	τ_1 (μs)	A_2	τ_2 (μs)	A_3	τ_3 (μs)
Point 1	0.144	1,823.671	0.060	131.900	0.346	-	-
Point 2	0.908	448.511	0.093	497.428	0.399	136.149	1.548

Faster decay times from the same emitting centres were related to the presence of a non-radiative path:

$$\frac{1}{\tau_{obs}} = \frac{1}{\tau_R} + \frac{1}{\tau_{NR}} = \gamma_R + \gamma_{NR}$$

where τ_{obs} is the decay time experimentally measured by time-resolved luminescence analysis and τ_R and γ_R (τ_{NR} and γ_{NR}) are the decay time and transition rate for a radiative (non-radiative) process. The faster the observed decay, the higher the presence of the non-radiative path often related to structural defects.

In this case, it was possible to argue that a defective matrix non-homogeneously generated a non-radiative path for the emissions from the γ–phase of $CsPbI_3$, as could be evinced from the punctual Raman/luminescence analysis and from HRTEM images.

3.2.3 HRTEM and Epitaxy Studies

High-resolution TEM (HRTEM) structural analysis provided a direct confirmation of the features of the CPI3-10 h sample, namely the presence of nanoparticles with multiple, well-defined crystalline domains of different crystalline phases and usually surrounded by a thin, amorphous/out-of-axis shell. Two dimensional Fast Fourier Transform (2D-FFTs) diffractograms were calculated for different regions of interest (ROIs), and the corresponding planar and angular relationships between diffraction spots were analysed against diffraction cards of the phases previously identified by XRD analysis to understand the orientation of each domain. The results were compatible with the formation of crystalline domains of γ-$CsPbI_3$, δ-$CsPbI_3$ and Cs_4PbI_6, as reported in Figure 22, with lattice planes of each phase being indicated by different false colours.

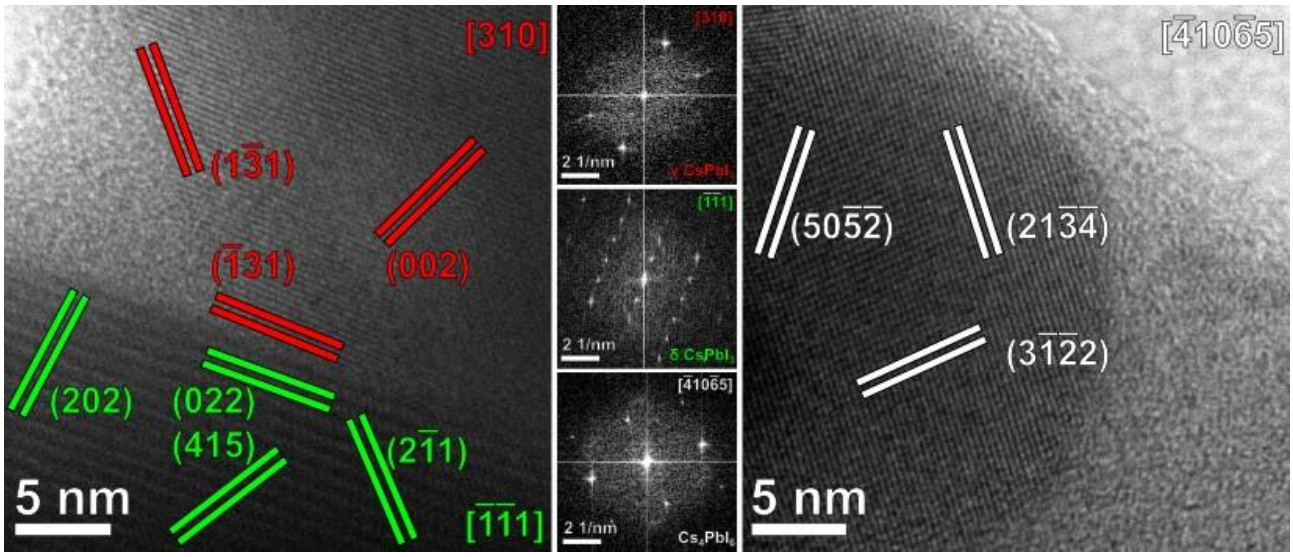

Figure 22: Representative HRTEM images of the CPI3-10 h sample. Lattice planes of γ-$CsPbI_3$, δ-$CsPbI_3$ and Cs_4PbI_6 are indicated in red, green and white, respectively. The 2D-FFT diffractograms used to calculate the orientations of each domain are reported in the central column.

Moreover, the well-defined straight interface between the γ– and δ-phases of $CsPbI_3$, reported in Figure 22, was analysed to verify the possibility of epitaxial symmetry relationships between the two phases. An interface alignment and a vector alignment were identified as follows:

$$\delta\text{-phase } (0\ 2\ 2)//\gamma\text{-phase } (-1\ 3\ 1)$$

$$\delta\text{-phase } [-1\ -1\ 1]//\gamma\text{-phase } [3\ 1\ 0]$$

These symmetry relationships were used to calculate the actual lattice mismatch (*m*) occurring between average lattice spacings of the two phases along a given direction (Table 8). In general terms, the mismatch parameter *m* between the average lattice spacings of two different phases (indicated as d_1 and d_2, respectively) can be defined as:

$$m = 2\times|d_1 - d_2|/(d_1 + d_2).$$

The Fourier analysis of the HRTEM images at the interface between two well-defined crystal domains of γ– and δ-phases was performed by 2D-fast Fourier transform (FFT) of equally-sized ROIs and proved their alignment as epitaxial, related domains: six unit cells of δ-$CsPbI_3$ (6*) along the (0 2 2) direction corresponded to eight cells of γ–$CsPbI_3$ (8*) along the (−1 3 1) direction, one unit cell of δ-$CsPbI_3$ along the (2 −1 1) direction corresponded to one cell of γ–$CsPbI_3$ along the (1 −3 1) direction and three unit cells of δ-$CsPbI_3$ (3*) along the (−1−1 1) direction corresponded to 4 cells of γ–$CsPbI_3$ (4*) along the (3 1 0) direction (see Table 8). The relevant epitaxially related lattice planes are presented in Figure 23 along with the corresponding diffraction spots in the 2D-FFTs.

*Table 8: Lattice mismatches among phases. * indicate that there are n cells in this particular crystallographic direction.*

Commensurate Lattice Mismatches *m*	
δ-phase //γ-phase	m
6 *(0 2 2)//8 *(−1 3 1)	4.0%
(2 −1 1)//(1 −3 1)	1.0%
3 *(−1 −1 1)//4 *(3 1 0)	2.0%

A slight angular distortion could be observed between the (2 −1 1) spots of δ-$CsPbI_3$ and the (1 −3 1) spots of γ–$CsPbI_3$ in comparison to their theoretical value, which could be attributed to local deformations in the crystalline frameworks in proximity to the interface.

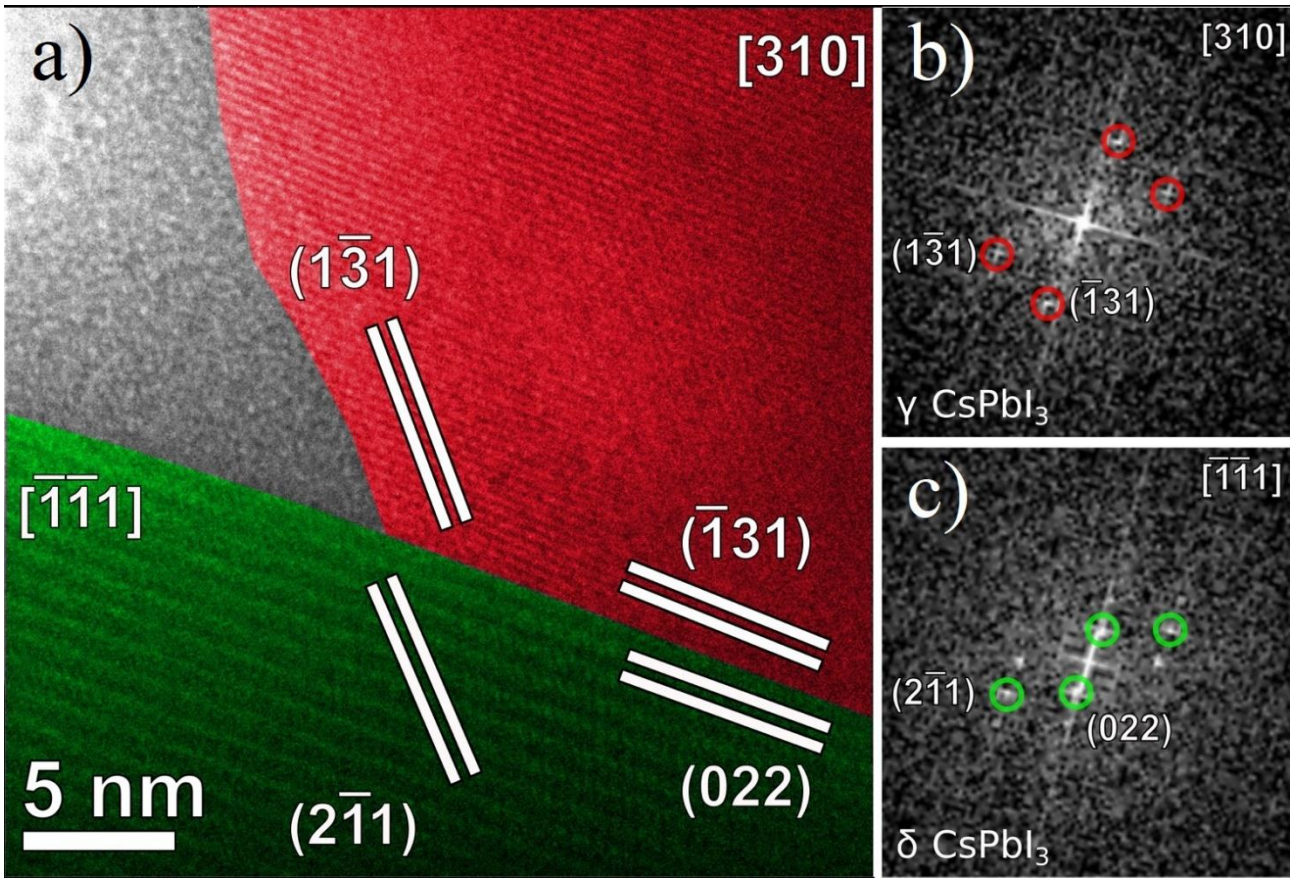

*Figure 23: **(a)** Epitaxy study on the interface between γ-$CsPbI_3$ and δ-$CsPbI_3$, previously reported in Figure 22. γ-$CsPbI_3$ and δ-$CsPbI_3$ crystal domains in the HRTEM image are depicted in red and green, respectively. **(b,c)** The diffraction spots in the 2D-FFT diffractograms corresponding to the lattice planes used for the mismatch calculations are indicated according to the same colour coding.*

A general model for phase formation in solid-state synthesis is proposed in Figure 24. In the first step, δ-$CsPbI_3$ is obtained from the precursors, CsI and PbI_2, for temperatures below 300 °C. Next, as the temperature increases, the transition between the δ and α phase occurs in a relatively fast period (observed in 10 min).

The α-phase is a cubic $CsPbI_3$ perovskite structure consisting of I ions corner-shared by two $[PbI_6]^{4-}$ octahedra, with the Cs cation occupying the 12-fold coordination site within the cuboctahedron cavities. The α-phase requires the correct stoichiometry in the perovskite structure and a high temperature (above 320 °C) to remain stable.

As time goes on, at 400 °C, the $CsPbI_3$ phase partially undergoes a dynamic equilibrium consisting of its dissociation into the starting precursors, CsI and PbI_2.

$$CsI + PbI_2 \rightleftharpoons CsPbI_3$$

PbI_2 partially evaporates, leaving behind most/all of the CsI and creating an amorphous layer around α-$CsPbI_3$. As already reported in the literature, an excess of CsI in the $CsPbI_3$ helps the formation and

the stabilization of the distorted perovskite γ phase.[84] The γ phase is orthorhombic, belonging to the Pbnm space group, and it remains stable at RT in a non-stoichiometric relationship $CsI/PbI_2 > 1$. On the other hand, the α phase converts to the δ phase at RT.[85,86]

The presence of CsI was evidenced in the XRD diffraction data reported and discussed in Figure 11. However, the higher percentage of CsI (not PbI_2) was observed in samples with prolonged thermal treatment. This data confirmed the hypothesis that there was a dynamic equilibrium between the perovskite phase and $CsI + PbI_2$.

Upon returning to RT after a variable amount of time spent at 400 °C, local variations in the CsI/PbI_2 ratio, caused by the evaporation rates of PbI_2, determine which stable phases will form in the samples. α phase crystals will form in regions with an optimal CsI/PbI_2 ratio (i.e., = 1) at a high temperature, and they will turn into δ phase at RT. Whenever the ratio is higher than 1, the creation of γ-$CsPbI_3$ is favored over α. Finally, when the CsI/PbI_2 ratio >>1, the formation of crystalline domains of secondary-phase Cs_4PbI_6 is most likely because the temporal increase of the thermal treatment generates a stronger excess of CsI, which prevents the formation of the perovskite phase and facilitates the formation of Cs_4PbI_6 (CsI/PbI_2 about 4:1).

In this sense, structural analysis performed by HRTEM showed that domains of the different phases could be observed in close proximity, which confirmed the heterogeneity in sample composition previously revealed by optical microscopy, luminescence and Raman maps. In addition, the presence of epitaxial relationships at the interface between γ and δ phase domains suggested that the structural α→δ rearranging, caused by local variations in the PbI_2 ratio, did not imply a drastic rearrangement of the atomic positions, so that a smooth structural transition between γ and δ phases could be maintained even with a sharp interface.

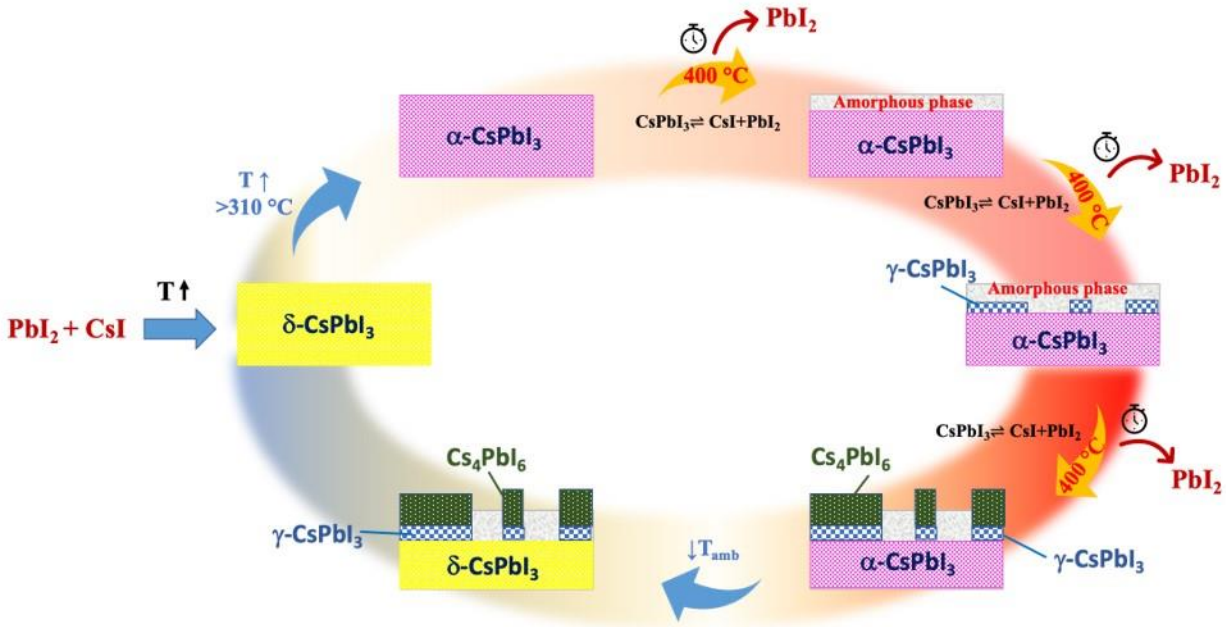

Figure 24: Model of the phase transition during the synthesis process and image of the sample after synthesis.

3.3 Conclusions

Focalized on the solid-state synthesis of pure, inorganic lead halide perovskites of the class $CsPbI_3$, we showed that a pure α phase could be obtained with a brief treatment (in the order of minutes) at 400 °C without any solvent, and that it quickly passed to a stable δ phase at room temperature. XRD analysis evidenced that an increase of treatment time at steady temperature generated the formation of the secondary phase Cs_4PbI_6, while micro-Raman and micro-luminescence measurements underlined the presence of the luminescent γ-phase. The analysis of the collected data, time resolved measurements and HRTEM imaging permitted us to understand the phase behaviour during the synthesis as a function of the temporal duration. After a few minutes at high temperature, the $CsPbI_3$ phase partially underwent a dynamic equilibrium process consisting of dissociation into its starting precursors, CsI and PbI_2. Lead iodide quickly evaporated at 400 °C, creating an excess of CsI and the consequent formation of a stable perovskite γ-phase at room temperature and, in a longer temporal step, the secondary phase Cs_4PbI_6. The samples were not uniform and presented amorphous phases and defectivity in the crystals structure, but remained stable at room temperature.

Beyond the importance of basic studies on this important class of materials, we have shown the possibility of easily obtaining bulk $CsPbI_3$, and we indicate a mechanism for future development and control of the phase formation of lead halide perovskites.

4 Caesium lead halide perovskites stabilization

Among the strategies to increase the stability of lead halide perovskites, a promising approach is to increase the contribution of the surface energy, reducing the crystal size and obtaining nanocrystals (NCs), also called Quantum dots (QDs).[32,87] Further, the high plasticity of the lattice permits the exchange of both anions and cations and, in particular, the high mobility of halide anions allows the formation of mixed-halide composition and the consequent tuning of the emission in the whole visible spectrum.[88,89] The synthetic methods are essentially divided in two categories: direct synthesis and post-synthesis. The former includes the ligand-assisted hot-injection synthesis and the ligand-assisted reprecipitation method, which have been the first approaches to synthesize $CsPbX_3$ NCs (X=Br, Cl, I).[32,41] The latter includes ion exchange,[90,91] phase transformation[92,93] and template-assisted synthesis.[94,95] Other strategies involve ultrasonication,[96,97] microwave,[87,98,99] solvothermal synthesis,[100] ball-milling[101] and chemical vapor deposition (CVD)[102]. All these approaches allow the synthesis of nanocrystals with different morphologies, from the zero dimensional nanocubes[32] and nanospheres[103] to the one dimensional nanowires[104] and the two dimensional nanoplates.[105] Despite the increased phase stability and the huge properties, critical issues of nanocrystals remains the instability under environmental stresses and the low efficiency, which need to be overcome. Among the different strategies, surface passivation seems to be a feasible and reliable approach. Different organic capping ligands have been tested to protect the NCs, preferring short-chain ligands that provide increased carrier transport.[106,107] Another strategy is to use inorganic chemicals in a post-treatment, to remove excess ions and decrease surface defects.[108–110] As well, metal ions such copper, silver and gold, have been introduced in the modification of $CsPbX_3$ NCs. They are able to substitute some Caesium atoms in the lattice structure or react with the halide forming a metal halide, able to passivate the surface and, at the same time, increase the efficiency.[111–113]

Other methodologies to improve the stability of NCs include the use of polymers and inert materials. Polymers, such as polystyrene and poly methyl methacrylate, are widely used for the encapsulation, preventing the aggregation of NCs into larger sizes and providing efficient isolation from the ambient, improving for example the water-resistance.[114,115] Inert oxide materials have been used, as well, as coating materials to protect the core of $CsPbX_3$ NCs. Alumina provides a uniform coverage of the surface and a strong barrier against water and heat.[116] The incorporation in silica matrices has been explored, both by using sol-gel method and directly mixing colloidal nanocrystals with mesoporous SiO_2.[117,118] A series of porous matrices have been tested for the nanocrystals growth. The matrix serves as host to incorporate NCs, allowing their ligand-free growth with tuneable dimensions as function of the pores size and channel orientation.[119–122] Essentially, independently of the matrix,

three methods can be employed for the infiltration of perovskites within the pores. In the aforementioned ex-situ process, the suspension of colloidal nanocrystals is infiltrated in the matrix and the size is predetermined by the synthesis parameters. Other two approaches are in-situ methods: the first is a two-step method, where the metal halide is infiltrated in the matrix and then the scaffold is immersed in the solution containing the cation; the second is a single step method, where the matrix is impregnated with an unreacted solution of perovskite precursors. In both the two approaches, the reaction occurs within the pores when the solvent evaporates after annealing.

In this perspective, during the Ph.D. course, two works dedicated to the role of the interaction of perovskites with surrounding matrix have been performed. In the first, the possibility of realizing a heterostructure of $CsPbBr_3$ NCs and nanoporous gold has been studied. The aim was to study the interaction between halide perovskites and a nanoporous metal matrix, evaluating the stability of metal – perovskite interface, by analysing the variation of the optical properties. Indeed, of paramount importance is the interaction between the perovskite and the metals for the stability of devices architecture, where the metals constitute back-contacts.[123] We show two different synthesis approaches to obtain the heterostructure, but as it will be reported in the following chapter, the efficient charge transfer process in NCs@NP Au has been observed only when perovskites NCs were grown directly in the proximity of the gold surface.

The second study was focalized on NCs@Silica heterostructure. In this case the surrounding matrix had the role of protecting NCs perovskite and no charge transfer process are expected and established. Likely to the previous approach, the synthesis of the perovskite structure has been obtained directly in ordered mesoporous matrices (SBA-15 and MCM 41, mean pore diameter 8 and 4 nm, respectively), but in this case the nanosized dimension is defined by the morphology of the matrix itself. The post heat treatment at high temperature assures the collapse of the silica structure and the realization of a robust protective shell on the perovskite.

$CsPbCl_3$, $CsPbBr_3$ and $CsPbI_3$ NCs have been obtained with different optical and emitting properties that permitted us to obtain a first prototype of RGB matrix for lighting applications.

5 Energy Transfer Mechanism in $CsPbBr_3$ – Au Nanostructure

Jessica Satta, Andrea Pinna, Giorgio Pia, Luca Pilia, Carlo Maria Carbonaro, Daniele Chiriu, Luigi Stagi, Pier Carlo Ricci

Submitted to pssa: physica status solidi (a) – Special issue E-MRS Spring Meeting symposium S

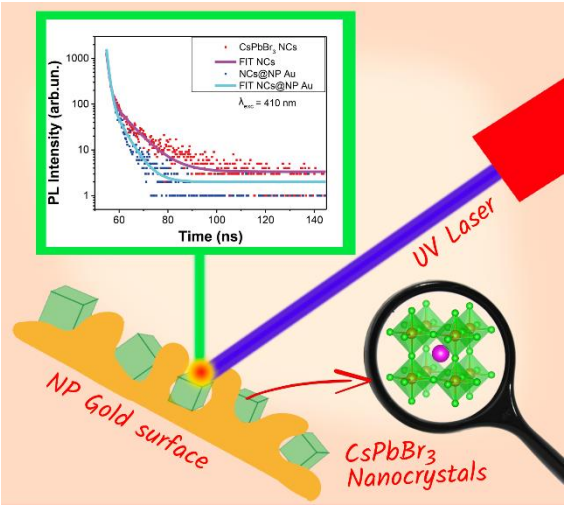

Despite all their promising characteristics, the efficiency of QDs devices is far from the theoretically predicted values, probably due to poor charge transfer at the interfaces.[124,125] Further, the poor stability hampers commercial applications of the devices, being them sensitive to heat, light and environmental stresses.[75,85,126,127] In photocatalysis and photovoltaics, for example, the performances of the devices depend on their charge separation ability and the implementation of good NCs – electrode interfaces. The development of nanocrystals – metal heterostructures can help to improve both factors and provide new functionalities to the nanostructures, altering the optical properties of semiconductors, notably with photoluminescence quenching or enhancement.[128–130] Noble metals are widely used for their intrinsic capacity to accept electrons, fast capturing the photogenerated electrons at the semiconductor surface, promoting the charge separation and the reduction processes. The presence of metal is also known to induce plasmonic field effects in semiconductor nanostructures, influencing their photocatalytic and photovoltaic performances.[131,132] Among several geometries, plasmonic nanocavities can confine electromagnetic fields in ultrasmall volumes, resulting in very big local field enhancement. Nanoporous metals are self–standing metallic materials with interconnected nano – sized ligaments and pores, commonly obtained by dealloying of a precursor alloy.[133] Among them, nanoporous gold (hereafter, NP Au) is the most studied material. NP Au finds possible applications in various technological areas,[133] such as catalysis,[134] sensing,[135] Surface – Enhanced Raman Spectroscopy (SERS),[136] Metal – Enhanced Fluorescence

(MEF),[137] actuators,[138] energy storage and conversion.[139] Several works have been focused on studying the optical properties of lead halide perovskites – Au nanocomposites and their application in photocatalysis and photovoltaic.[140–142]

In this chapter, we explore the possibility to develop a $CsPbBr_3$ – NP Au heterostructure (hereafter NCs@NP Au). Indeed, two different approaches were developed and studied to obtain the NCs – Au system, and the optical and structural properties are reported. By analyzing the effect on $CsPbBr_3$ optical properties influenced by the presence of gold, we evidence the efficient charge transfer process in NCs@NP Au investigating the possible formation mechanisms of the heterostructure.

5.1 Experimental section and methods

5.1.1 Chemicals

Caesium carbonate (Cs_2CO_3; Aldrich, CAS No. 534-17-8), Octanoic acid (OTAc; Aldrich, CAS No. 124-07-2), Lead bromide ($PbBr_2$; Aldrich, CAS No. 10031-22-8), Tetraoctylammonium bromide (TOAB; Aldrich, CASNo. 14866-33-2), Didodecyldimethylammonium bromide (DDAB; Aldrich, CAS No. 3282-73-3). Toluene, Ethyl acetate, and n-Hexane were of analytical grade. Au powders (99.995%, Alfa Aesar, CAS No. 7440-57-5), Ag powders (99.9%, Aldrich, CAS No. 7440-22-4), Nitric acid (HNO_3 70%, BDH, CAS No. 7697-37-2). Ultrapure water (18.2 MΩ·cm) was produced with a Milli-Q Millipore water purification system. All chemicals were used without any further purification.

5.1.2 Synthesis and purification of $CsPbBr_3$ NCs

Synthesis and purification of $CsPbBr_3$ NCs were performed based on previous records.[143] First, caesium precursor was prepared by loading 1 mmol of Cs_2CO_3 and 10 mL of OTAc into a 20 mL vial, and the mixture was stirred for 10 min at room temperature. The $PbBr_2$ precursor solution was prepared by dissolving 1 mmol of $PbBr_2$ and 2 mmol of TOAB in 10 mL of toluene. For the synthesis of $CsPbBr_3$ QDs, 1.0 mL of caesium precursor solution was swiftly added into 9 mL of a $PbBr_2$–toluene solution into the conical flask. The reaction was magnetically stirred for 5 min at room temperature in open air. Subsequently, 3 mL of DDAB (in toluene 10 mg mL^{-1}) solution was added. After 2 min, ethyl acetate was added into the crude solution with a volume ratio of 2:1; the precipitate was collected separately after centrifugation and dispersed in toluene. The extra ethyl acetate was added into the toluene dispersion, and the precipitate was collected and re-dispersed in n-hexane.

5.1.3 Synthesis of NP Au

Precursor alloy fabrication

Au and Ag powders were mixed in a ratio 30:70. 2g of the mixture were ball milled in a SPEX 8000M Mixer/Mill ball mill for 16 hours in a hardened steel vial with two hardened steel spheres of 8g each. The powders were homogenized every 30 minutes in the first 2 hours and then every 5 hours.

NP Au fabrication

NP Au powders were prepared by chemical dealloying in HNO_3 70% for 24 hours.[144,145] The powders were then washed in MillQ water 5 times and then dried under vacuum.

5.1.4 Synthesis and purification of $CsPbBr_3$–Au hybrid structure

$CsPbBr_3$ – Au hybrid structures have been prepared following two different procedures.

In procedure 1, 70 mg of NP Au were just added into the $CsPbBr_3$ NCs (2mg/mL) dispersed in hexane (3 ml) under ambient conditions. After stirring for 4 hours, the powder was filtered and washed several times with hexane under vacuum and then dried overnight.

In procedure 2, the synthesis of $CsPbBr_3$ QDs was repeated in presence of NP Au. NP Au (140 mg) was added to the $PbBr_2$ precursor solution, then the synthesis proceeded identically. The hexane dispersion was filtered and washed several times with hexane under vacuum, to separate the nanocrystals not linked to gold, and then dried overnight.

5.1.5 Characterization

X-ray measurements were performed with a Bruker D8 Advance diffractometer operating at 30 kV and 20 mA, equipped with a Cu tube (λ = 1.5418 Å) and a Vantec-1 PSD detector. The powder patterns were recorded in the $10° \leq 2\theta \leq 70°$ range.

Raman measurements were collected using MS750 spectrograph (sol-instruments) equipped with 600 gr/mm grating. The laser beam (785 nm) was focalized through an Olympus objective (10x), with a laser power of about 7.5 mW. Measurements were performed at room temperature, with a spectral resolution of 1 cm^{-1}.

The absorption measurements were obtained by diffuse reflectance spectroscopy utilizing a UV-Vis-NIR Agilent Technologies Cary 5000. Measurements were performed by using a PbS solid state photodetector using KBr as reference. The reflection configuration measures the diffuse reflection of sample respect to a reference sample which is considered to have a 100% reflectivity. The Kubelka-Munk equation was applied to define the absorption properties.

Time-resolved photoluminescence (TR-PL) measurements were recorded by exciting the samples with 200 fs pulses sourced from an optical parametric amplifier (Light Conversion TOPAS-C) pumped by a regenerative Ti:Sapphire amplifier (Coherent Libra-HE). The repetition frequency was 1 kHz and the TR-PL signal was recorded by a streak camera (Hamamatsu C10910) equipped with a grating spectrometer (Princeton Instruments Acton Spectra Pro SP-2300). All the measurements were collected in the front-face configuration to reduce inner filter effects. Proper emission filters were applied to remove the reflected contribution of the excitation light.

Scanning Electron Microscopy (SEM) for nanoporous gold was performed with a FEI Quanta Field Emission Electron Microscope, equipped with an Everhart-Thornley secondary electron detector. Imaging was performed at an operating voltage of 20 kV at 10 mm from the examined samples.

SEM studies for heterostructures were carried out using a Carl ZEISS Auriga microscope equipped with an energy dispersive X-ray spectroscopy (EDX) detector or an ESEM FEI Quanta 200 microscope operating at 25 kV.

Transmission Electron Microscopy measurements on pure $CsPbBr_3$ NCs were performed using a Jeol JEM 1400 plus at 120 kV.

5.2 Results and discussion

SEM image of the as-prepared NP Au is shown in Figure 25. NP Au shows a fine nanoporous structure with ligaments and pores diameters around 20 nm.

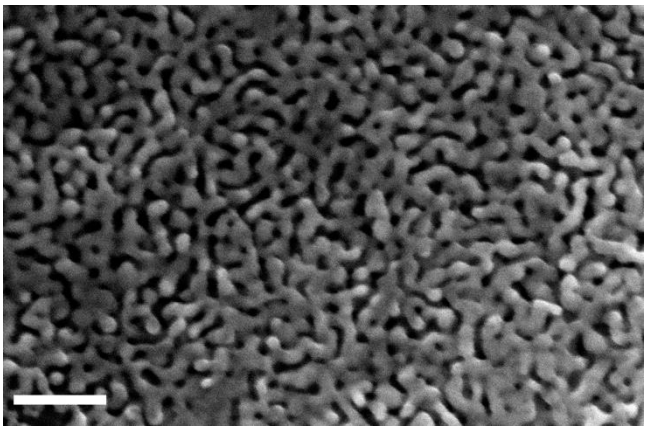

Figure 25: SEM image of NP Au, scale bar: 200 nm.

$CsPbBr_3$ nanocrystals were synthesized following a room–temperature procedure, adopted in previous reports with QDs crystal size of about 10 nm, with a uniform and cubic morphology (Figure 26).[143]

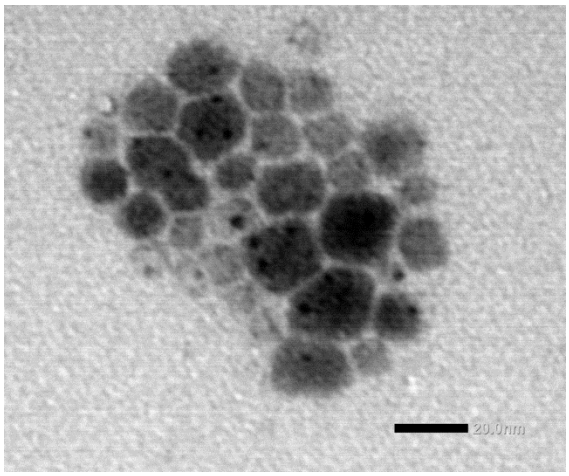

Figure 26: TEM image of $CsPbBr_3$ NCs, scale bar 20 nm.

X-ray diffraction measurements were performed on nanocrystals precipitate. Figure 27 reports the Rietveld refinement of the pattern, obtained by using the software MAUD.[76] $CsPbBr_3$ NCs are in the orthorhombic γ-phase (Pbnm, space group No. 62, COD ID 1533062), with lattice parameters a = 8.219 Å, b = 8.254 Å and c = 11.753 Å.

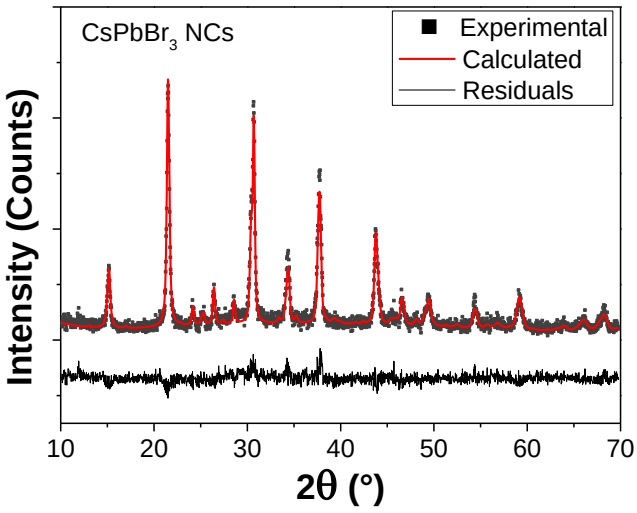

Figure 27: Rietveld refinement of the nanocrystals precipitate. ■ refers to the Experimental pattern, Red line is the pattern calculated by Rietveld refinement, in Black line the residuals between the experimental and calculated pattern.

In Figure 28 the Raman spectrum of the nanocrystals precipitate is reported; in the inset the enlarged view of the region 200 – 400 cm^{-1}. The Raman features confirm that $CsPbBr_3$ NCs are in the orthorhombic γ-phase, with an intense peak in the region 60 – 80 cm^{-1}, a low-intensity peak around 130 cm^{-1}, and a broad second-order peak around 310 cm^{-1}.[146,147]

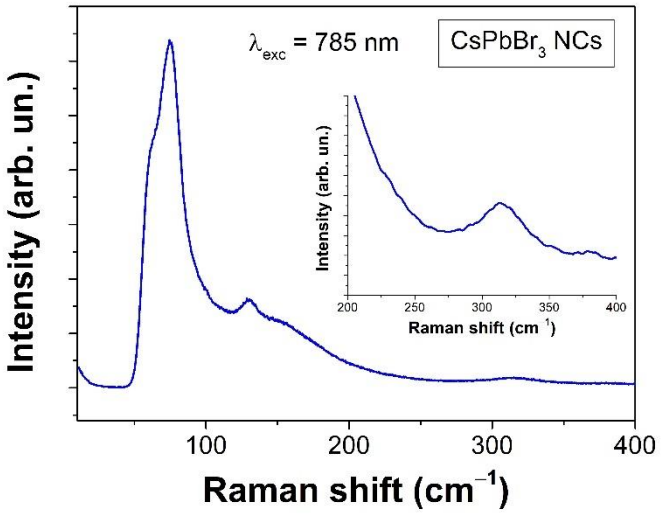

Figure 28: Raman spectrum of nanocrystals precipitate; in the inset a zoom of the region 200 – 400 cm^{-1}. λ_{exc} = 785 nm.

Figure 29 presents the absorption and emission spectra of colloidal $CsPbBr_3$ dispersed in hexane. The NCs show bright photoluminescence with an emission maximum at 518 nm.

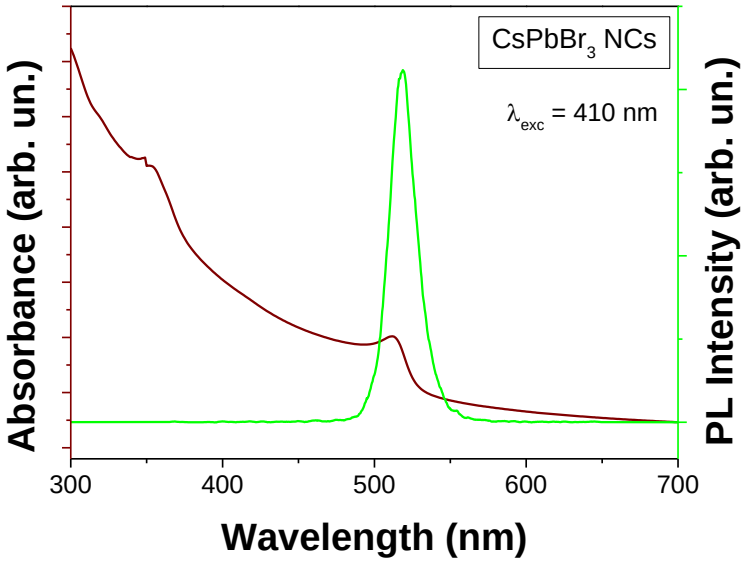

Figure 29: Absorption (brown) and emission (green) spectra of colloidal $CsPbBr_3$ NCs; λ_{exc} = 410 nm.

The synthesis of NCs@NP Au followed two different procedures (detailed conditions are reported in 5.1.4). In procedure 1, a known amount of NP Au (70 mg) was incorporated into the hexane suspension of $CsPbBr_3$ NCs under ambient conditions. The concentration of the $CsPbBr_3$ NCs was 2mg/mL. Figure 30 shows the pictures of the solution under UV light (375 nm), before and after the addition of NP Au.

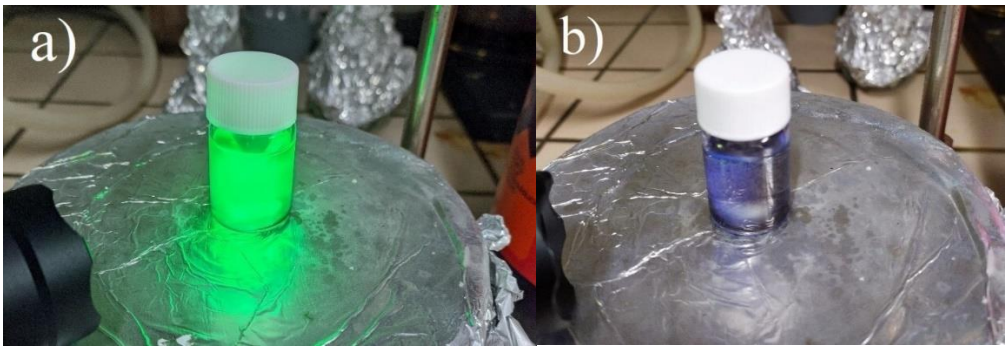

Figure 30: Photographs under UV light (375 nm) of $CsPbBr_3$ NCs dispersion a) before and b) after the introduction of nanoporous gold.

The solution turns to be colourless with a drastic quenching of the fluorescence. Raman measurements (Figure 31) show the presence of two peaks (135 and 176 cm^{-1}), which cannot be assigned but are in the range of Cs – Pb – Br vibrations.[146,148,149] This can be attributed to the instability of NCs in presence of gold.

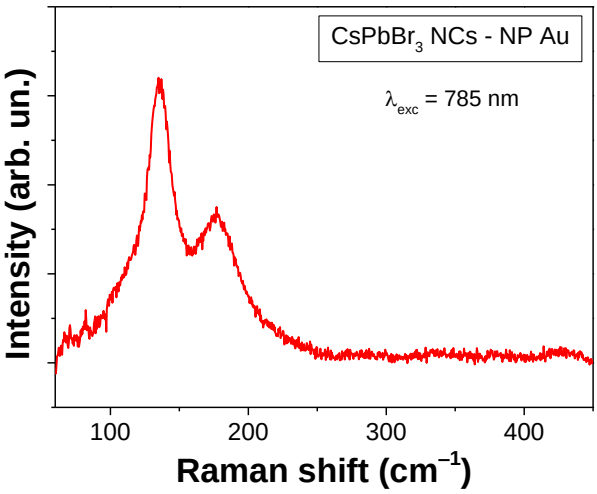

Figure 31: Raman spectrum of NP Au soaked with $CsPbBr_3$ NCs.

The capping agent (namely, DDAB) is formed by the alkyl chain terminating with the Nitrogen and methyl groups, respectively. It is widely accepted the strong affinity of the Au surface with ammonium surfactants, and the capping agent likely leaves the nanoparticles to deposit on the Au nanostructures.[150–152]

We argue that NP Au possess a good affinity with the capping agent of $CsPbBr_3$ NCs. Stripped of all protection, NCs are no longer stable in hexane and degrade in different stoichiometric phases, as observed in the Raman spectra. To further confirm the hypothesis, the Au nanostructures were covered with the same capping agent and successively added to the $CsPbBr_3$ NCs hexane solution.

No interaction between $CsPbBr_3$ NCs and Au nanostructures was observed in this case, the perovskites maintain the structural stability and their characteristic optical properties.

In order to further confirm the hypotesis of the degradation, we performed the elemental analysis on different points of the surface of the sample obtained with procedure 1, by means of SEM – EDX measurements. Paying attention to Cs, Pb and Br, we evidenced the presence of lead or caesium, or both of them, with the disappearence of bromine. This difference in the stoichiometry from the starting $CsPbBr_3$ NCs confirms the absence of perovskites and the formation of amorphous Cs – Pb compounds.

In procedure 2, nanoporous gold was added during the synthesis of $CsPbBr_3$ nanocrystals, then the synthesis proceeded as mentioned in 5.1.2. Figure 32 reports the XRD pattern of the as synthesized sample, compared to pure NP Au. It's possible to notice the presence of additional peaks (at 21.5°, 31.5°, 49.4° and 59.1°), pertaining to pure $CsPbBr_3$ NCs (Rietveld refinement in Figure 27).

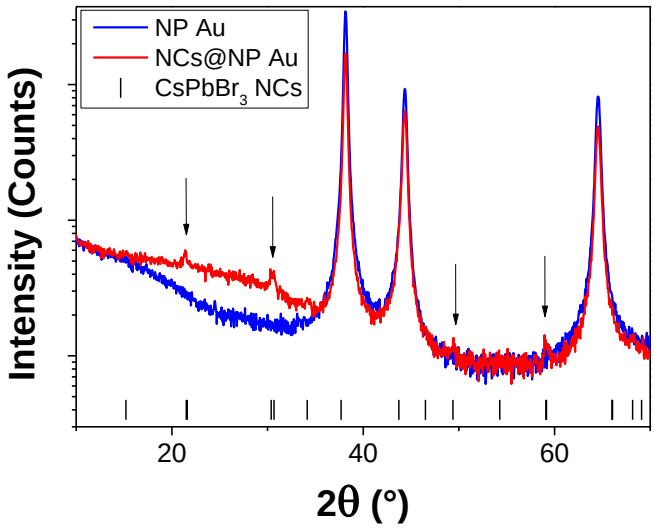

Figure 32: XRD pattern of the sample of pure NP Au (blue) and NCs@NP Au heterostructure (red). Vertical bar individuates the main peaks of pure $CsPbBr_3$ NCs.

Figure 33 shows the steady-state luminescence spectrum of NCs@NP Au heterostructure compared to the emission of the pure $CsPbBr_3$ NCs.

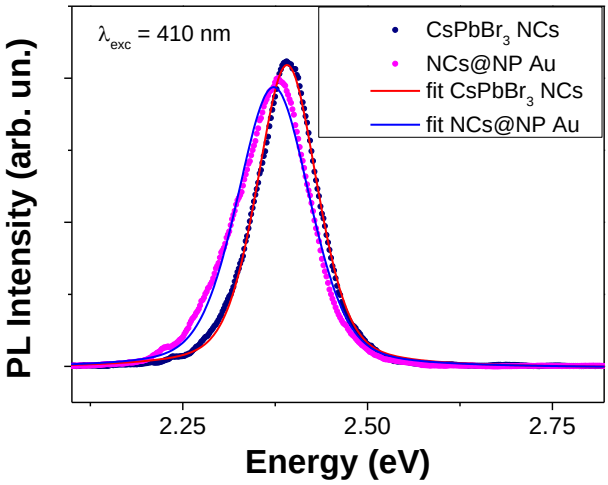

Figure 33: Steady-state luminescence spectra of pure $CsPbBr_3$ NCs and NCs – Au hybrid structure; λ_{exc} = 410 nm.

The curves have been fitted with a Pseudo-Voigt function, a combination of Gaussian and Lorentzian profiles:

$$I = I_0 + A\left[\mu\frac{2}{\pi}\frac{w_L}{4(x-x_c)^2+w_L^2} + (1-\mu)\frac{\sqrt{4\ln(2)}}{\sqrt{\pi}w_G}e^{-\frac{4\ln(2)}{w_G^2}(x-x_c)^2}\right]$$

where m represents the Lorentzian character of the Voigt profile, w_L and w_G are the width parameters of the Lorentzian and Gaussian components, respectively. A slight red shift and a small line broadening is observed. Derived parameters are reported in Table 9.

Table 9: Fit parameters of PL measurements on pure $CsPbBr_3$ NCs and NCs – Au hybrid structure.

	x_c [eV]	**w [eV]**	**μ**
$CsPbBr_3$ NCs	2.39	0.097	0.48
NCs@NP Au	2.37	0.117	0.41

Time-resolved photoluminescence measurements (reported in Figure 34) performed on the samples give more insight on the properties of the recombination mechanism. The curves have been fitted with a biexponential decay function:

$$I(t) = I_0 + \sum_{i=1}^{2} A_i e^{-(t-t_0)/\tau_i}$$

With I(t) time-dependent PL intensity, I_0 initial PL intensity, A_i amplitude, t time, t_0 initial time, t_i the characteristic lifetime. Table 10 retrieves the fitting parameters, which are in accord with previous results.[143,153,154] The average lifetime has been calculated using the following relation:[83]

$$\bar{\tau} = \frac{\sum_i A_i \cdot \tau_i^2}{\sum_i A_i \cdot \tau_i}$$

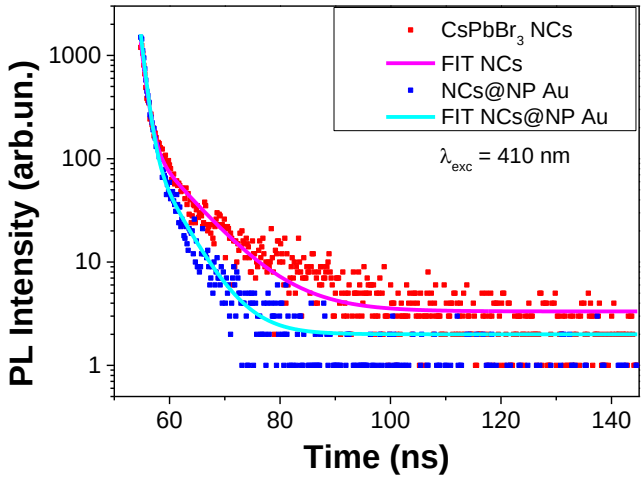

Figure 34: Time-resolved photoluminescence measurement on pure $CsPbBr_3$ NCs and NCs – Au hybrid structure; λ_{exc} = 410 nm.

Table 10: Fit parameters of TR – photoluminescence measurements.

	$\bar{\tau}$ [ns]	A_1	τ_1 [ns]	A_2	τ_2 [ns]
$CsPbBr_3$ NCs	**3.6**	1445.2	0.89	144.02	7.0
NCs@NP Au	**1.9**	1760.9	0.87	140.7	4.4

The average lifetime decreases from 3.6 ns to 1.9 ns, showing the interaction between $CsPbBr_3$ NCs and nanoporous gold matrix evidenced by the shortening of the average lifetime with respect to the pure $CsPbBr_3$ NCs. Indeed, it strongly suggests the presence of non-radiative recombination path and

the formation of NCs – NP Au hybrid structure. The transfer efficiency can be calculated by the relation:

$$\eta = 1 - \frac{\tau}{\tau_0}$$

Where τ_0 is the average lifetime in pure $CsPbBr_3$ NCs and τ the average lifetime in presence of gold. The calculated charge transfer efficiency is around 47%.

5.3 Conclusions

Summarizing, the goal was to realize a $CsPbBr_3$ – Au heterostructure. By one approach, $CsPbBr_3$ NCs dispersed in hexane were mixed with nanoporous gold. The result is the disappearance of the luminescence, whose cause is assumed to be the degradation of NCs and the subsequent formation of amorphous compounds. The second approach involves the synthesis of NCs directly on NP Au surface. In this case, it's possible to notice a blue shift in the emission spectrum and a faster decay. Such behaviour can be attributed to the achievement of a nanostructure of $CsPbBr_3$ NCs and NP Au, with an efficient charge transfer. The result show high potential appliance in all the applications where an efficient charge transfer is required. Further, the possibility to utilize the perovskite NCs as efficient sensitizer strongly suggest the possibility to achieve tunable photocatalityc device active in all the visible range. In this regards, further specific measurements needs to be performed.

6 Caesium lead halides perovskites in silica matrices: a step toward the stability

The definition of Quantum dots (QDs) first entered the lexicon of materials related to spatial quantization of fabricated heterojunction systems based on gallium—arsenic (GaAs) compounds in 1986.[155] The paper gave a fundamental insight into the unique electronic subsystem of crystal heterostructures, defining QDs as promising materials for the next future. However, from their first appearance, QDs are always related to compounds with inherent toxicity. If in their first version was the arsenic, currently, the best-known quantum dot technologies is based on materials that benefit from controversial Restriction of Hazardous Substances (RoHS) exemptions. Despite the classification of cadmium as a carcinogenic heavy metal, Cadmium selenide (CdSe) is widely utilized in QDs, being one of the leading compound for quantum dot synthesis.[156] The exemption for cadmium in display applications was initially established due to the technological importance of cadmium–based quantum dots and the lack of a suitable alternative. Other compounds did exist, but they were neither commercially viable nor comparable in terms of efficiency and performance.[157,158] Permissible limits of cadmium concentration were set at 100 parts per million (ppm) by weight, but initially, this limit had been exempted to 1000 ppm.

With the onset of new, high-performance quantum dot technologies, the exemption established for cadmium appears more fragile than ever before. In 2015 the European Commission defined new restrictions where the maximum permitted concentrations in non-exempt products are 0.01% or 100 ppm by weight.[159] The restrictions are on each homogeneous material in the product, which means that the limits do not apply to the weight of the finished product, or even to a component, but to any single material that could (theoretically) be separated mechanically — for example, display. Further, although arguments continually suggest that the current RoHS limitation for cadmium is safe for commercial display applications, the potential toxicity of cadmium in biological environments remains an area of concern, which is why the development of cadmium-free quantum dots is therefore mandatory.

Caesium lead halide perovskites were the first quantum dot technology to spearhead cadmium-free innovations, conform to long-established RoHS regulations for lead concentration in displays, being less than 1000 ppm, meeting RoHS limitations for restricted substances.

Now, a plethora of novel chemical arrangements has arrived with realistic, industrial-scale applicability. The initial drawback of alternative technologies was their comparatively poor

performance and low stability respect to cadmium-based quantum dots, but now Cadmium-free quantum dots with high photoluminescent quantum yields (PLQY >86%) have been already achieved.[160,161] The challenges to overcome the hegemonic position of cadmium- and indium-based products as the only materials capable of reaching the high-performance quantum dot technology need to be pursuit.

Inorganic lead halide perovskites NCs possess several properties which make them suitable for full-colour displays, including quantum confinement, narrow emission spectrum, high quantum yield, low manufacturing costs, and in particular a large colour gamut.[162,163] However, they show poor stability under operation conditions, in particular red-emitting iodine-based $CsPbX_3$ NCs. Several works have proposed different methods to enhance NCs stability, promoting encapsulation, which provides a protective shell against external factors.[115,163,164]

In this perspective, in this chapter, we report a viable way to enhance the stability of inorganic lead halide perovskites utilizing encapsulation in mesoporous silica matrices. Starting from Zhang's work,[164] we study the encapsulation of $CsPbX_3$ in SBA-15 and MCM-41 mesoporous silica. The mesostructured silica acts as a template for the formation of nanosized perovskites. The nanometric dimensions contribute to the structural stability of metal halide perovskites, but this is not enough to ensure good stability against moisture, oxygen and water. Hence the need to create a protective shell, which can be obtained by collapsing the silica to incorporate the nanocrystals. As the final goal, a first prototype of a RGB matrix backlight with a NUV source is realized.

6.1 Experimental section

6.1.1 Materials

Caesium iodide (CsI, 50 ppm alkali metals, 99,9%) was purchased from Alfa Aesar, Caesium bromide (CsBr, 99.9% trace metals basis), caesium chloride (CsCl, 99.9%), lead bromide ($PbBr_2$, ≥98%), lead iodide (PbI_2, 99%), lead chloride ($PbCl_2$, 98%), mesoporous silica SBA-15 (SiO_2, <150 μm particle size, pore size 8 nm, Hexagonal pore morphology), mesoporous silica MCM-41 (SiO_2, pore size 3.6 nm, Hexagonal pore morphology) were purchased from Sigma Aldrich. All chemicals were used without any further purification.

6.1.2 Synthesis

$CsPbX_3$ (X=Cl, Br, I) in MCM-41 and in SBA-15 have been synthesized, following the same procedure, but varying the annealing temperature. CsX and PbX_2 (X=Cl, Br, I, molar ratio 1:1) were dissolved in ultrapure water and stirred constantly for 30 min at 80 °C. The concentration was 0.012 M in the case of bromides and chlorides. Since PbI_2 is poorly soluble in water, the concentration

was decreased to 0.003 M for iodides. Then, a certain amount of microporous silica (MS) was added to the above solution (CsX/PbX_2:MS = 1:1) and the mixture was stirred for 1 h at 80 °C. The as-obtained mixture was dried at 80 °C, then ground and calcined for 0.5 h with a heating rate of 5 °C min^{-1}, at 600 °C in the case of MCM-41 and 800 °C for SBA-15 (Figure 35). Finally, the samples were washed with distilled water and then dried in vacuum at 60 °C.

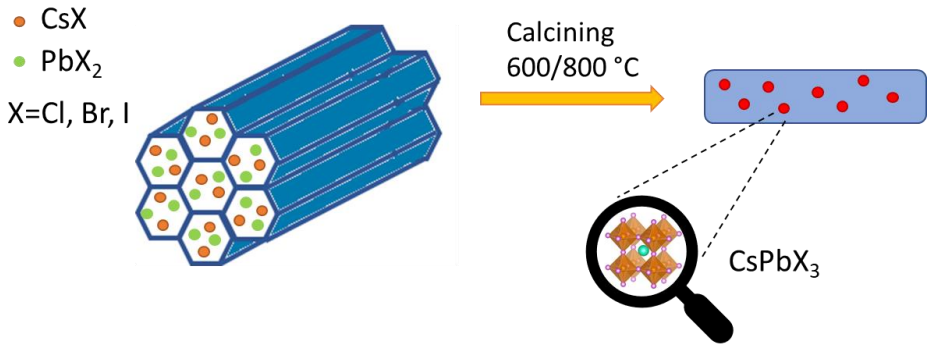

Figure 35: Scheme of the synthetic procedure.

6.1.3 Device fabrication

A 3x3 matrix has been realized perforating a slab of plexiglass with a black back surface. Each hole has been filled with a different perovskite sample, forming three lines in alternating colours (green, blue and red). To obtain a homogeneous layer to fill the holes, the powders of $CsPbX_3$@MS have been mixed with a transparent resin CMIT/MIT (weight ratio powder/resin = 1/2). The powder has been mixed with resin, instead of creating a pellet of just perovskite/silica, to reduce the amount of sample avoiding an excessive thickness which limit the transmission of the excitation source.

6.1.4 Characterization

Transmission Electron Microscopy measurements were performed using a Jeol JEM 1400 plus at 120 kV.

N_2 physisorption characterization was performed using a Micrometrics ASAP 2020 Porosimeter at 77 K. Surface area and pore volume textural parameters were assessed by the Brunauer-Emmett-Teller and Barret-Joyner-Halenda methods, respectively.

X-ray patterns were collected by using a Bruker D8 Advance diffractometer operating at 30 kV and 20 mA, equipped with a Cu tube (λ = 1.5418 Å), a Vantec-1 PSD detector. The powder patterns were recorded in the $10° \leq 2\theta \leq 60°$ range.

The absorption measurements were obtained by diffuse reflectance spectroscopy utilizing a UV-Vis-NIR Agilent Technologies Cary 5000. Measurements were performed by using a PbS solid-state photodetector using KBr as reference. The reflection configuration measures the diffuse reflection of

the sample with respect to a reference sample which is considered to have a 100% reflectivity. The Kubelka-Munk equation was applied to define the absorption properties.

Time-resolved photoluminescence (TR-PL) measurements were recorded by exciting the samples with 200 fs pulses sourced from an optical parametric amplifier (Light Conversion TOPAS-C) pumped by a regenerative Ti:Sapphire amplifier (Coherent Libra-HE). The repetition frequency was 1 kHz and the TR-PL signal was recorded by a streak camera (Hamamatsu C10910) equipped with a grating spectrometer (Princeton Instruments Acton Spectra Pro SP-2300). All the measurements were collected in the front-face configuration to reduce inner filter effects. Proper emission filters were applied to remove the reflected contribution of the excitation light.

6.2 Results and discussion

6.2.1 Structural and morphological characterizations

The first key point that is needed to be addressed is the definition of the morphological and structural aspects of the Perovskite/Silica compounds. However, even if crucial, the characterization techniques suffer from the shielding effect of the Silica matrix.

The TEM analysis of the starting mesoporous structure shows an ordered path with dimensions well defined in the order of ten nanometres (Figure 36). After the treatment in aqueous solution with the precursors of the final perovskites, nanometric inclusions of perovskite nanoparticles in the Silica mesh are clearly observable.

Crystals non-uniformly distributed but arranged along the direction of the channels can be observed, suggesting an effective infiltration of the precursors solution during the synthesis. The agglomeration of the different particles does not permit a deep analysis, but a non-complete filling of the pores is observed.

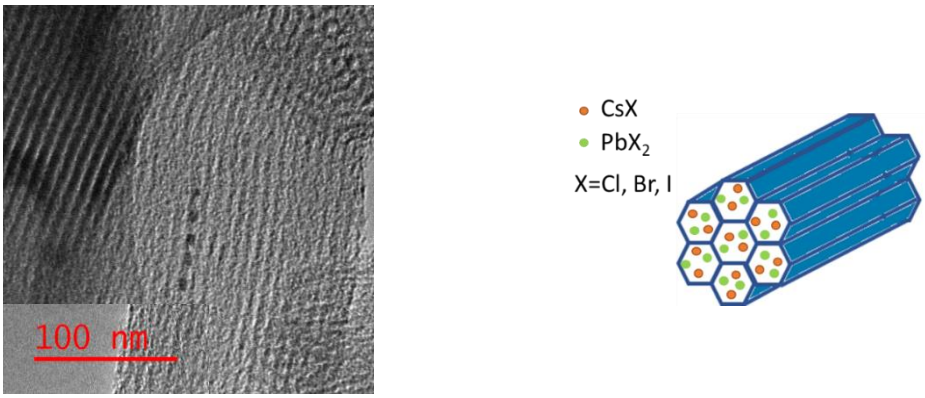

Figure 36: TEM image of $CsPbI_3$@SBA-15 before the thermal treatment and graphical representation.

The BET analysis (Figure 37) on the impregnated samples shows a drastic reduction of the available specific surface, confirming the partial filling of the pores and the collapsing of the Silica structure after the thermal treatment for all three samples. The average surface area passes from 646 m^2/g and

pore volume of 0.87 cm^3/g in the pristine samples to 348 m^2/g and 0.55 cm^3/g, respectively, for the impregnated samples, before the thermal treatment. The collapse of the porous structure, after calcination, is well evidenced by the decreased surface area for the thermally treated samples, down to 54 m^2/g.

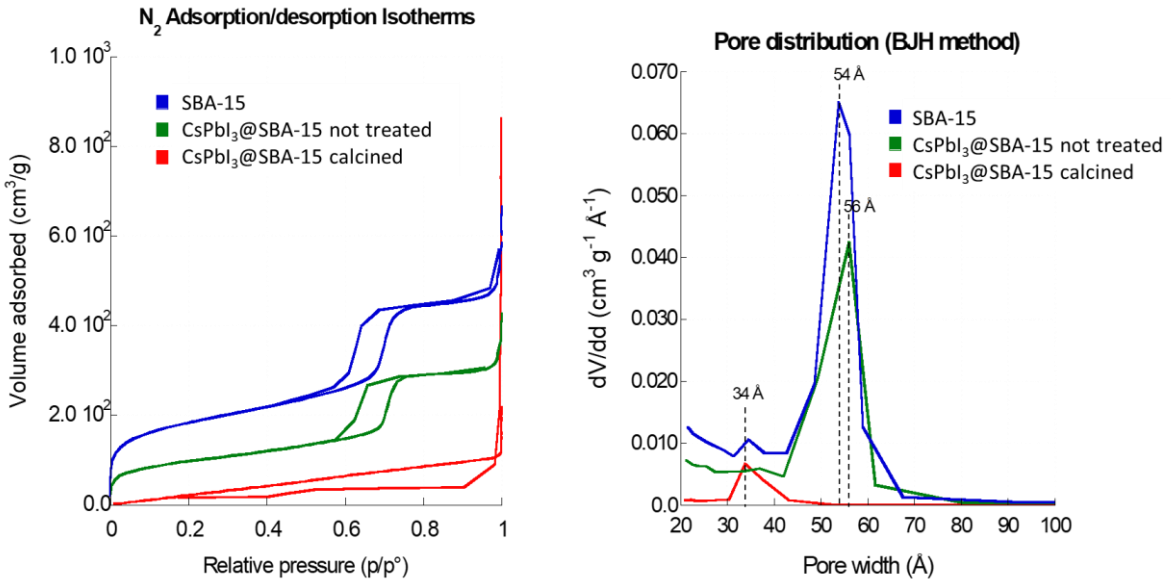

Figure 37: BET measurements on the sample $CsPbI_3$@SBA-15.

Although the presence of perovskite nanocrystals was evidenced in the porous matrix before the calcination process, X-ray diffraction measurements on treated samples did not provide good results. The high background from the silica matrix strongly overlaps the perovskites signal and, in particular, in the samples $CsPbCl_3$ and $CsPbI_3$ the characteristic peaks are below the background.

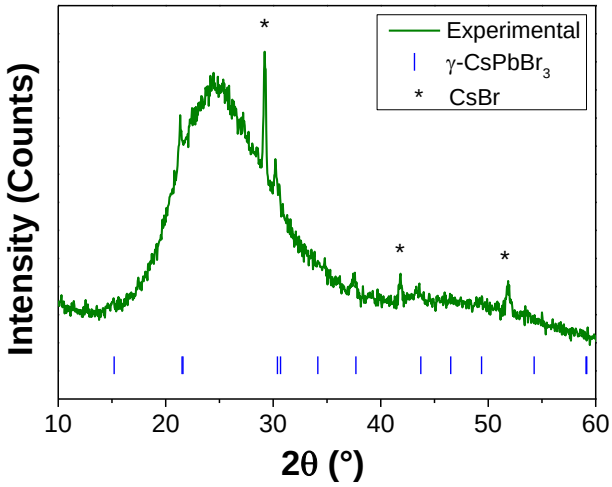

Figure 38: X-ray diffraction pattern of the sample $CsPbBr_3$@SBA-15.

Regarding the sample of $CsPbBr_3$@SBA-15 (Figure 38), the XRD pattern evidences the peaks at 21.3°, 30.2°, and 37.5° related to the presence of $CsPbBr_3$ in γ phase (ICSD 97851) and a broad peak around 24° related to the amorphous silica.

The differences in the XRD patterns among the samples were initially attributed to the different solubility in an aqueous solution of the starting precursors. After various attempts to improve the solubility, obtaining similar results, the synthesis was repeated in an inert atmosphere (Argon), evidencing the presence of PbX_2 precursors residuals in the furnace tube. Then, the further hypothesis was that in the case of $PbCl_2$ and PbI_2 the evaporation rate at the calcination temperature is higher than in the case of $PbBr_2$. As previously reported,[126] with annealing at high temperature, $CsPbI_3$ degrades to the secondary phase Cs_4PbI_6, because of the evaporation of PbI_2. If PbI_2 evaporates further, all that's left is CsI. Figure 38 shows the presence of CsBr together with $CsPbBr_3$, and that seems to confirm the aforementioned hypothesis evidencing the partial degradation of $CsPbBr_3$ as a result of the evaporation of $PbBr_2$.

6.2.2 Optical characterization

If the structural and morphological characterizations suffer from a lack of deep information, the optical characterization well described the behaviour and the properties of the samples.

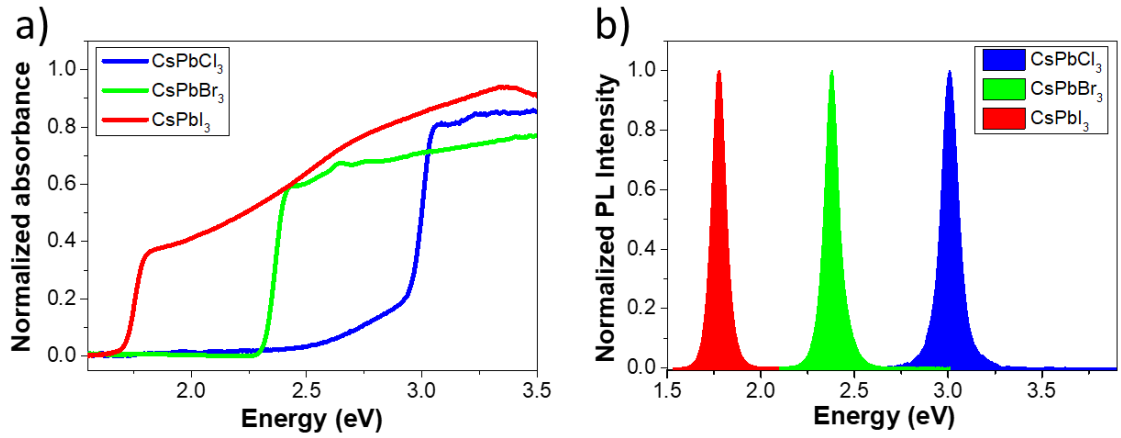

Figure 39: Absorption (a) and steady-state luminescence (b) spectra of $CsPbX_3$@MS; λ_{exc}=375 nm.

The absorption spectra are reported in Figure 39a. The typical spectra of lead inorganic perovskites are observed for all three samples, where the absorption threshold is reported at 1.77 eV, 2.38 eV, and 3.0 eV for the $CsPbI_3$, $CsPbBr_3$, and $CsPbCl_3$, respectively.

The emission spectra (Figure 39b) agree as well with the data reported in the literature; however, a slight blue shift is clearly present and, probably related to the nanometric dimension of the

nanocrystals. Actually, the dependence of the bandgap of perovskites synthesized in porous matrices has been described using the Brus equation that is valid for dimensions close to the Bohr radius[165]

$$E_{g,NC} = E_{g,bulk} + \frac{h^2}{8\mu R^2} - \frac{1{,}786e^2}{4\pi\varepsilon_0\varepsilon_r R}$$

The formula has three terms, Eg is the bandgap ($E_{g,NC}$ is the exciton lowest excited energy state within the nanocrystal, $E_{g,\,bulk}$ is the bandgap of the bulk perovskite), R is the radius of the nanoparticle, h is Planck's constant, μ is the exciton reduced mass, e is the electron charge, and ε_0 and ε_r are the dielectric constants of vacuum and of the perovskite, respectively. The second term represents the first energy level of a quasiparticle of reduced mass μ confined in a spherical well of radius R limited by a wall of infinite potential. The third term is the Coulomb energy, which results from the electrostatic interaction between electron and hole within the nanocrystal.

The energy shift in the three set of samples is in accord with the dimension of the template silica pores, being 8 nm for a blue shift of about 60-70 meV for each of them. In principle, the blue shift can be further increased by changing the initial pore size.[166,167] It is worth noting that the samples obtained in MCM-41 as templating matrix don't show further blue shift, but rather an inverse trend (Figure 40). In these samples, the mean pore diameter is 3.6 nm, but the behaviour of PL emission suggests that during the collapsing process, an agglomeration of NCs takes place.

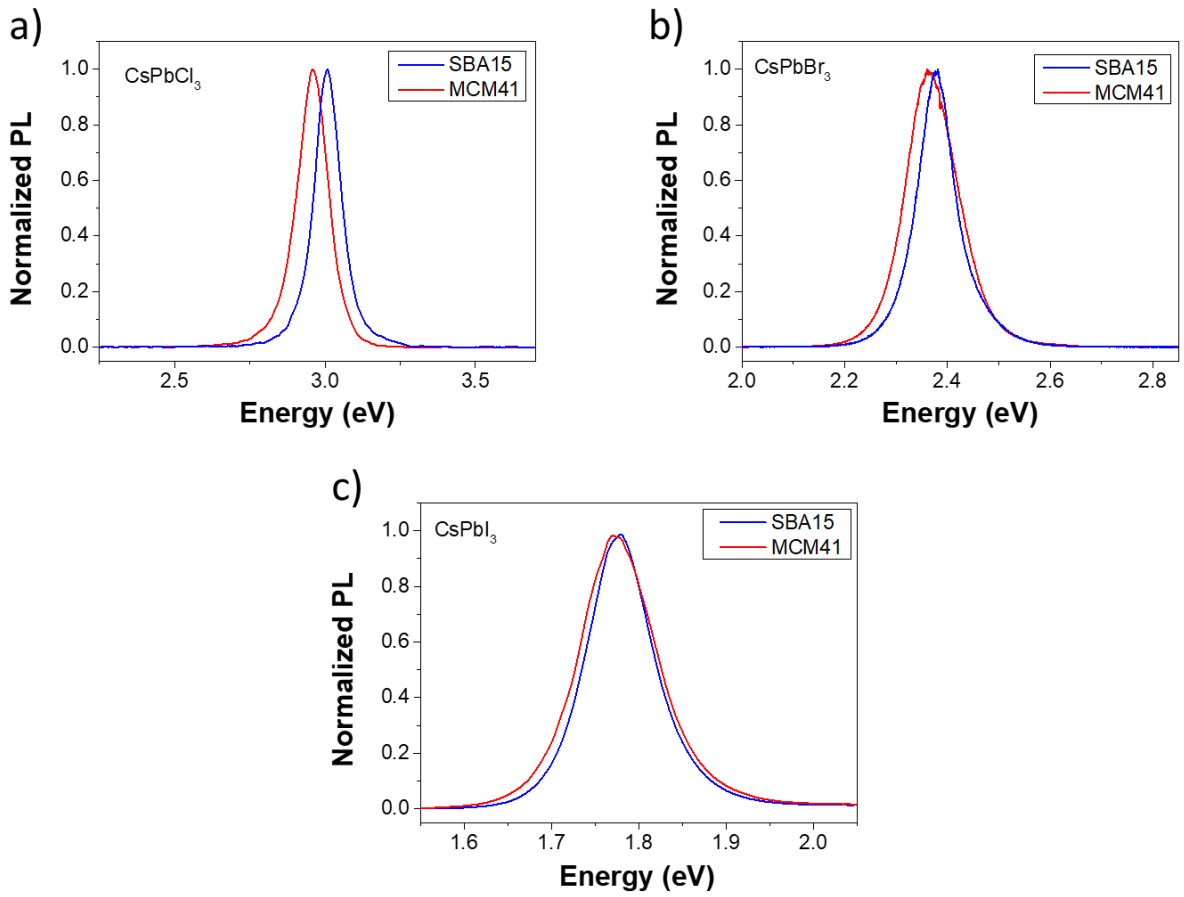

Figure 40: Comparison between the three set of samples in different silica matrices: a) $CsPbCl_3$, b) $CsPbBr_3$, c) $CsPbI_3$; λ_{exc}=375 nm.

Figure 41 reports the lifetime behaviour of the three different samples. The curves have been fitted with a multi-exponential decay function:

$$I(t) = I_0 + \sum_{i=1}^{n} A_i e^{-(t-t_0)/\tau_i}$$

With I(t) time-dependent PL intensity, I_0 initial PL intensity, A_i amplitude, t time, t_0 initial time, t_i the characteristic lifetime, n=2 for $CsPbCl_3$ and $CsPbBr_3$, and n=3 for $CsPbI_3$. Table 11 retrieves the fitting parameters. The average lifetime has been calculated using the following relation:[83]

$$\bar{\tau} = \frac{\sum_i A_i \cdot \tau_i^2}{\sum_i A_i \cdot \tau_i}$$

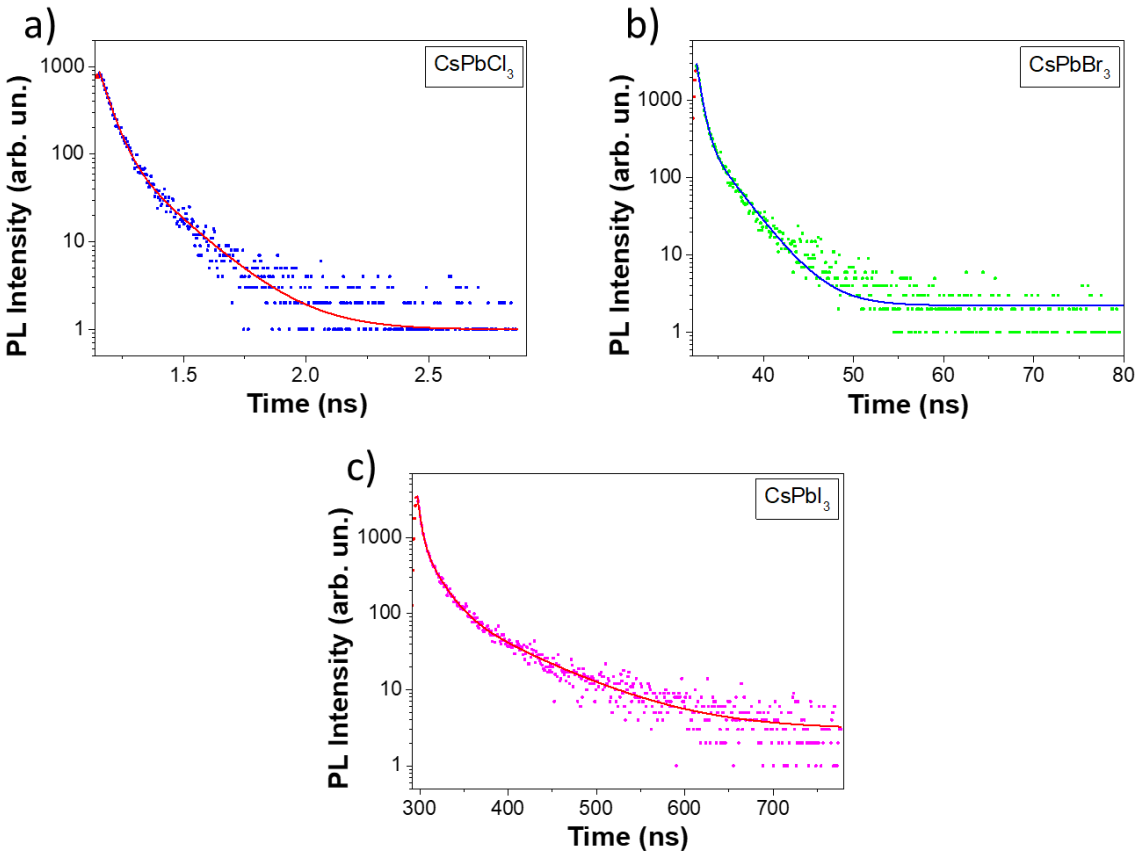

Figure 41: Time-resolved PL measurements of the samples $CsPbCl_3$@MS (a), $CsPbBr_3$@MS (b), $CsPbI_3$@MS (c); λ_{exc}=375 nm.

Table 11: Fit parameters of TR-PL measurements.

	$\bar{\tau}$ [ns]	A_1	τ_1 [ns]	A_2	τ_2 [ns]	A_3	τ_3 [ns]
$CsPbCl_3$	0.1	733.3	0.04	125.1	0.17		
$CsPbBr_3$	1.4	3266.8	0.52	380.6	2.81		
$CsPbI_3$	26.4	4603.8	3.76	961.7	17.2	146.5	75.6

The results for the different samples, 0.1 ns, 1.4 ns, and 26.4 ns agree with the values reported for pure perovskite nanocrystals,[32,166,167] strongly indicating the absence of new non-radiative paths connected to the surrounding silica matrix.

The observed luminescence time decay is related to the radiative and non-radiative path,

$$\frac{1}{\tau_{meas}} = \frac{1}{\tau_R} + \frac{1}{\tau_{nR}} = \gamma_R + \gamma_{nR}$$

where τ_{meas} is the decay time experimentally measured by time-resolved luminescence, τ_R and γ_R (τ_{nR} and γ_{nR}) are the decay time and transition rate for a radiative (non-radiative) process. The fastening of the measured decay is therefore the indication of the presence of new non radiative paths, and, oppositely, the unvaried values is related to the absence of interaction between the luminescence centre and the silica matrix.

6.2.3 Stability test

By taking advantage of such considerations, we tested the stability of the Silica/perovskites phosphors in different environmental conditions.

Considering that the quantum absolute efficiency is a tricky parameter in these samples (it is strongly altered by the surrounding Silica matrix, which increases the scattering effects and increases the uncertainty, as well by the overall ratio between the luminescent perovskites and the silica), the relative quantum efficiency could be considered a good indication about the presence of degradation effects.

Time-resolved luminescence measurements were acquired again, after leaving the samples in standard environmental conditions (about 20 °C in the air) for five months. Further, considering the detrimental effect of water in perovskites, the samples were left in water for 7 days.

The relative quantum efficiency can be calculated considering the equation

$$\eta = 1 - \frac{\tau_{new}}{\tau_{old}}$$

where τ_{old} represents the time decays constant measured immediately after the synthesis and τ_{new} the value obtained after the tests in different environmental conditions.

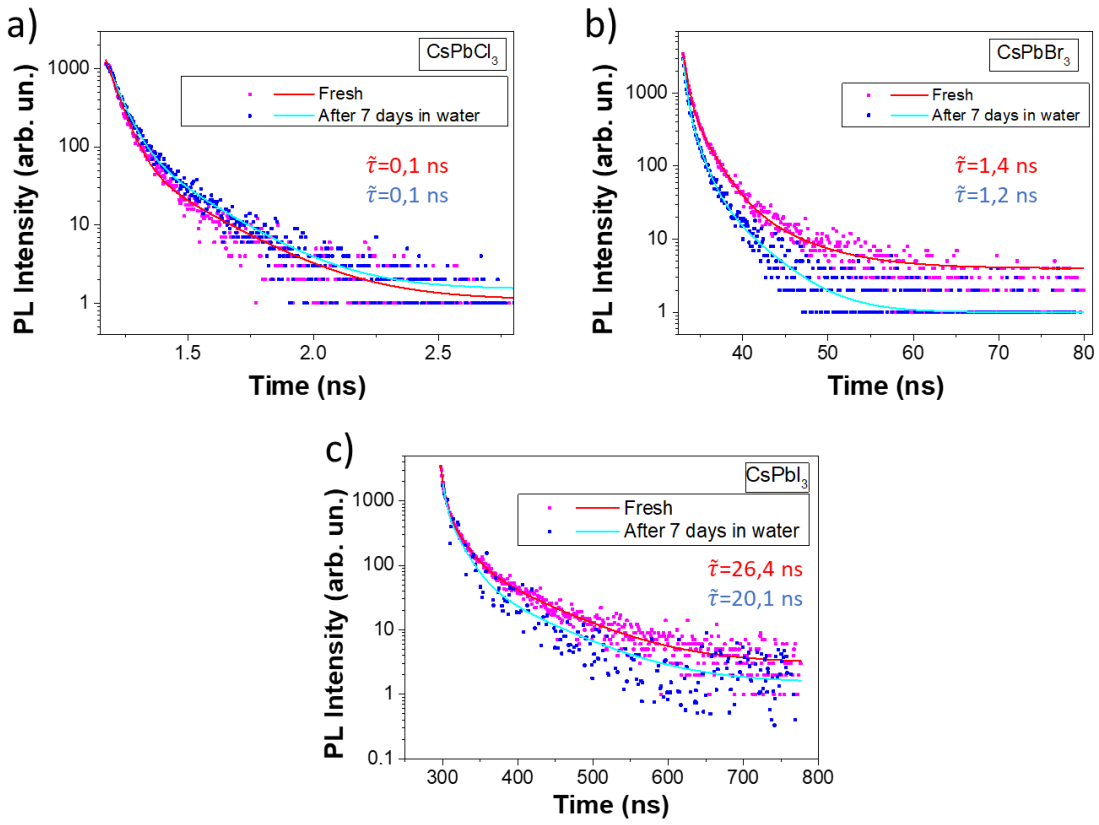

Figure 42: Time resolved PL measurements before and after the treatment in water: a) $CsPbCl_3$@MS, b) $CsPbBr_3$@MS, c) $CsPbI_3$@MS; λ_{exc}=375 nm.

The results indicate a very similar behaviour (Figure 42), evidencing a slight variation in the case of $CsPbBr_3$@MS and $CsPbI_3$@MS. The result is further confirmed by comparative luminescence measurements. The PL spectra were acquired in the same conditions, by carefully checking the experimental conditions to obtain a comparative estimation of the efficiency of the samples. Relative Quantum yield cannot give insights on the efficiency of the samples, being the ratio between photon absorbed on photon emitted, while absolute Quantum yield is difficult to accurately calculate for the high scattering from the silica shell. The results show a variation below the 5% that is below the accuracy of the experiment.

6.3 Device definition

As a final demonstration of the possibility to use the nano Perovskite/Silica compounds as suitable phosphors for down conversion, we define a very first prototype of an RGB matrix. The phosphors were embedded separated from each other in a transparent polymeric matrix to easily define the thickness and optical properties. Then, each phosphor was placed in a pre-assembled transparent matrix that will act as the front display. Such structure has been retro illuminated with a NUV LED (375 nm), acting as a back illuminating device (Figure 43).

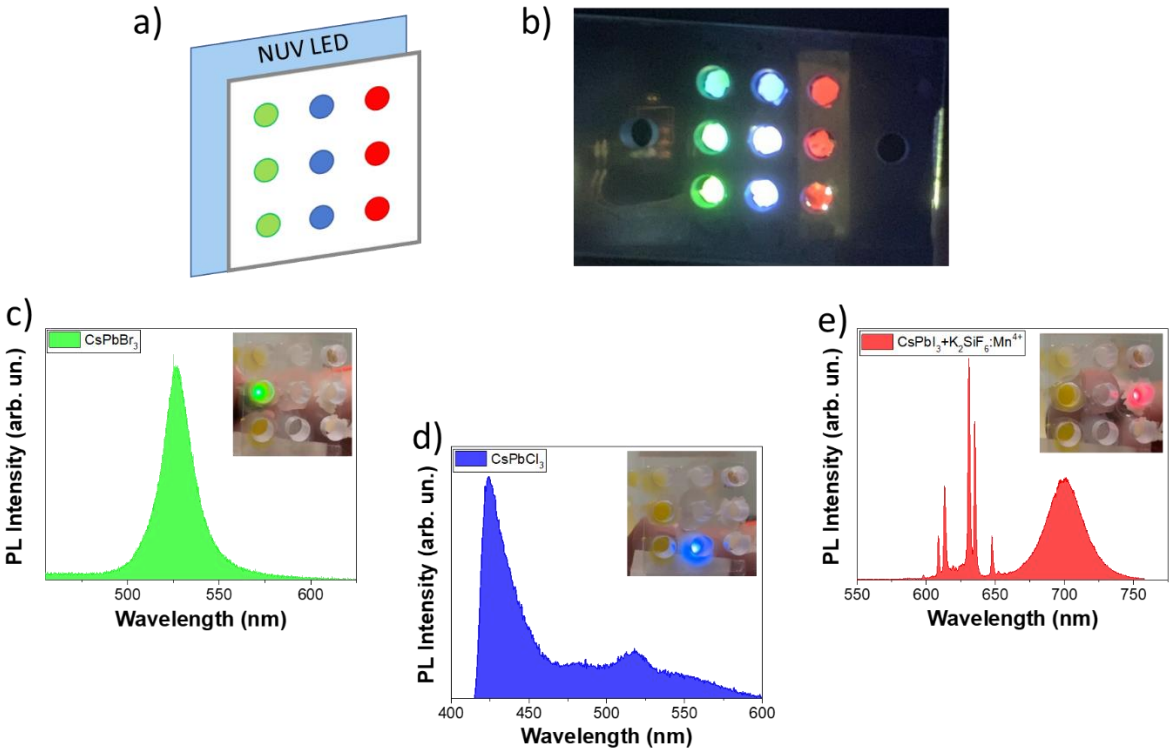

Figure 43: Preliminary device: RGB matrix, NUV source at 375 nm. a) sketch of the device, b) real prototype, c) $CsPbBr_3$@MS, d) $CsPbCl_3$@MS, e) $CsPbI_3$@MS and $K_2SiF_6:Mn^{4+}$.

As evidenced in Figure 43c,d the colour down conversion is easily obtained for the green ($CsPbBr_3$) and blue phosphors ($CsPbCl_3$). On the contrary, a poor result is obtained for the red phosphor ($CsPbI_3$). Different reasons are at the base of such effect, the first could be due to a reduced content of phosphor in the silica matrix, as previously indicated, connected to the higher evaporating rate of PbI_2 with respect to lead bromide and chloride. This assumption could be evidenced by the lower intensity in the overall emission, while cannot depend on the phase of the iodide perovskite. In this last case, the Raman spectrum would evidence the presence of δ-phase and the luminescent properties would evidence the broadband at about 550 nm. The absence of these features and the reduced intensity stronger indicate the lower amount of $CsPbI_3$ in the Silica matrix. Different attempts in this direction have been performed:

- increase the content of PbI_2 in a higher amount with respect to the correct stoichiometry;
- perform the synthesis in a controlled atmosphere: Argon, Nitrogen;
- static and fluxed atmosphere;
- closed heating chamber.

However, none of the above-mentioned techniques allowed to reach a higher efficiency. Despite the optical features of the samples synthesized in MCM-41 and SBA-15 being the same, a different efficiency is evidenced in the two set of samples. The samples in MCM-41 show brighter colours

under UV light. This further statement can confirm the above-reported considerations on the poor efficiency of $CsPbI_3$ samples. The calcination process for the samples encapsulated in SBA-15 takes place at higher temperature (800 °C instead of 600 °C), increasing the evaporation rate of all the lead halides.

Therefore, even considering the emission of $CsPbI_3$ at about 700 nm, where the human eye perception has a peak around 550 nm, we decided to use a further phosphor to increase the intensity and shift the emission at lower energy.

Among the different potential materials, we choose the $K_2SiF_6:Mn^{4+}$ for different reasons:

- the excitation spectrum overlaps the NUV pumping wavelength;
- narrow emissions between 600 and 650 nm;
- it acts as a potential sensitizer for $CsPbI_3$.

Figure 43e reports the RGB panel where the red phosphor is obtained by the mixing of red $CsPbI_3$ perovskite with $K_2SiF_6:Mn^{4+}$.

6.4 Conclusions

Summarizing, the goal was to stabilize inorganic lead halide perovskites, and realize a simple and stable prototype. Caesium lead halide perovskites have been encapsulated in silica matrices, showing good stability in ambient conditions and good resistance in water.

Despite the challenges related to the structural characterization, the analysis of optical properties allowed to study the interaction mechanism between the perovskites and the silica matrix. Moreover, the excellent emitting properties and the good stability permitted the realization of a simple and stable prototype of an RGB matrix, highlighting the opportunity of using inorganic lead halide perovskites as phosphors.

7 Conclusions

In conclusion, during these three years of Ph.D. all-inorganic perovskites have been synthesized and deeply characterized from the structural and optical point of view.

The work permitted to study different synthesis techniques and find new characterization methods to analyse the phase transition and the degradation processes of inorganic lead halide perovskites. Moreover, the study permitted to get insights on the stability of perovskites and their potential applications.

The vibrational analysis of α and δ-$CsPbI_3$ has been performed, making order in the assignation of Raman modes, and showing the potentiality of Raman Spectroscopy as fast technique to identify the polymorphs and study in-situ degradation processes. Moreover, focalizing on the solid–state synthesis of $CsPbI_3$, the effect of the synthesis duration has been studied. With a multi-technique approach it has been evidenced as the formation of the secondary phase Cs_4PbI_6 contributes to the stabilization of the luminescent γ-phase at room temperature.

In order to shed light on the stability of lead halide perovskites and their applications, the interaction with two different matrices has been studied.

A $CsPbBr_3$ NCs – Au heterostructure has been realized, evidencing the presence of an efficient charge transfer process. The result showed high potential appliance in all the applications where an efficient charge transfer is required. Further, the possibility to utilize the perovskite NCs as efficient sensitizer strongly suggest the possibility to achieve tunable photocatalityc device active in all the visible range.

A second heterostructure has been obtained from $CsPbX_3$ in mesoporous silica matrices. The encapsulation in the matrix, SBA15 and MCM41, contributed to the stabilization of inorganic lead halide perovskites against external factors. Preserving their excelent optical properties, perovskites proved to be suitable for display applications. On this basis, a first prototype of an RGB matrix backlight by near UV source has been realized.

8 References

[1] C. Li, X. Lu, W. Ding, L. Feng, Y. Gao, Z. Guo, *Acta Crystallogr. Sect. B Struct. Sci.* **2008**, *64*, 702–707.

[2] C. K. Møller, *Mat. Fys. Medd . Dan . Vid . Selsk* **1959**, *32*.

[3] D. B. Mitzi, in *Prog. Inorg. Chem.*, **2007**, pp. 1–121.

[4] H. Huang, L. Polavarapu, J. A. Sichert, A. S. Susha, A. S. Urban, A. L. Rogach, *NPG Asia Mater.* **2016**, *8*, e328–e328.

[5] NREL, *Best Res. Effic. Chart | Photovolt. Res. | NREL* **2020**, https://www.nrel.gov/pv/cell-efficiency.html.

[6] W.-J. Yin, T. Shi, Y. Yan, *J. Phys. Chem. C* **2015**, *119*, 5253–5264.

[7] G. Kim, A. Petrozza, *Adv. Energy Mater.* **2020**, *10*, 2001959.

[8] W. Travis, E. N. K. Glover, H. Bronstein, D. O. Scanlon, R. G. Palgrave, *Chem. Sci.* **2016**, *7*, 4548–4556.

[9] Z. Xiao, Y. Yan, *Adv. Energy Mater.* **2017**, *7*, 1701136.

[10] T. Leijtens, G. E. Eperon, N. K. Noel, S. N. Habisreutinger, A. Petrozza, H. J. Snaith, *Adv. Energy Mater.* **2015**, *5*, 1500963.

[11] S. Plesko, R. Kind, J. Roos, *J. Phys. Soc. Japan* **1978**, *45*, 553–557.

[12] M. Rodová, J. Brožek, K. Knížek, K. Nitsch, *J. Therm. Anal. Calorim.* **2003**, *71*, 667–673.

[13] A. Marronnier, G. Roma, S. Boyer-Richard, L. Pedesseau, J.-M. Jancu, Y. Bonnassieux, C. Katan, C. C. Stoumpos, M. G. Kanatzidis, J. Even, *ACS Nano* **2018**, *12*, 3477–3486.

[14] A. F. Akbulatov, S. Y. Luchkin, L. A. Frolova, N. N. Dremova, K. L. Gerasimov, I. S. Zhidkov, D. V. Anokhin, E. Z. Kurmaev, K. J. Stevenson, P. A. Troshin, *J. Phys. Chem. Lett.* **2017**, *8*, 1211–1218.

[15] B. Conings, J. Drijkoningen, N. Gauquelin, A. Babayigit, J. D'Haen, L. D'Olieslaeger, A. Ethirajan, J. Verbeeck, J. Manca, E. Mosconi, F. De Angelis, H.-G. Boyen, *Adv. Energy Mater.* **2015**, *5*, 1500477.

[16] E. J. Juarez-Perez, L. K. Ono, M. Maeda, Y. Jiang, Z. Hawash, Y. Qi, *J. Mater. Chem. A* **2018**, *6*, 9604–9612.

[17] B. R. Vincent, K. N. Robertson, T. S. Cameron, O. Knop, *Can. J. Chem.* **1987**, *65*, 1042–1046.

[18] J. Yang, B. D. Siempelkamp, D. Liu, T. L. Kelly, *ACS Nano* **2015**, *9*, 1955–1963.

[19] M. Shirayama, M. Kato, T. Miyadera, T. Sugita, T. Fujiseki, S. Hara, H. Kadowaki, D. Murata, M. Chikamatsu, H. Fujiwara, *J. Appl. Phys.* **2016**, *119*, 115501.

[20] J. S. Yun, J. Kim, T. Young, R. J. Patterson, D. Kim, J. Seidel, S. Lim, M. A. Green, S. Huang, A. Ho-Baillie, *Adv. Funct. Mater.* **2018**, *28*, 1705363.

[21] J. Lin, M. Lai, L. Dou, C. S. Kley, H. Chen, F. Peng, J. Sun, D. Lu, S. A. Hawks, C. Xie, F. Cui, A. P. Alivisatos, D. T. Limmer, P. Yang, *Nat. Mater.* **2018**, *17*, 261–267.

[22] M. Kuno, M. C. Brennan, *Matter* **2020**, *2*, 21–23.

[23] H. Zhang, X. Fu, Y. Tang, H. Wang, C. Zhang, W. W. Yu, X. Wang, Y. Zhang, M. Xiao, *Nat. Commun.* **2019**, *10*, 1088.

[24] A. F. Gualdrón-Reyes, S. J. Yoon, E. M. Barea, S. Agouram, V. Muñoz-Sanjosé, Á. M. Meléndez, M. E. Niño-Gómez, I. Mora-Seró, *ACS Energy Lett.* **2019**, *4*, 54–62.

[25] Y. Zu, J. Dai, L. Li, F. Yuan, X. Chen, Z. Feng, K. Li, X. Song, F. Yun, Y. Yu, B. Jiao, H. Dong, X. Hou, M. Ju, Z. Wu, *J. Mater. Chem. A* **2019**, *7*, 26116–26122.

[26] C. Sun, X. Wang, Y. Xu, W. Lu, X. Teng, G. Fu, W. Yu, *Appl. Surf. Sci.* **2020**, *508*, 145188.

[27] X. Li, Y. Wu, S. Zhang, B. Cai, Y. Gu, J. Song, H. Zeng, *Adv. Funct. Mater.* **2016**, *26*, 2584–2584.

[28] W. Ke, I. Spanopoulos, C. C. Stoumpos, M. G. Kanatzidis, *Nat. Commun.* **2018**, *9*, 4785.

[29] Q. Zhao, A. Hazarika, L. T. Schelhas, J. Liu, E. A. Gaulding, G. Li, M. Zhang, M. F. Toney, P. C. Sercel, J. M. Luther, *ACS Energy Lett.* **2020**, *5*, 238–247.

[30] B. Luo, F. Li, K. Xu, Y. Guo, Y. Liu, Z. Xia, J. Z. Zhang, *J. Mater. Chem. C* **2019**, *7*, 2781–2808.

[31] Q. A. Akkerman, D. Meggiolaro, Z. Dang, F. De Angelis, L. Manna, *ACS Energy Lett.* **2017**, *2*, 2183–2186.

[32] L. Protesescu, S. Yakunin, M. I. Bodnarchuk, F. Krieg, R. Caputo, C. H. Hendon, R. X. Yang, A. Walsh, M. V. Kovalenko, *Nano Lett.* **2015**, *15*, 3692–3696.

[33] B. T. Diroll, H. Zhou, R. D. Schaller, *Adv. Funct. Mater.* **2018**, *28*, 1800945.

[34] P. Luo, W. Xia, S. Zhou, L. Sun, J. Cheng, C. Xu, Y. Lu, *J. Phys. Chem. Lett.* **2016**, *7*, 3603–3608.

[35] Q. Wang, X. Zheng, Y. Deng, J. Zhao, Z. Chen, J. Huang, *Joule* **2017**, *1*, 371–382.

[36] B. Li, Y. Zhang, L. Fu, T. Yu, S. Zhou, L. Zhang, L. Yin, *Nat. Commun.* **2018**, *9*, 1076.

[37] B. Jeong, H. Han, Y. J. Choi, S. H. Cho, E. H. Kim, S. W. Lee, J. S. Kim, C. Park, D. Kim, C. Park, *Adv. Funct. Mater.* **2018**, *28*, 1706401.

[38] X. Jia, C. Zuo, S. Tao, K. Sun, Y. Zhao, S. Yang, M. Cheng, M. Wang, Y. Yuan, J. Yang, F. Gao, G. Xing, Z. Wei, L. Zhang, H.-L. Yip, M. Liu, Q. Shen, L. Yin, L. Han, S. Liu, L. Wang, J. Luo, H. Tan, Z. Jin, L. Ding, *Sci. Bull.* **2019**, *64*, 1532–1539.

[39] A. Swarnkar, A. R. Marshall, E. M. Sanehira, B. D. Chernomordik, D. T. Moore, J. A.

Christians, T. Chakrabarti, J. M. Luther, *Science (80-.).* **2016**, *354*, 92–95.

[40] J. Deng, J. Li, Z. Yang, M. Wang, *J. Mater. Chem. C* **2019**, *7*, 12415–12440.

[41] X. Li, Y. Wu, S. Zhang, B. Cai, Y. Gu, J. Song, H. Zeng, *Adv. Funct. Mater.* **2016**, *26*, 2435–2445.

[42] P. C. Ricci, C. M. Carbonaro, L. Stagi, M. Salis, A. Casu, S. Enzo, F. Delogu, *J. Phys. Chem. C* **2013**, *117*, 7850–7857.

[43] G. Pezzotti, A. A. Porporati, *J. Biomed. Opt.* **2004**, *9*, 372.

[44] C. A. Chen, Y. S. Huang, W. H. Chung, D. S. Tsai, K. K. Tiong, *J. Mater. Sci. Mater. Electron.* **2009**, *20*, 303–306.

[45] S. Xiang, Z. Fu, W. Li, Y. Wei, J. Liu, H. Liu, L. Zhu, R. Zhang, H. Chen, *ACS Energy Lett.* **2018**, *3*, 1824–1831.

[46] K. E. A. Hooper, H. K. H. Lee, M. J. Newman, S. Meroni, J. Baker, T. M. Watson, W. C. Tsoi, *Phys. Chem. Chem. Phys.* **2017**, *19*, 5246–5253.

[47] D. B. Straus, S. Guo, R. J. Cava, *J. Am. Chem. Soc.* **2019**, *141*, 11435–11439.

[48] W. Zhou, F. Sui, G. Zhong, G. Cheng, M. Pan, C. Yang, S. Ruan, *J. Phys. Chem. Lett.* **2018**, *9*, 4915–4920.

[49] T. Ben Uliel, L. Gouda, H. Aviv, A. Itzhak, Y. R. Tischler, *J. Raman Spectrosc.* **2019**, *50*, 1672–1678.

[50] P. Giannozzi, S. Baroni, N. Bonini, M. Calandra, R. Car, C. Cavazzoni, D. Ceresoli, G. L. Chiarotti, M. Cococcioni, I. Dabo, A. Dal Corso, S. de Gironcoli, S. Fabris, G. Fratesi, R. Gebauer, U. Gerstmann, C. Gougoussis, A. Kokalj, M. Lazzeri, L. Martin-Samos, N. Marzari, F. Mauri, R. Mazzarello, S. Paolini, A. Pasquarello, L. Paulatto, C. Sbraccia, S. Scandolo, G. Sclauzero, A. P. Seitsonen, A. Smogunov, P. Umari, R. M. Wentzcovitch, *J. Phys. Condens. Matter* **2009**, *21*, 395502.

[51] J. P. Perdew, K. Burke, M. Ernzerhof, *Phys. Rev. Lett.* **1996**, *77*, 3865–3868.

[52] N. Troullier, J. L. Martins, *Phys. Rev. B* **1991**, *43*, 1993–2006.

[53] P. Giannozzi, S. de Gironcoli, P. Pavone, S. Baroni, *Phys. Rev. B* **1991**, *43*, 7231–7242.

[54] M. Lazzeri, F. Mauri, *Phys. Rev. Lett.* **2003**, *90*, 036401.

[55] D. L. Rousseau, R. P. Bauman, S. P. S. Porto, *J. Raman Spectrosc.* **1981**, *10*, 253–290.

[56] K. Nakamoto, in *Handb. Vib. Spectrosc.* (Ed.: P.R. Griffiths), John Wiley & Sons, Ltd, Chichester, UK, **2006**, p. 419.

[57] K. Momma, F. Izumi, *J. Appl. Crystallogr.* **2011**, *44*, 1272–1276.

[58] M. Lai, Q. Kong, C. G. Bischak, Y. Yu, L. Dou, S. W. Eaton, N. S. Ginsberg, P. Yang, *Nano Res.* **2017**, *10*, 1107–1114.

[59] R. J. Sutton, M. R. Filip, A. A. Haghighirad, N. Sakai, B. Wenger, F. Giustino, H. J. Snaith, *ACS Energy Lett.* **2018**, *3*, 1787–1794.

[60] J. Brgoch, A. J. Lehner, M. Chabinyc, R. Seshadri, *J. Phys. Chem. C* **2014**, *118*, 27721–27727.

[61] M. Ahmad, G. Rehman, L. Ali, M. Shafiq, R. Iqbal, R. Ahmad, T. Khan, S. Jalali-Asadabadi, M. Maqbool, I. Ahmad, *J. Alloys Compd.* **2017**, *705*, 828–839.

[62] M. Bradley, *Thermo Fish. Sci. Appl. Note* **2007**, AN50733.

[63] Y. Li, X. Xu, C. Wang, B. Ecker, J. Yang, J. Huang, Y. Gao, *J. Phys. Chem. C* **2017**, *121*, 3904–3910.

[64] J. S. Niezgoda, B. J. Foley, A. Z. Chen, J. J. Choi, *ACS Energy Lett.* **2017**, *2*, 1043–1049.

[65] L. Burgio, R. J. H. Clark, S. Firth, *Analyst* **2001**, *126*, 222–227.

[66] A. J. Forty, *Philos. Mag.* **1960**, *5*, 787–797.

[67] G. Popov, M. Mattinen, T. Hatanpää, M. Vehkamäki, M. Kemell, K. Mizohata, J. Räisänen, M. Ritala, M. Leskelä, *Chem. Mater.* **2019**, *31*, 1101–1109.

[68] H. Mehdi, A. Mhamdi, R. Hannachi, A. Bouazizi, *RSC Adv.* **2019**, *9*, 12906–12912.

[69] D. Huang, P. Xie, Z. Pan, H. Rao, X. Zhong, *J. Mater. Chem. A* **2019**, *7*, 22420–22428.

[70] M. Konstantakou, D. Perganti, P. Falaras, T. Stergiopoulos, *Crystals* **2017**, *7*, 291.

[71] P. Wang, X. Zhang, Y. Zhou, Q. Jiang, Q. Ye, Z. Chu, X. Li, X. Yang, Z. Yin, J. You, *Nat. Commun.* **2018**, *9*, 2225.

[72] Y. El Ajjouri, F. Palazon, M. Sessolo, H. J. Bolink, *Chem. Mater.* **2018**, *30*, 7423–7427.

[73] A. Karmakar, M. S. Dodd, X. Zhang, M. S. Oakley, M. Klobukowski, V. K. Michaelis, *Chem. Commun.* **2019**, *55*, 5079–5082.

[74] Z. Hong, D. Tan, R. A. John, Y. K. E. Tay, Y. K. T. Ho, X. Zhao, T. C. Sum, N. Mathews, F. García, H. Sen Soo, *iScience* **2019**, *16*, 312–325.

[75] J. Satta, C. Melis, C. M. Carbonaro, A. Pinna, M. Salado, D. Salazar, P. C. Ricci, *J. Mater.* **2021**, *7*, 127–135.

[76] L. Lutterotti, *Nucl. Instruments Methods Phys. Res. Sect. B Beam Interact. with Mater. Atoms* **2010**, *268*, 334–340.

[77] Q. Zhang, Y. Zhou, Y. Wei, M. Tai, H. Nan, Y. Gu, J. Han, X. Yin, J. Li, H. Lin, *J. Mater. Chem. C* **2020**, *8*, 2569–2578.

[78] Y. Yang, J. P. Robbins, L. Ezeonu, Y. Ma, N. Sparta, X. Kong, S. Strauf, S. G. Podkolzin, S. S. Lee, *J. Mater. Chem. C* **2020**, *8*, 8896–8903.

[79] F. Liu, Y. Zhang, C. Ding, S. Kobayashi, T. Izuishi, N. Nakazawa, T. Toyoda, T. Ohta, S. Hayase, T. Minemoto, K. Yoshino, S. Dai, Q. Shen, *ACS Nano* **2017**, *11*, 10373–10383.

[80] B. Zhao, S.-F. Jin, S. Huang, N. Liu, J.-Y. Ma, D.-J. Xue, Q. Han, J. Ding, Q.-Q. Ge, Y. Feng, J.-S. Hu, *J. Am. Chem. Soc.* **2018**, *140*, 11716–11725.

[81] V. Babin, A. Krasnikov, M. Nikl, K. Nitsch, A. Stolovits, S. Zazubovich, *J. Lumin.* **2003**, *101*, 219–226.

[82] C. Chen, L. Zhang, T. Shi, G. Liao, Z. Tang, *Nanomaterials* **2019**, *9*, 1751.

[83] J. R. Lakowicz, *Principles of Fluorescence Spectroscopy*, Springer US, Boston, MA, **2006**.

[84] P. Becker, J. A. Márquez, J. Just, A. Al-Ashouri, C. Hages, H. Hempel, M. Jošt, S. Albrecht, R. Frahm, T. Unold, *Adv. Energy Mater.* **2019**, *9*, 1900555.

[85] Y. Zhou, Y. Zhao, *Energy Environ. Sci.* **2019**, *12*, 1495–1511.

[86] I. Deretzis, C. Bongiorno, G. Mannino, E. Smecca, S. Sanzaro, S. Valastro, G. Fisicaro, A. La Magna, A. Alberti, *Nanomaterials* **2021**, *11*, 1282.

[87] A. Swarnkar, A. R. Marshall, E. M. Sanehira, B. D. Chernomordik, D. T. Moore, J. A. Christians, T. Chakrabarti, J. M. Luther, *Science (80-.).* **2016**, *354*, 92–95.

[88] W. van der Stam, J. J. Geuchies, T. Altantzis, K. H. W. van den Bos, J. D. Meeldijk, S. Van Aert, S. Bals, D. Vanmaekelbergh, C. de Mello Donega, *J. Am. Chem. Soc.* **2017**, *139*, 4087–4097.

[89] L. Wu, H. Hu, Y. Xu, S. Jiang, M. Chen, Q. Zhong, D. Yang, Q. Liu, Y. Zhao, B. Sun, Q. Zhang, Y. Yin, *Nano Lett.* **2017**, *17*, 5799–5804.

[90] L. Rao, Y. Tang, C. Yan, J. Li, G. Zhong, K. Tang, B. Yu, Z. Li, J. Z. Zhang, *J. Mater. Chem. C* **2018**, *6*, 5375–5383.

[91] W. Lv, X. Tang, L. Li, L. Xu, M. Li, R. Chen, W. Huang, *J. Phys. Chem. C* **2019**, *123*, 24313–24320.

[92] X. Yu, L. Wu, H. Hu, M. Chen, Y. Tan, D. Yang, Q. Pan, Q. Zhong, T. Supasai, Q. Zhang, *Langmuir* **2018**, *34*, 10363–10370.

[93] L. Wu, H. Hu, Y. Xu, S. Jiang, M. Chen, Q. Zhong, D. Yang, Q. Liu, Y. Zhao, B. Sun, Q. Zhang, Y. Yin, *Nano Lett.* **2017**, *17*, 5799–5804.

[94] A. Pan, M. Jurow, Y. Zhao, F. Qiu, Y. Liu, J. Yang, J. J. Urban, L. He, Y. Liu, *Nanoscale* **2017**, *9*, 17688–17693.

[95] A. Rubino, L. Caliò, A. García-Bennett, M. E. Calvo, H. Míguez, *Adv. Opt. Mater.* **2020**, *8*, 1901868.

[96] A. Yan, Y. Guo, C. Liu, Z. Deng, Y. Guo, X. Zhao, *Nanoscale Res. Lett.* **2018**, *13*, 185.

[97] Y. Tong, E. Bladt, M. F. Aygüler, A. Manzi, K. Z. Milowska, V. A. Hintermayr, P. Docampo, S. Bals, A. S. Urban, L. Polavarapu, J. Feldmann, *Angew. Chemie Int. Ed.* **2016**, *55*, 13887–13892.

[98] Z. Long, H. Ren, J. Sun, J. Ouyang, N. Na, *Chem. Commun.* **2017**, *53*, 9914–9917.

[99] Y. Li, H. Huang, Y. Xiong, S. V. Kershaw, A. L. Rogach, *Angew. Chemie Int. Ed.* **2018**, *57*, 5833–5837.

[100] M. Chen, Y. Zou, L. Wu, Q. Pan, D. Yang, H. Hu, Y. Tan, Q. Zhong, Y. Xu, H. Liu, B. Sun, Q. Zhang, *Adv. Funct. Mater.* **2017**, *27*, 1701121.

[101] L. Wang, D. Ma, C. Guo, X. Jiang, M. Li, T. Xu, J. Zhu, B. Fan, W. Liu, G. Shao, H. Xu, H. Wang, R. Zhang, H. Lu, *Appl. Surf. Sci.* **2021**, *543*, 148782.

[102] M. K. Hossain, R. dos Reis, W. Qarony, Y. H. Tsang, J. C. Ho, K. M. Yu, *J. Mater. Chem. C* **2021**, *9*, 3229–3238.

[103] Z. Liang, S. Zhao, Z. Xu, B. Qiao, P. Song, D. Gao, X. Xu, *ACS Appl. Mater. Interfaces* **2016**, *8*, 28824–28830.

[104] Y. Gao, L. Zhao, Q. Shang, Y. Zhong, Z. Liu, J. Chen, Z. Zhang, J. Shi, W. Du, Y. Zhang, S. Chen, P. Gao, X. Liu, X. Wang, Q. Zhang, *Adv. Mater.* **2018**, *30*, 1801805.

[105] Y. Bekenstein, B. A. Koscher, S. W. Eaton, P. Yang, A. P. Alivisatos, *J. Am. Chem. Soc.* **2015**, *137*, 16008–16011.

[106] S. Wei, Y. Yang, X. Kang, L. Wang, L. Huang, D. Pan, *Chem. Commun.* **2016**, *52*, 7265–7268.

[107] H. Wu, Y. Zhang, M. Lu, X. Zhang, C. Sun, T. Zhang, V. L. Colvin, W. W. Yu, *Nanoscale* **2018**, *10*, 4173–4178.

[108] J. Bo, X. Sun, P. Wan, D. Huang, X. Chen, M. Chen, R. Li, D. Shen, Q. Li, W. Xia, Z. Ye, Y. Chen, S. Chen, *J. Phys. Chem. Lett.* **2021**, *12*, 9115–9123.

[109] M. Imran, P. Ijaz, D. Baranov, L. Goldoni, U. Petralanda, Q. Akkerman, A. L. Abdelhady, M. Prato, P. Bianchini, I. Infante, L. Manna, *Nano Lett.* **2018**, *18*, 7822–7831.

[110] Y. Liu, F. Li, Q. Liu, Z. Xia, *Chem. Mater.* **2018**, *30*, 6922–6929.

[111] H. Li, Y. Qian, X. Xing, J. Zhu, X. Huang, Q. Jing, W. Zhang, C. Zhang, Z. Lu, *J. Phys. Chem. C* **2018**, *122*, 12994–13000.

[112] M. Lu, X. Zhang, X. Bai, H. Wu, X. Shen, Y. Zhang, W. Zhang, W. Zheng, H. Song, W. W. Yu, A. L. Rogach, *ACS Energy Lett.* **2018**, *3*, 1571–1577.

[113] C. Bi, S. Wang, Q. Li, S. V. Kershaw, J. Tian, A. L. Rogach, *J. Phys. Chem. Lett.* **2019**, *10*, 943–952.

[114] S. Wei, H. Zhu, J. Zhang, L. Wang, M. An, Y. Wang, X. Zhang, Y. Liu, *J. Alloys Compd.* **2019**, *789*, 209–214.

[115] Y. Xie, Y. Yu, J. Gong, C. Yang, P. Zeng, Y. Dong, B. Yang, R. Liang, Q. Ou, S. Zhang, *Opt. Mater. Express* **2018**, *8*, 3494.

[116] A. Loiudice, S. Saris, E. Oveisi, D. T. L. Alexander, R. Buonsanti, *Angew. Chemie Int. Ed.* **2017**, *56*, 10696–10701.

[117] S. Park, M. N. An, G. Almeida, F. Palazon, D. Spirito, R. Krahne, Z. Dang, L. De Trizio, L. Manna, *Nanoscale* **2019**, *11*, 18739–18745.

[118] X. Di, L. Shen, J. Jiang, M. He, Y. Cheng, L. Zhou, X. Liang, W. Xiang, *J. Alloys Compd.* **2017**, *729*, 526–532.

[119] W. Shi, X. Zhang, K. Matras-Postolek, P. Yang, *ACS Appl. Nano Mater.* **2021**, *4*, 9391–9400.

[120] Y. Zong, T. Yang, P. Hao, B. Shan, B. Peng, X. Hu, R. Tao, X. Chen, P. Wu, K. Zhang, *Microporous Mesoporous Mater.* **2020**, *302*, 110229.

[121] J. Cuan, D. Zhang, W. Xing, J. Han, H. Zhou, Y. Zhou, *Chem. Eng. J.* **2021**, *425*, 131556.

[122] J.-Y. Sun, F. T. Rabouw, X.-F. Yang, X.-Y. Huang, X.-P. Jing, S. Ye, Q.-Y. Zhang, *Adv. Funct. Mater.* **2017**, *27*, 1704371.

[123] S. Saris, V. Niemann, V. Mantella, A. Loiudice, R. Buonsanti, *Nanoscale* **2019**, *11*, 19543–19550.

[124] J. S. Shaikh, N. S. Shaikh, S. S. Mali, J. V. Patil, S. A. Beknalkar, A. P. Patil, N. L. Tarwal, P. Kanjanaboos, C. K. Hong, P. S. Patil, *ChemSusChem* **2019**, *12*, 4724–4753.

[125] J. Zhang, W. Zhang, H.-M. Cheng, S. R. P. Silva, *Mater. Today* **2020**, *39*, 66–88.

[126] J. Satta, A. Casu, D. Chiriu, C. M. Carbonaro, L. Stagi, P. C. Ricci, *Nanomaterials* **2021**, *11*, 1823.

[127] H. Cho, Y.-H. Kim, C. Wolf, H.-D. Lee, T.-W. Lee, *Adv. Mater.* **2018**, *30*, 1704587.

[128] N. M. Dimitrijević, T. Rajh, S. P. Ahrenkiel, J. M. Nedeljković, O. I. Mićić, A. J. Nozik, *J. Phys. Chem. B* **2005**, *109*, 18243–18249.

[129] M. T. Sheldon, P.-E. Trudeau, T. Mokari, L.-W. Wang, A. P. Alivisatos, *Nano Lett.* **2009**, *9*, 3676–3682.

[130] K. C. Nawrot, D. Wawrzyńczyk, O. Bezkrovnyi, L. Kępiński, B. Cichy, M. Samoć, M. Nyk, *Nanomaterials* **2020**, *10*, 715.

[131] H. Wei, D. Ratchford, X. (Elaine) Li, H. Xu, C.-K. Shih, *Nano Lett.* **2009**, *9*, 4168–4171.

[132] S. Dey, J. Zhao, *J. Phys. Chem. Lett.* **2016**, *7*, 2921–2929.

[133] Y. Ding, Z. Zhang, in *Nanoporous Met. Adv. Energy Technol.*, Springer International Publishing, Cham, **2016**, pp. 1–35.

[134] V. Zielasek, B. Jürgens, C. Schulz, J. Biener, M. M. Biener, A. V. Hamza, M. Bäumer, *Angew. Chemie Int. Ed.* **2006**, *45*, 8241–8244.

[135] F. Ruffino, M. G. Grimaldi, *Coatings 2020, Vol. 10, Page 899* **2020**, *10*, 899.

[136] S. O. Kucheyev, J. R. Hayes, J. Biener, T. Huser, C. E. Talley, A. V. Hamza, *Appl. Phys. Lett.* **2006**, *89*, 053102.

[137] L. Zhang, Y. Song, T. Fujita, Y. Zhang, M. Chen, T.-H. Wang, *Adv. Mater.* **2014**, *26*, 1289–1294.

[138] J. Biener, A. Wittstock, L. A. Zepeda-Ruiz, M. M. Biener, V. Zielasek, D. Kramer, R. N. Viswanath, J. Weissmüller, M. Bäumer, A. V. Hamza, *Nat. Mater. 2009 81* **2008**, *8*, 47–51.

[139] J. M. Gonçalves, A. Kumar, M. I. da Silva, H. E. Toma, P. R. Martins, K. Araki, M. Bertotti, L. Angnes, *Energy Technol.* **2021**, *9*, 2000927.

[140] S. Carretero-Palacios, A. Jiménez-Solano, H. Míguez, *ACS Energy Lett.* **2016**, *1*, 323–331.

[141] J.-F. Liao, Y.-T. Cai, J.-Y. Li, Y. Jiang, X.-D. Wang, H.-Y. Chen, D.-B. Kuang, *J. Energy Chem.* **2021**, *53*, 309–315.

[142] X. Zhou, C. Bao, F. Li, H. Gao, T. Yu, J. Yang, W. Zhu, Z. Zou, *RSC Adv.* **2015**, *5*, 58543–58548.

[143] J. Song, J. Li, L. Xu, J. Li, F. Zhang, B. Han, Q. Shan, H. Zeng, *Adv. Mater.* **2018**, *30*, 1800764.

[144] I. McCue, E. Benn, B. Gaskey, J. Erlebacher, *Annu. Rev. Mater. Res.* **2016**, *46*, 263–286.

[145] G. Pia, M. Mascia, F. Delogu, *Scr. Mater.* **2014**, *76*, 57–60.

[146] Z. Qin, S. Dai, V. G. Hadjiev, C. Wang, L. Xie, Y. Ni, C. Wu, G. Yang, S. Chen, L. Deng, Q. Yu, G. Feng, Z. M. Wang, J. Bao, *Chem. Mater.* **2019**, *31*, 9098–9104.

[147] O. Yaffe, Y. Guo, L. Z. Tan, D. A. Egger, T. Hull, C. C. Stoumpos, F. Zheng, T. F. Heinz, L. Kronik, M. G. Kanatzidis, J. S. Owen, A. M. Rappe, M. A. Pimenta, L. E. Brus, *Phys. Rev. Lett.* **2017**, *118*, 136001.

[148] M. Liu, J. Zhao, Z. Luo, Z. Sun, N. Pan, H. Ding, X. Wang, *Chem. Mater.* **2018**, *30*, 5846–5852.

[149] L.-Q. Xie, T.-Y. Zhang, L. Chen, N. Guo, Y. Wang, G.-K. Liu, J.-R. Wang, J.-Z. Zhou, J.-W. Yan, Y.-X. Zhao, B.-W. Mao, Z.-Q. Tian, *Phys. Chem. Chem. Phys.* **2016**, *18*, 18112–18118.

[150] J. Xiao, L. Qi, *Nanoscale* **2011**, *3*, 1383.

[151] J. E. Millstone, S. J. Hurst, G. S. Métraux, J. I. Cutler, C. A. Mirkin, *Small* **2009**, *5*, 646–664.

[152] Muniba, G. Naz, M. N. Anjum, M. Irfan, M. Irfan, M. Arshad, S. Z. Bajwa, W. S. Khan, *Results Mater.* **2020**, *5*, 100065.

[153] J. Chen, Z. Shen, P. Liu, Z. Sun, J. G. Liu, C. Shen, D. Song, S. Zhao, Z. Xu, *Nanotechnology* **2021**, *32*, 325202.

[154] S. K. Balakrishnan, P. V. Kamat, *ACS Energy Lett.* **2017**, *2*, 88–93.

[155] M. A. Reed, *J. Vac. Sci. Technol. B Microelectron. Nanom. Struct.* **1986**, *4*, 358.

[156] O. Chen, J. Zhao, V. P. Chauhan, J. Cui, C. Wong, D. K. Harris, H. Wei, H.-S. Han, D. Fukumura, R. K. Jain, M. G. Bawendi, *Nat. Mater.* **2013**, *12*, 445–451.

[157] P. Ramasamy, N. Kim, Y.-S. Kang, O. Ramirez, J.-S. Lee, *Chem. Mater.* **2017**, *29*, 6893–6899.

[158] S. Tsukuda, T. Omata, *J. Soc. Inf. Disp.* **2020**, *28*, 680–690.

[159] European Commission, "COMMISSION DELEGATED DIRECTIVE (EU) 2015/863 of 31 March 2015 amending Annex II to Directive 2011/65/EU of the European Parliament and of the Council as regards the list of restricted substances," can be found under https://eur-lex.europa.eu/eli/dir_del/2015/863/oj, **2015**.

[160] G. Xu, S. Zeng, B. Zhang, M. T. Swihart, K.-T. Yong, P. N. Prasad, *Chem. Rev.* **2016**, *116*, 12234–12327.

[161] W.-C. Chao, T.-H. Chiang, Y.-C. Liu, Z.-X. Huang, C.-C. Liao, C.-H. Chu, C.-H. Wang, H.-W. Tseng, W.-Y. Hung, P.-T. Chou, *Commun. Mater.* **2021**, *2*, 96.

[162] J. H. Heo, J. K. Park, S. H. Im, *Cell Reports Phys. Sci.* **2020**, *1*, 100177.

[163] Y. Lin, X. Zheng, Z. Shangguan, G. Chen, W. Huang, W. Guo, X. Fan, X. Yang, Z. Zhao, T. Wu, Z. Chen, *J. Mater. Chem. C* **2021**, *9*, 12303–12313.

[164] Q. Zhang, B. Wang, W. Zheng, L. Kong, Q. Wan, C. Zhang, Z. Li, X. Cao, M. Liu, L. Li, *Nat. Commun.* **2020**, *11*, 31.

[165] L. E. Brus, *J. Chem. Phys.* **1984**, *80*, 4403–4409.

[166] D. N. Dirin, L. Protesescu, D. Trummer, I. V. Kochetygov, S. Yakunin, F. Krumeich, N. P. Stadie, M. V. Kovalenko, *Nano Lett.* **2016**, *16*, 5866–5874.

[167] V. Malgras, J. Henzie, T. Takei, Y. Yamauchi, *Angew. Chemie Int. Ed.* **2018**, *57*, 8881–8885.

9 Appendix

Publications

- P. C. Ricci, J. Satta, D. Chiriu, R. Corpino, C. M. Carbonaro, M. Salis, C. Melis, P. S. Normile, J. A. De Toro, **Optical and vibrational properties of CaZnOS: The role of intrinsic defects**, *J. Alloys Compd.* 2019, *777*, 225-233, DOI: 10.1016/j.jallcom.2018.10.311
- J. Satta, C. Melis, C. M. Carbonaro, A. Pinna, M. Salado, D. Salazar, P. C. Ricci, **Raman spectra and vibrational analysis of $CsPbI_3$: A fast and reliable technique to identify lead halide perovskite polymorphs**, *J. Mater.* **2021**, *7*, 127–135, DOI: 10.1016/j.jmat.2020.08.004
- R. Corpino, D. Angioni, J. Satta, F. C. Ugbo, D. Chiriu, C. M. Carbonaro, C. Melis, L. Stagi, P. C. Ricci, **Emission mechanism in single and co-doped Tb:Eu:CaZnOS**, *J. Alloys Compd.* **2021**, *868*, 159007, DOI: 10.1016/j.jallcom.2021.159007
- J. Satta, A. Casu, D. Chiriu, C. M. Carbonaro, L. Stagi, P. C. Ricci, **Formation Mechanisms and Phase Stability of Solid-State Grown $CsPbI_3$ Perovskites**, *Nanomaterials* **2021**, *11*, 1823, DOI: 10.3390/nano11071823
- J Satta, A. Pinna, G. Pia, L. Pilia, C. M. Carbonaro, D. Chiriu, L. Stagi, P. C. Ricci, **Energy Transfer Mechanism in $CsPbBr_3$ – Au Nanostructure,** submitted to Physica Status Solidi (a) – Special issue E-MRS Spring Meeting symposium S

International experiences

8 months stay at BCMaterials, Bilbao (Basque Country, Spain) under the supervision of the senior researcher Daniel Salazar Jaramillo

Thesis co-supervisor

- Stefania Sanna: Bachelor degree in physics. Thesis: Optical and structural characterization of CsZnOS and CaZnOS:Mn.
- Antonella Tessoni, Bachelor degree in physics. Thesis: Phase stability of inorganic perovskites: $CsPbI_3$.
- Alin Grigoras: Bachelor degree in chemistry. Thesis: The use of Raman Spectroscopy for a rapid virus identification.
- Antonio Corona: Bachelor degree in physics. Thesis: Inorganic lead halide perovskites in silica matrices.

Conferences and symposia

- Sardinia goes nano, Sassari 2019, poster contribution: **Vibrational properties of all-inorganic caesium lead iodide perovskite nanocrystals**
- E-MRS Spring Meeting, Strasburg 2021, Talk contribution: **The role of Cs_4PbI_6 in stabilizing caesium lead iodide perovskite**

Certificates

- Single crystal diffractometer training
- Radioprotection formation course
- FullProf Training

Prizes

- Gianni Licheri award
- E-MRS Spring Meeting student award